Reaction-diffusion modelling of hydrogen retention and release mechanisms in beryllium

Mirko Wensing

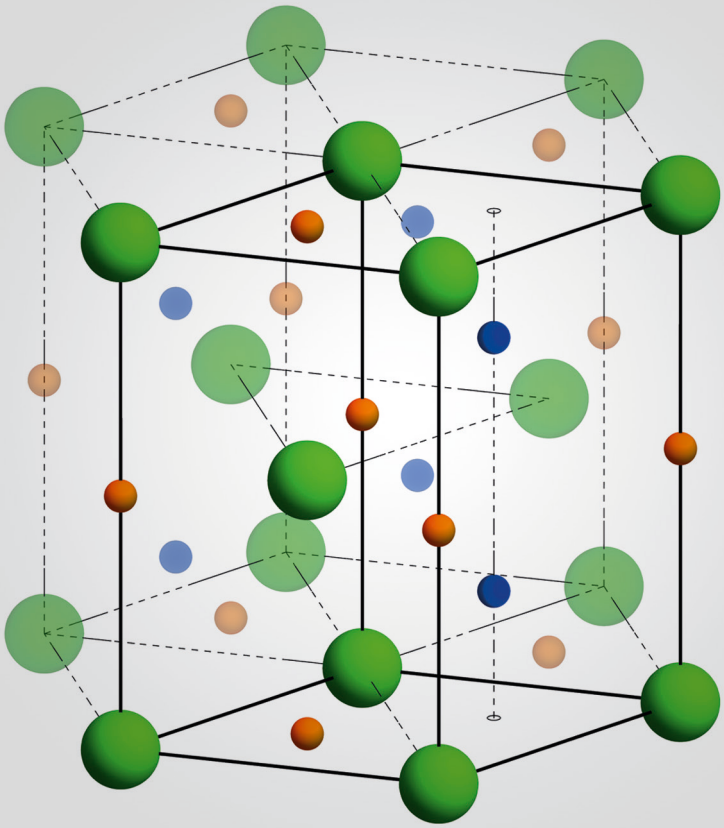

Energie & Umwelt / Energy & Environment
Band / Volume 344
ISBN 978-3-95806-184-2

JÜLICH
FORSCHUNGSZENTRUM

Schriften des Forschungszentrums Jülich
Reihe Energie & Umwelt / Energy & Environment Band / Volume 344

Forschungszentrum Jülich GmbH
Institute of Energy and Climate Research
Plasma Physics IEK-4

Reaction-diffusion modelling of hydrogen retention and release mechanisms in beryllium

Mirko Wensing

Schriften des Forschungszentrums Jülich
Reihe Energie & Umwelt / Energy & Environment Band / Volume 344

ISSN 1866-1793 ISBN 978-3-95806-184-2

Bibliographic information published by the Deutsche Nationalbibliothek.
The Deutsche Nationalbibliothek lists this publication in the Deutsche
Nationalbibliografie; detailed bibliographic data are available in the
Internet at http://dnb.d-nb.de.

Publisher and Distributor:	Forschungszentrum Jülich GmbH Zentralbibliothek 52425 Jülich Tel: +49 2461 61-5368 Fax: +49 2461 61-6103 Email: zb-publikation@fz-juelich.de www.fz-juelich.de/zb
Cover Design:	Grafische Medien, Forschungszentrum Jülich GmbH
Printer:	Grafische Medien, Forschungszentrum Jülich GmbH
Copyright:	Forschungszentrum Jülich 2016

Schriften des Forschungszentrums Jülich
Reihe Energie & Umwelt / Energy & Environment, Band / Volume 344

82 (Master, RWTH Aachen University, 2016)

ISSN 1866-1793
ISBN 978-3-95806-184-2

The complete volume is freely available on the Internet on the Jülicher Open Access Server (JuSER)
at www.fz-juelich.de/zb/openaccess.

Abstract

Beryllium will be the first wall material for the international fusion reactor ITER. Due to the heavy irradiation of the first wall by impinging hydrogen isotopes a detailed understanding of hydrogen retention mechanisms within Be is of technical importance. Especially, the retention of the radioactive isotope tritium needs to be investigated for safety reasons.

This master thesis presents a model based on a reaction-diffusion approach to simulate thermal desorption experiments in order to relate microscopic material properties of beryllium to spectra observed in experiments. After motivation and introduction of experimental observations, hydrogen diffusivity in Be is examined from the theoretical point of view, yielding faster diffusion as indicated experimentally. Mechanisms of hydrogen trapping in vacancies are considered which give rise to a high-temperature peak in thermal desorption spectra. Finally, with the consideration of surface desorption also a fluence-dependent low temperature release stage can be treated in simulations. The model is able to explain the majority of properties that are also visible in experiments and gives good qualitative agreement with experimental observations. An analysis of available experimental data and physical effects is presented.

Zusammenfassung

Beryllium wird als Material für die erste Wand im internationalen Fusionsreaktor ITER benutzt werden. Aufgrund der intensiven Bestrahlung durch auftreffende Wasserstoffisotope ist ein detailliertes Verständnis von Wasserstoffrückhaltungsmechanismen in Be unerlässlich. Besonders die Rückhaltung vom radioaktiven Isotop Tritium stellt ein Sicherheitsproblem dar.

Die vorliegende Masterarbeit präsentiert ein auf Reaktionsdiffusionsansatz basierendes Modell zur Simulation von thermischen Desorptionsspektroskopie-Experimenten um mikroskopische Materialeigenschaften von Beryllium mit experimentell beobachtbaren Spektren in Verbindung zu setzen. Anschließend an Motivation und der Einführung von experimentellen Befunden, wird die Wasserstoffdiffusion von einem theoretischen Standpunkt aus untersucht, die auf eine schnellere Diffusion hindeutet als experimentell beobachtet. Bindungsmechanismen von Wasserstoff in Gitterleerstellen werden untersucht, die zu einem Hoch-Temperatur Peak in thermischen Desorptionsspektren führen. Schließlich wird gezeigt, dass Desorption von der Materialoberfläche in das Modell eingebunden werden kann und zu einem Fluenz-abhängigem Niedrig-Temperatur Peak führt. Das Modell ist in der Lage eine Vielzahl von experimentellen Befunden zu reproduzieren und zeigt qualitative Übereinstimmung. Eine Analyse vorhandener experimenteller Daten und möglicher physikalischer Effekte ist präsentiert.

Contents

1. Introduction

1.1. Thermonuclear fusion

Thermonuclear fusion of light particles to a combined heavier nucleus is the energy source of stars. The first terrestrial realisation of fusion was achieved in 1952 by detonation of a hydrogen bomb [7, p. 285ff]. Since then, significant progress could be achieved in the civil usage of thermonuclear fusion.

To enable the fusion between two atomic cores, the distance between those must not be larger than the attraction region of the strong interaction which binds them to a single heavier nucleus. Therefore, the repelling Coulomb interaction has to be overcome, which is possible in stars under very high pressure and temperature.

Among all possible reactions, the fusion of the hydrogen isotopes deuterium (D=$^2_1$H) and tritium (T=$^3_1$H) has the highest cross section [32, p. 255]. The quantum mechanical tunnelling effect enables the reaction at technically feasible temperatures of roughly 10^8 K

$$\mathrm{D} + \mathrm{T} \rightarrow {}^4\mathrm{He} + \mathrm{n} + 17.6\ \mathrm{MeV}. \tag{1.1}$$

The fuel for the reaction, deuterium and tritium, is obtainable everywhere on earth. Deuterium is naturally available in water with a ratio of 1:6700. Tritium however does only occur in traces in nature due to its relatively short half-life of roughly 12 years. Therefore, naturally occurring tritium is very rare, hence, it is breeded artifically from lithium, which is naturally available in stone and ocean water, according to the reactions

$$^7\mathrm{Li} + \mathrm{n} \rightarrow {}^4\mathrm{He} + {}^3\mathrm{T} + \mathrm{n} - 2.47\ \mathrm{MeV}, \tag{1.2}$$
$$^6\mathrm{Li} + \mathrm{n} \rightarrow {}^4\mathrm{He} + {}^3\mathrm{T} + 4.78\ \mathrm{MeV}. \tag{1.3}$$

The needed neutron is emerging from the fusion reaction itself. Nevertheless, without a method to increase the number of neutrons every single neutron would have to react with a lithium atom to produce as much tritium as what is used in the fusion reaction. For this purpose beryllium can be used as a neutron multiplier to close the fuel cycle

$$^9\mathrm{Be} + \mathrm{n} \rightarrow 2\,{}^4\mathrm{He} + 2\mathrm{n}. \tag{1.4}$$

The resulting energy difference of the D-T reaction of 17.6 MeV is distributed onto the products inversely to their masses (^4He : 3.5 MeV, n : 14.1 MeV). In a magnetically confined plasma, the twofold charged He ion cannot leave the plasma, so its kinetic energy is used to heat the plasma by collisions until the He-core is in thermal equilibrium with its environment. The electrically neutral neutron can leave the plasma and its energy is deposited in the walls of the reactor. Heat exchangers transport the thermal energy to generators to produce electrically usable power.

The fusion reaction is very energy-efficient. The released amount of energy of fusion of 1 g of deuterium-tritium mixture equals the amount of energy from combustion of 12 t of coal [7].

The presence of neutrons in a reactor inevitably incorporates activation processes in the surrounding material. Nevertheless, by choice of suitable structural materials which show reduced activation and which lead to short life-time isotopes, a surveillance time of roughly 100 a [39] is enough until the materials are harmless for the environment and can possibly be used again in the reactor. The need of finding a radioactive waste repository for long-life-time materials, like for conventional nuclear power plants, does not arise.

The most advanced concept to enable the fusion reaction under controlled conditions is the reactor type 'Tokamak'. The magnetical confinement of the plasma within a torioidal vessel is achieved by a combination of external magnetic fields and induced current in the plasma itself.

The tokamak experiment JET (Joint European Torus) has already shown that the fusion of a D-T plasma is feasible. It reached 16 MW power by fusion which equals 62% of the power that was needed for heating the plasma [28].

The next-generation fusion reactor experiment ITER (International Thermonuclear Experimental Reactor), that is currently under construction in Cadarache, will demonstrate that net power gain from fusion, which exceeds the used heating power by a factor of 10, is possible under controlled conditions. It will clarify important technical and physical questions to pass the way for a commercial power plant.

The plasma-facing wall materials in ITER have to withstand extreme conditions. High ion fluxes of $10^{19} - 10^{21}\ m^{-2}s^{-1}$ in the main chamber and $10^{24}\ m^{-2}s^{-1}$ in the divertor region are expected [10]. The energy of particles in the main chamber ranges from thermal energies to some keV with peak energy near some 100 eV.

For ITER beryllium is chosen for the main chamber and tungsten for the divertor region [26]. Beryllium has some beneficial properties that suggest its use as first wall material. The plasma is very sensitive to impurities, especially impurities of high atomic numbers due to radiative cooling. Be has a high tendency of binding oxygen, thus a significant reduction of the oxygen contamination can be achieved. Experiments with the ITER-like-wall in JET have shown that the oxygen contamination within the plasma is significantly reduced by using Be [29]. Unfortunately, Beryllium shows relatively high physical sputtering, the release of wall material due to ion impact. Nevertheless, due to the low atomic number the threshold of acceptable Be contamination in the plasma is rather high ($\approx 5\%$ [13]). For comparison, the tolerable amount of tungsten in the plasma is much lower ($\approx 0.01\%$ [13]). The melting point of 1560 K is rather low compared to other first-

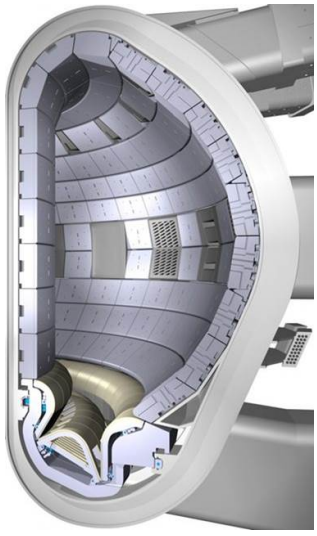

Figure 1: Schematic view of ITER cross-section [27]

wall candidates like tungsten ($T_{melt} = 3695$ K). The strong embrittlement of Be under neutron-irradation is a huge disadvantage. Furthermore, Be must be handled with caution due to the high toxicity of beryllium dust which demands special handling in laboratory experiments [34].

The fact that ions from the plasma steadily bombard the plasma facing components raises the question of retention properties of hydrogen isotopes in beryllium. The process of breeding tritium is very effortful, so wasting fuel in the wall material is undesirable. Furthermore, uncontrolled emission of hydrogen isotopes from the wall could lead to instability of the magnetically confined plasma. Most important, the fact that tritium is radioactive states a safety issue. In a worst-case scenario, where the outer shell is destroyed, potentially gaseous radioactive isotopes state a problem. However, even in a worst-case scenario evacuation of the area around the power-plant is sufficient. A large scale contamination of surrounding areas cannot occur in contrast to conventional nuclear power-plants [26].

Therefore the maximum tolerable amount of tritium that is scheduled for ITER is restricted to 1000 g [26]. The construction for ITER provides the possibility of heating the main chamber to a temperature of 510K in order to release hydrogen from the first-wall [47]. If this is sufficient to remove a majority of retained hydrogen isotopes is still object of discussion.

Therefore, a detailed understanding of the mechanisms that govern the retention and release properties of hydrogen isotopes in beryllium is crucial.

1.2. Thermal desorption spectroscopy

An experimental procedure that is used to investigate the binding states within the material is the thermal desorption spectroscopy (TDS). A material that contains hydrogen isotopes is heated up in a controlled way, usually in a linear manner, while the desorption of particles from the sample is observed, e.g. by mass spectrometers. The thermal desorption spectrum (also commonly abbreviated with TDS) is a curve desorption rate $[\frac{D}{s}]$ (or desorption flux $[\frac{D}{m^2 s}]$) vs. temperature [K] that is a measure for the binding states of hydrogen isotopes within the material.

Originally used to study desorption from material surfaces, by raising the sample temperature linearly and observing the emitted particles, TDS is also used for samples where the desorbant is implanted deeper in the material (e.g. by previous ion implantation). This raises the complexity of the analysis immensely due to the inclusion of bulk processes like diffusion and binding on defects which must be accounted for. Additionally, surface recombination can also state a rate-limiting step in the desorption process. However, predictions may be misleading if the probes are not handled with the adequate caution, e.g. surface contamination might alter the results strongly.

We investigate experiments that were done by M. Reinelt [51][49][50] and M. Oberkofler [45][43] with the ultra-high vacuum experiment ARTOSS [38], that were performed at the Max-Planck institute of plasma physics in Garching. A schematic view of the experimental setup is shown in figure 2.

The experiments are performed under well-defined conditions with base pressure of 10^{-10}–10^{-11} mbar, which is mandatory for maintaining clean sample surfaces. In order to exclude effects from oxygen layers, the composition of atoms on the surface is checked using X-ray photoemission spectroscopy (XPS). Observable surface contamination can then be removed

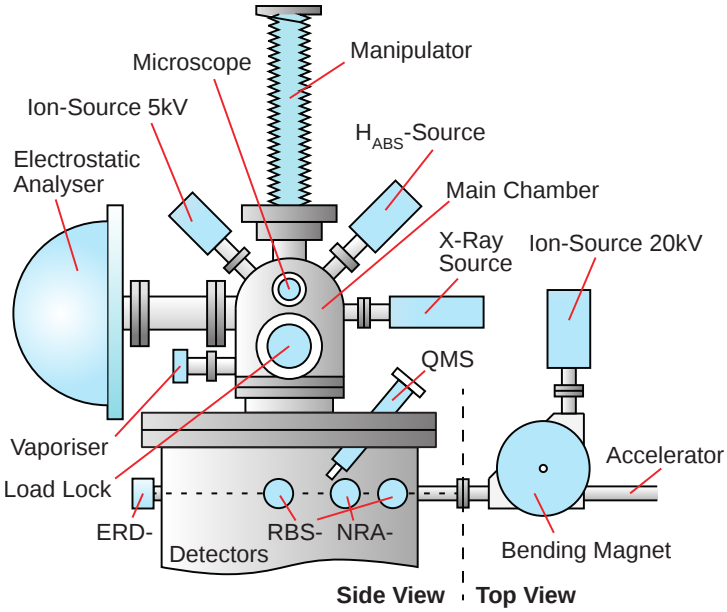

Figure 2: Schematic view of the ARTOSS device. Picture provided with kind permission by Michael Eichler.

by subsequent sputtering with inert ions like argon and annealing cycles. With the relatively good vacuum conditions experiments can be performed within approximately 24 hours until a closed layer of oxygen covers the surface [51].

"Ion source 1" provides a beam of deuterium-ions which is separated according to mass and energy using a magnetic field. Deuterium D_3^+-ions are implanted with defined energies in the keV-regime. At the impact on the material the ions dissociate and the deuterium atoms are implanted. In the following, the primary energy E_{prim} is always given as energy per deuterium atom. Due to the impact of keV-energy ions the primary particle creates collision cascades of atoms in the material. After recombination time on pico-second scale some defects remain in the material. Hydrogen either remains in interstitial position or is bound to defect sites.

After implantation thermal desorption spectroscopy is performed. The sample temperature is raised linearly by electron bombardment of the rear side. The resulting particle desorption rate during the TDS-phase is observed with quadrupole mass spectrometers, that resolve for different particles species according to their mass to charge ratio m/q. The incident gas molecules get simply ionized within the spectrometer, so that the signal for $m/q = 4$ relates to the desorption of D_2 from the sample. Due to the good vacuum conditions the H_2- and HD-molecule signal are orders of magnitude lower. A background correction is not needed.

Depth profiles of the hydrogen distribution can be assessed using nuclear reaction analysis (NRA) via ^{3}He-ion beams with mono-energetic MeV energy. In case a deuterium atom is hit in the bulk material, the nuclear reaction D(^{3}He,p)α with known cross-section can occur, that

yields defined kinetic energy for the proton and the α-particle (2-particle-process). The depth in which the reaction takes place can be estimated from the energy loss of the products due to collisions on its way through the material. These are usually done for calibration of the mass spectrometer. The total amount of hydrogen is estimated from the depth profile and the area of the implantation spot. Comparison to the integrated value of a following TDS yields a calibration factor for the amount of deuterium per second from the mass-4-signal. Which holds under the assumption that all hydrogen is removed from the sample in a single TDS run. Subsequent TDS runs do not show outgassing after the first so this assumption is valid.

The main benefit of doing experiments with ARTOSS is that all these different techniques, implementation, sample cleaning and analysis methods, can be done within the same chamber, without breaking the vacuum in the steps between, which would else immediately result in closed oxide layers on the beryllium surface.

The samples used are single-crystals with surface orientation along the $[11\bar{2}0]$- and [0001]-direction with high-purity. A schematic view of the sample preparation within the experiment is shown in figure 3. An area of roughly 5×5 mm^2 is sputtered by keV-Ar^+-ions which removes surface oxygen. The so created damage is annealed by heating the sample to 1000 K. This procedure is repeated until the surface shows a satisfactory level of oxygen contamination, which can be observed by different methods (XPS, LEIS, NRA, RBS). The implantation of deuterium ions is usually done on an area of roughly 3×3 mm^2 under an incident angle of 90° with D_3^+-ions of fixed energy.

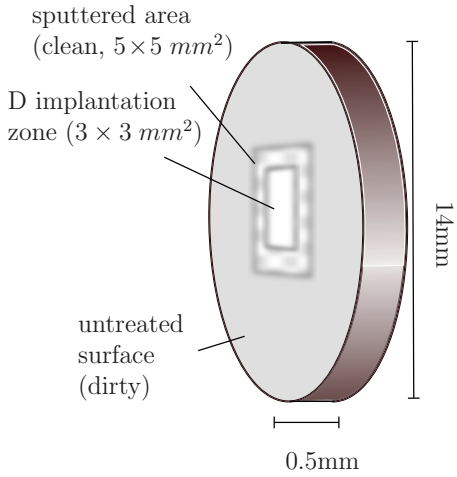

Figure 3: Schematic view of the sample.

One of the main inaccuracies in the experiments provided by Reinelt is the undefined beam profile that was used. It has to be assumed that the beam intensity was neither homogeneous nor in the shape of a square in the implantation zone. The procedure of creating homogeneous implantation profiles was drastically improved by Oberkofler who decided to subsequently expose different regions in the sputtered area to the ion beam [45]. The beam profile was characterized to have a width of approximately 1 mm. The sample is moved during the implantation run to create a sufficiently homogeneous implantation region which consequently yields an edge of ≈ 0.5 mm of reduced fluence around the implantation zone, which however still may influence the outcome of measurements.

Meanwhile the ARTOSS experiment was moved to the Research Center Jülich. The experiment is still under maintenance. Therefore, we investigated measurements previously performed by M. Reinelt [51] and M. Oberkofler [45] in IPP Garching. These will be presented in the next section.

1.3. Experimental observations:

Even though many experiments have been performed, the mechanisms of retention are still subject to discussions. A review of experiments with beryllium is given e.g. by Causey et al. [11] or Anderl et al. [6].

Most experimental results are based on thermal desorption spectroscopy. Here, a summary of most important experimental studies for hydrogen retention in beryllium is given.

Retention in Be changes drastically once a certain fluence Φ_c, that depends on the primary energy of the implanted ions, is overcome. Therefore retention behaviour can roughly be separated into three regions with respect to fluence Φ $[\frac{D}{m^2}]$ (=ion-flux $\times$ exposure time): a) the low fluence regime, b) near-saturation regime and c) way above the critical region. Experiments at the different regions will be discussed in the following.

1.3.1. Low fluence regime

At low exposure fluence $\Phi < \Phi_c$ the release happens in a single desorption peak usually located above 600K. This peak will be referred to as – high temperature peak (HT-peak)– in the following.

The peak maximum depends on the heating rate during the TDS heating ramp and the primary energy of implanted hydrogen ions. The effects of the fluence itself on the HT-peak position is not that clear. In measurements by Oberkofler [45] (see figure 4) the peak maximum shifts towards higher temperature with increasing fluence.

On the contrary, measurements by Reinelt (see figure 5 and also appendix A.1 for more data) do not shift in peak position. The lack of peakshift in data by Reinelt can be attributed to the strongly inhomogeneous implantation profile, where some regions were exposed to higher fluence than others. Due to different local concentration which smears out the peak position of the TDS that is a superposition of desorption fluxes from every region in the implantation zone.

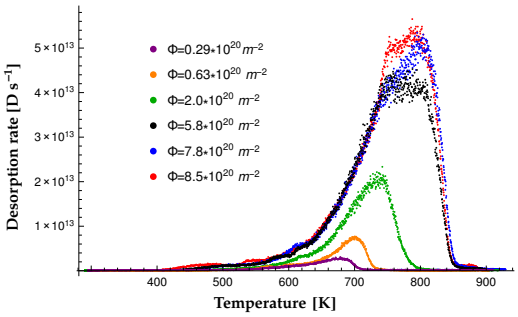

Figure 4: Measurements by M. Oberkofler on single-crystalline Be [45]. Heating rate $\alpha = 0.7$ K/s, primary energy $E_{prim} = 1$ keV/atom.

Markin et. al. [40] observed a non-steadily shift of HT-peak position, which however could be attributed to non-linearity in the used heating ramp.

All the observed HT-peaks have a tendency to a steep decay at the right flank in common.

The total amount of hydrogen that is retained within the sample after implantation increases linearly with fluence. It is commonly agreed about by many authors that the retention of hydrogen at low fluence in Be is close to 100% of the implanted amount [2][44], deviations arising are usually explained by kinetic reflection at the surface of the material which is $\approx 3\%$ for 90° incidence angle[15].

The high-T peak is usually attributed to the trapping of hydrogen in vacancies that were created during ion bombardment after collision cascades [48][43]. Later, it will be shown that vacancies indeed provide very favourable binding states for hydrogen.

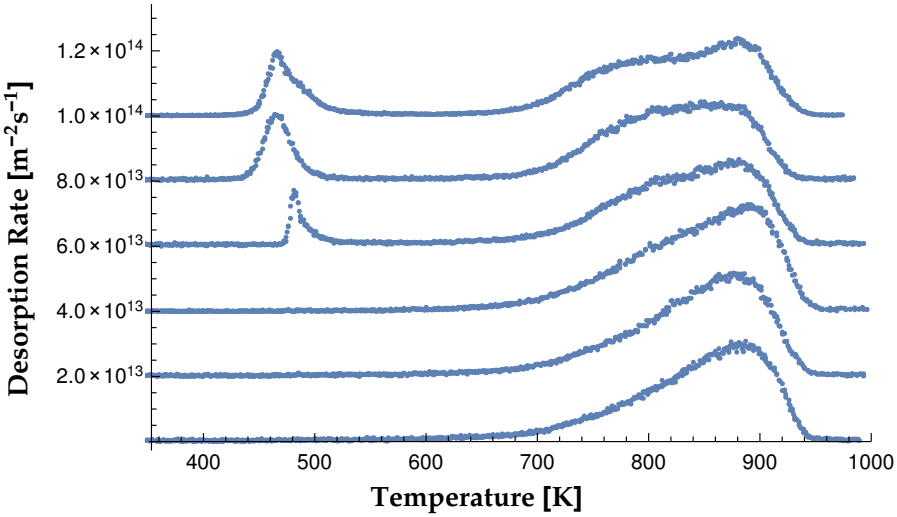

Figure 5: Measurements done by M. Reinelt[50]. Fluence dependence of TDS spectra at constant total amount of hydrogen $1.15 \cdot 10^{15}$ atoms. It shows the emergence of a low-energy binding state at fluence of above $\Phi_c = 10^{21}\ m^{-2}$. Parameters used: $\alpha = 1.45 K/s, E_{prim} = 1$ keV/atom. For the sake of clarity, the zero level of the spectra is shifted at different fluences. Experiments: BeD21,23,24,26,27,28 (for comparison with experiments presented in App. A.1)

1.3.2. Retention near critical fluence

At a certain threshold Φ_c, which depends on the primary energy of the particles, a second peak at lower temperatures emerges, which is clearly separated from the high-temperature stage. Measurements performed by Reinelt are shown in figure 5 for a series of rising fluence. Above $\Phi_c \approx 10^{21}$ m^{-2} the emergence of a – low-temperature peak (LT-peak)– is observed which is also reported consistently by many other authors [43][24][40].

Markin et al. have found a threshold of $\Phi_c = 1.2 \cdot 10^{21}$ D/m^2 by using 5 keV D-ions in poly-crystalline Be. They report a two-peak substructure of the low-temperature peak with maxima at 460 K and 490 K. Transmission electron microscopy (TEM) performed after implantation revealed D_2 bubbles with mean diameter of 1.1 nm and a concentration of $3 \cdot 10^{24}$ m^{-3} which were partly interconnected. They attributed the two-peak structure to the desorption from hydrogen from walls of the channels and opening of gas filled bubbles, respectively [40].

A measurement with $\Phi = 1.89 \cdot 10^{21}$ m^{-2} done by Reinelt [50] is shown in figure 6, which was performed using a snorkel between sample and mass spectrometer, effectively resulting in

an increased signal to noise ratio and more detailed peak structures. A shoulder at the right side of the LT-peak is observed, which however is not observed in all measurements. One has to be careful which kind of properties of the spectra do always occur and which appear just occasionally in the spectra. A visualization of all experimental data provided by M. Reinelt can be found in the appendix (A.1).

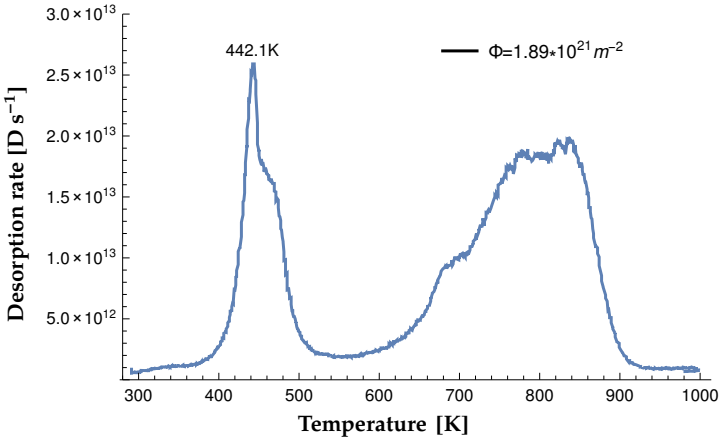

Figure 6: Reinelt, measurement with snorkel [50]: retention of 1 keV/atom deuterium-ions at $\Phi = 1.89 \cdot 10^{21}\mathrm{m}^{-2}$, $\alpha = 1.45K/s$. In this picture the low-T peak seems to consist of two peaks that are very close. The high-T peak has a steep decay at the right side and a shoulder on the left. (BeDS29)

The low temperature states are stable at room-temperature, as indicated by comparison of measurements by Reinelt with immediate post-implantation TDS and a measurement 18 hours after ion implantation (see figure 7). During waiting time the sample was kept at room temperature. In accordance with Reinelt, Markin reported that 20 hours of waiting time did not have influence on spectra [40] indicating the low-energy state is stable at room-temperature and the sample is at (quasi-)thermodynamic equilibrium. Measurements of time evolution of the depth profile were not reported.

Figure 8 shows the retained amount of deuterium in the material as a function of fluence. Above the threshold the retained amount of hydrogen in the sample saturates.

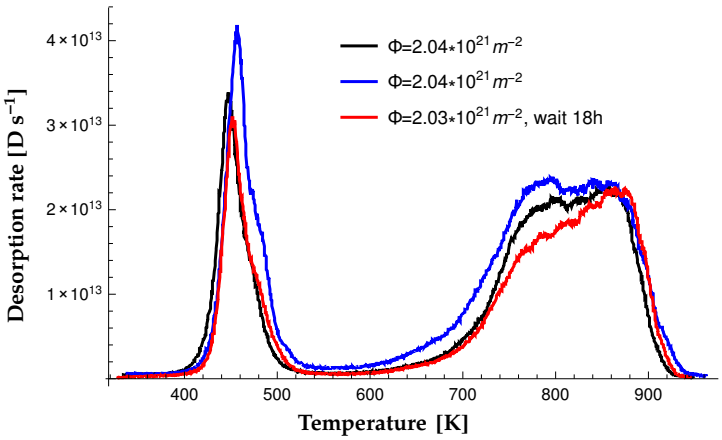

Figure 7: Measurements of comparable fluence [51]: for the blue and black curves TDS was done immediately after implantation, whereas the TDS of the red curve was performed 18 hours after ion implantation. (BeDS31,32,35)

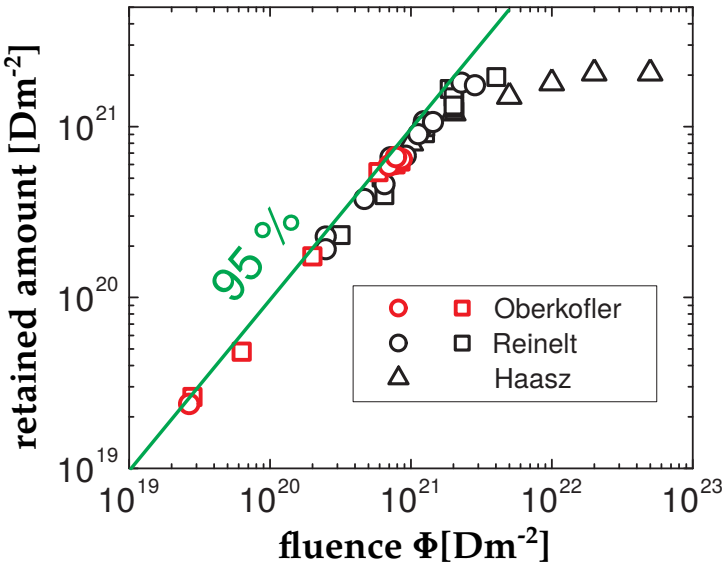

Figure 8: The amount of deuterium that is retained in the sample after irradiation rises linearly approximately up to Φ_c. For higher fluences saturation is observed. The different symbols indicate different samples that were used. Measurements by Reinelt and Oberkofler were done with single crystals with surface orientation $[11\bar{2}0]$, measurements by Haasz were done at polycrystalline Be. Picture adopted from [45]

Figure 9 shows post-implantation depth profiles of atomic D and molecular D_2 in the course of subsequent surface sputtering using 4 keV Ar^+ ions performed by Alimov et al. [2]. The implantation was done at $T_0 = 300$ K with $E_{prim} = 9$ keV/D and fluences ranging in $\Phi = 6 \cdot 10^{19} - 9 \cdot 10^{22} \mathrm{m}^{-2}$. For the highest fluence the ratio of hydrogen stored in atomic form to molecular form equals roughly 1:3. The formation of D_2 molecules is observed at $\Phi \geq 1.5 \cdot 10^{20}$ D/m^2. Retention up to a depth of 700 nm was observed. TDS spectra were not measured. Transmission electron microscopy of the post-implantation samples was performed. These revealed small bubbles of 1 nm radius which increasingly interconnect with rising fluence, which connect to surface areas.

It should be noted that the D^+-signal also may partly have contributions from H_2^+-signal due to equal m/q-ratio.

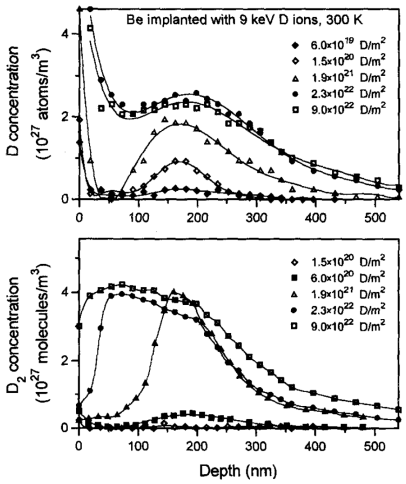

Figure 9: Depth profiles of atomic D and molecular D_2 reported by Alimov et al. Picture taken from [2].

1.3.3. Very high fluence-regime

Experiments performed by Haasz et al. [24] have investigated the retention on polycrystalline beryllium samples at very high fluence $\Phi = 10^{21} - 3 \cdot 10^{24}$ m^{-2}. After ion implantation of 1 keV D at 300 K TDS measurments were performed at 7 K/s heating ramp. Using a flux of 10^{20} Dm^{-2}s^{-1} implantation time varied between $\sim 10s$ for the lowest and up to ~ 20 h for the highest fluences.

Their measurements show that the low-temperature peak increases drastically and contains majority of the hydrogen in the sample. This indicates that the low-temperature states are related to material damaging during implantation. The retention shows saturation for the high fluences. The retained amount of hydrogen is $\sim 2.7 \cdot 10^{21}$ Dm^{-2}, so only about 0.1% of the hydrogen is retained within the sample for the highest fluence studied.

Similar measurements were done by Langley et al. [35] who used a higher primary energy of 25 keV/D. They found retention saturation of $2.8 \cdot 10^{22}$ D/m^{-2}. The increase of a factor 10 is attributed to the higher implantation depth of particles which leads to a lower local volume concentration and therefore need a higher fluence until saturation is reached. In this sense these data do not contradict each other.

Since the fluence of 10^{24} Dm^{-2} is roughly comparable to one pulse of 20 minutes in ITER one can estimate the amount of tritium in the beryllium-cladded main chamber (700 m^2) based on the saturation limit found by Haasz et al. if one assumes that no isotope effect affects the retention and the primary energy of 1 keV is represantative for the wide range of primary energies in a fusion reactor experiment. For one pulse in ITER this leads to a tritium inventory of 9 g. Since measurements by Haasz indicate a saturation behaviour, it can be assumed that this amount does not scale linearly with the number of pulses. The energy distribution of incident hydrogen on the plasma facing components peaks at 100 eV, which

relates to a smaller retention depth and therefore earlier saturation concentration. Still, these estimates are very rough and for more precise values, a deeper understanding of the retention mechanisms is crucial.

In the following, the term – hydrogen (H) – will be used for all isotopes (H,D,T). As soon as dependencies on the specific isotopes arise it will be noted, otherwise hydrogen will be used synonymously for all three of them.

1.4. Rate equation modelling

Results from TDS experiments are usually analysed by comparison with model systems. The simplest approach is to assume that only one of the large variety of mechanisms is rate-limiting, i.e. all other processes happen much faster. The Polanyi-Wigner Method [31] fits this rate limiting step with a single exponential term $R(T) \propto exp(-\frac{E_R}{k_B T})$ with an activation energy E_R. Usually, this method results in much higher activation barriers compared to values calculated by ab initio methods. In fact the possibility that particles are trapped again after their initial release and the diffusive process of interstitial motion of hydrogen atoms can change this picture drastically [23].

A more sophisticated model accounts for multiple mechanisms that influence the release, e.g. diffusion and trapping. One considers the time evolution of volume-averaged concentration fields, for hydrogen but also for different type of lattice defects, according to rate-equations. The volume averaging is done on mesoscopic scale, so that retention profiles can be resolved, whereas atomistic scales are not. The reaction rates $R_i[m^{-3}s^{-1}]$ of the different processes depend on the relative concentration of educts, that can participate in the reaction, an energy barrier that governs the temperature dependence and a frequency prefactor $\nu_{i,j}[s^{-1}m^{3N}]$, where N is the reaction order

$$\mathrm{A}_1 + \mathrm{A}_2 + \mathrm{A}_3 ... + \mathrm{A}_N \rightarrow \mathrm{B}_1 + \mathrm{B}_2 + ... + \mathrm{B}_M \tag{1.5}$$

$$R_{i,j}(\{c\}, T) = \nu_{i,j} exp(-E_{i,j}/k_B T) \prod_{l=1}^{N} c_l. \tag{1.6}$$

Example: Release of hydrogen that is bound to a vacancy (= detrapping)

$$\mathrm{VH} \rightarrow \mathrm{V} + \mathrm{H} \tag{1.7}$$

$$R_{i,j}(c_{VH}, T) = \nu_{dt} exp(-E_{dt}/k_B T) c_{VH}. \tag{1.8}$$

The total change of species i is then given by the sum of all reactions it participates $R_i = \sum_j \pm R_{i,j}$ (sign determined whether reaction $R_{i,j}$ increases or decreases the number of particles of species i). Taking into account the mobility of species the evolution of particle concentrations can be modelled by the following system of (coupled, non-linear) partial differential equations, which is usually referred to as a reaction-diffusion-model. Additionally, a source term $S_i[m^{-3}s^{-1}]$ allows simulation of the implantation process by ion irradiation

$$\partial_t c_i(x,t) = D_i(T(t)) \partial_{xx} c_i(x,t) + R_i(\{c\}, T) + S_i(x,t). \tag{1.9}$$

There exist a couple of codes currently in use that allow for modelling of thermal desorption spectroscopy by means of a reaction-diffusion approach.

The (*Tritium migration analysis* program) *TMAP* [5] allows for up to three immobile defect types within the bulk.

The *CRDS*(*Coupled reaction-diffusion-system*)-code, which was created at IPP Garching [44], allows an arbitrary number of species and reactions among them and also can handle diffusive motion of defects within the material. Piechoczek et al. [48] have shown that this code can be used to (partially quantitatively) reproduce TDS experiments in the low-fluence regime. It accounts for 4 types of species: hydrogen H, empty vacancies V, self-interstitial Be atoms SIA and hydrogen bound inside a vacancy VH. Nevertheless, many of the reaction parameters are subject to discussion and also not all reactions are physically motivated.

At the stage where this master project was started, a proper treatment of hydrogen surface agglomeration and desorption from it was still lacking and the possibility of storing multiple hydrogen atoms in a single vacancy has also not yet been accessed for Be. Until then, no emergence of a fluence-dependent low-temperature desorption stage by means of rate-equation modelling was reported.

1.5. Aim of this thesis

A phenomenological model is developed which is based on physically intuitive arguments, which builds a bridge between macroscopic TDS experiments and microscopic crystal properties which can be predicted by ab initio calculations based on density functional theory.

The aim of this thesis is to elucidate the main mechanisms that govern TDS experiments and (quantitatively) reproduce experiments with a simple model based on a rate equation approach. The CRDS model is re-built from scratch and extended with additional mechanisms.

Special attention is given to the

- extension of the CRDS code by surface effects and the possibility of binding multiple hydrogen atoms in a single vacancy (multiple trapping),
- nature of the emergence of a low-temperature peak at high fluences,
- suggestion of possible experiments to clarify open questions.

The thesis is structured as follows. First, the aspect of hydrogen diffusion in the undisturbed beryllium lattice is investigated and the possibility of explaining TDS experiments without material defects is assessed. In section 3.3.2, the binding of hydrogen within lattice defects is assessed. Ab initio data on vacancy-hydrogen complexes is presented and a minimal reaction-diffusion model is discussed. The model is extended by the possibility of multiple trapping. In section 4, the model is extended by hydrogen agglomeration on sample surfaces. The understanding of processes that lead to experimentally observed spectra is then summarized in section 5 and suggestions for future experiments are provided.

2. Hydrogen diffusion in beryllium

To understand the release of hydrogen that has been implanted into a sample, a good starting point is the discussion of mechanisms of hydrogen transport within the bulk material.

To understand the processes that cause the diffusion and govern its rate crystal properties of Be will be introduced and results from ab initio calculations done by various groups Ganchenkova et. al. [21] [20], Ferry et al. [17] [18] and Zhang et. al. [59][60] will be presented. These will give a theoretical fundament for further discussions.

In order to model the diffusive process by thermally activated jumps and give a theoretical description for diffusion of hydrogen in Be we will make use of the theory of thermally activated processes (see Appendix A.2), which allows to give a first approximation of the diffusivity of hydrogen in beryllium. This picture is refined by usage of a three-dimensional Monte Carlo model, developed in the framework of this thesis, that takes the crystal properties of the real system into account and leads us to a theoretical prediction of the diffusion constant. The prediction is finally compared to values published in literature.

An analytic treatment of the diffusion equation in presence of a linear temperature evolution is given. The possibility of explaining TDS spectra on the basis of only considering diffusive processes is assessed.

2.1. Diffusion in solids

A phenomenological description of particle movement of the macroscopic concentration field $c(\mathbf{x}, t)$ caused due to concentration gradient is given by Fick's law [22]

$$\mathbf{j}(\mathbf{x}, t) = -D(\mathbf{x}, T)\nabla c(\mathbf{x}, t) \tag{2.1}$$

where D is called the diffusion coefficient which in a general material is a 3×3 matrix that has a spatial dependency. For isotropic (nondirectional) materials the diffusion constant is a scalar function. Especially in non-cubic single crystals the possibility of anisotropic diffusion has to be considered. In general, diffusion is strongly temperature dependent.

In combination with the microscopic particle conservation

$$\partial_t c(\mathbf{x}, t) = -\nabla \cdot \mathbf{j}(\mathbf{x}, t) \tag{2.2}$$

we obtain the diffusion equation

$$\partial_t c(\mathbf{x}, t) = \nabla \cdot (D(\mathbf{x}, T)\nabla c(\mathbf{x}, t)). \tag{2.3}$$

In a general hexagonal crystal the diffusion is anisotropic. The diffusion within the basal plane is isotropic, whereas diffusion perpendicular to it exhibits a different diffusivity [22].

$$[D_{ij}] = \begin{pmatrix} D_{11} & 0 & 0 \\ 0 & D_{11} & 0 \\ 0 & 0 & D_{22} \end{pmatrix} \tag{2.4}$$

The purpose of the following sections is to determine the temperature dependent diffusion constant $D(T)$.

2.2. Beryllium: Atomistic properties

Beryllium (**Be**) is the 4$^{\text{th}}$ element of the periodic table. Naturally occurring Be consists almost exclusively of ^{9}Be, all other isotopes are unstable and appear only as traces.

It crystallizes in hexagonal closed-packed (hcp) structure (Figure 10). The i^{th} atom in the unit-cell with indices klm is at location:

$$\mathbf{R}^i_{klm} = k\mathbf{a}_1 + l\mathbf{a}_2 + m\mathbf{a}_3 + \mathbf{b}_i \qquad k,l,m \in \mathbb{Z}, i \in \{1,2\} \tag{2.5}$$

where $\mathbf{a}_i$ and $\mathbf{b}_i$ are the lattice and basis vectors for atoms within the unit cell respectively (Table 1).

Table 1: Summary of crystal parameters

atoms per unit-cell	2
lattice constant a_0	$2.27\mathring{A}$
unit-cell volume V_0	$\frac{\sqrt{3}}{2}a_0^2 c \approx 15.9\mathring{A}^3$
atomic density $\rho_{Be} = 2/V_0$	$\frac{1}{\sqrt{6}a_0^2 c} \approx 0.13\mathring{A}^{-3}$
lattice vectors	
$\mathbf{a}_1$	$(a_0, 0, 0)$
$\mathbf{a}_2$	$\left(\frac{a_0}{2}, \frac{\sqrt{3}a_0}{2}, 0\right)$
$\mathbf{a}_3$	$(0, 0, c)$
basis vectors	
$\mathbf{b}_1$	$(0, 0, 0)$
$\mathbf{b}_2$	$(\frac{a_0}{2}, \frac{a_0}{2\sqrt{3}}, \frac{c}{2})$

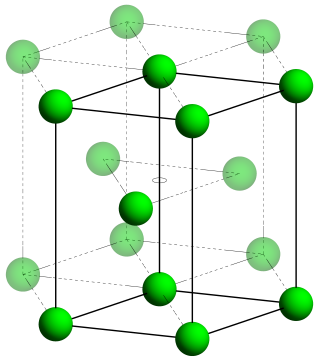

Figure 10: Unit cell and hexagonal supercell of the hcp crystal are shown. Atoms that do not touch the first unit-cell are displayed transparent.

The lattice planes spanned by vectors $\mathbf{a}_1$ and $\mathbf{a}_2$ are called basal planes. The normal to these planes is the [0001]-direction[1]. Another direction that is considered in this work is the $[11\bar{2}0]$-direction that is parallel to basal planes.

Among all elements that crystallize in a hcp-lattice structure Be has the lowest axis ratio

$$\frac{c}{a_0} = 1.57 < \sqrt{8/3}_{\text{ideal hcp}} \approx 1.63 \tag{2.6}$$

due to presence of sp- and sp^2-hybridization with partial filling. The higher populated sp-orbitals are aligned with the c-axis whereas the sp^2-orbitals are located within basal planes. This effectively increases the electron density between adjacent basal planes and leads to a smaller inter-plane distance in c-direction compared to usual hcp-lattices [57].

Certain high-symmetry points are needed for further investigations. A summary of high-symmetry points is given in figure 11.

[1]For trigonal and hexagonal lattice systems four-index notation $[hklm]$ is often used, where the third number is actually redundant and can be obtained from the other indices $l = -(h+k)$. The use of the four-index scheme has the benefit of recognizing permutation symmetries, e.g. the similarity of planes $[110] \equiv [11\bar{2}0]$ and $[1\bar{2}0] \equiv [1\bar{2}10]$ is only evident in four-index notation.

The environment of octahedral (O) and tetrahedral (T) positions is shown in figure 12. Their projections on empty sites in the basal planes are called basal-octahedral (BO) and basal-tetrahedral (BT) positions, respectively. For simplicity, crowdion points (C, BC) are not shown. Transparent atoms in the middle basal plane lie in adjacent unit-cells. For better visibility parts of basal planes that correspond to the octahedron or tetrahedron are colourized.

According to calculations based on density functional theory (DFT) by Ganchenkova et al. [21], Ferry et al. [17] [18] and Zhang et al. [59], the only stable interstitial positions for hydrogen within the Be bulk are the BT and O positions. Therefore, bulk diffusion is a transport through adjacent sites BT and O.

Vector representation for all stable positions in the unit-cell are given in table 2.

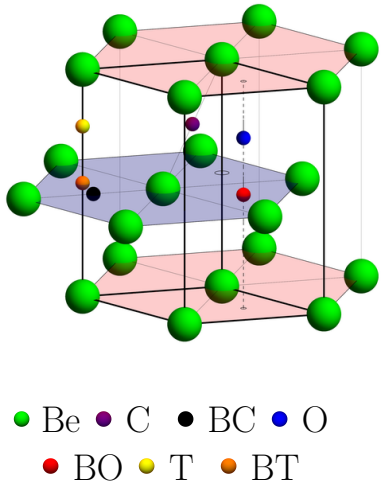

Figure 11: High-symmetry interstitial positions

Table 2: All stable hydrogen interstitial positions in the unit-cell.

BT (basal tetrahedral)	
BT-points per unit-cell	2
BT_1	$\left(\frac{a_0}{2}, \frac{a_0}{2\sqrt{3}}, 0\right)$
BT_2	$\left(0, 0, \frac{c}{2}\right)$
O (octahedral)	
O-points per unit-cell	2
O_1	$\left(a_0, \frac{a_0}{\sqrt{3}}, \frac{c}{4}\right)$
O_2	$\left(a_0, \frac{a_0}{\sqrt{3}}, \frac{3c}{4}\right)$

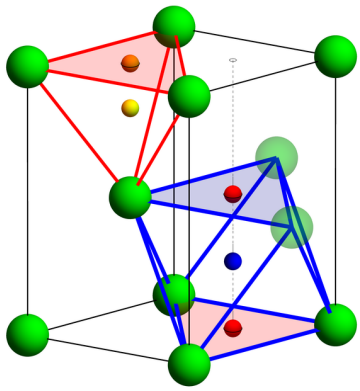

Figure 12: Environment of octahedral and tetrahedral interstitial positions.

All stable interstitial positions in the first unit-cell and in the hexagonal super-cell are shown in figure 13. There are four non-equivalent positions per unit-cell (BT_1,BT_2,O_1,O_2) that can be occupied by hydrogen atoms.

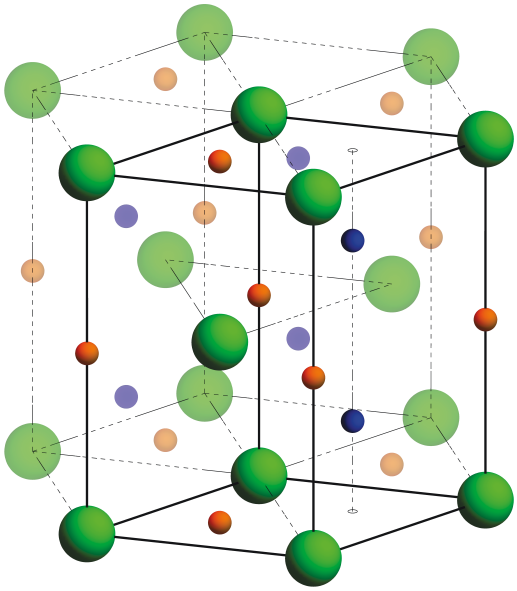

Figure 13: Visualization of the O and BT position within the first unit-cell with opaque spheres. Additional points in the hexagonal cell are shown transparent.

Figure 14 illustrates the positions of stable hydrogen interstitial positions as projection onto the basal plane. The BT positions are located above and below Be atoms, whereas O positions are located between two basal layers. Beryllium atoms are displayed in green or gray for layer A and B, respectively. The stacking sequence is ABAB.

Table 3 shows all vectors that lead from one stable interstitial position to another. These will be needed later for development of a random walk model. Note, that the vectors on the right side of the table are the negative of the left and also the paths involving O_2 can be obtained from O_1-paths mirroring the z-axis (z-parity operator $P_z(a,b,c) = (a,b,-c)$, e.g. $P_z(\overline{O_1BT_x}) = \overline{O_2BT_x}$).

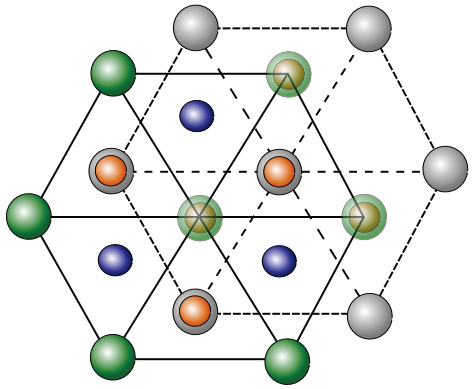

Figure 14: Projection of BT and O positions onto the basal planes.

All migration paths have same length $\lambda = \sqrt{\frac{a_0^2}{3} + \frac{c^2}{16}}$ ($= \frac{a_0}{\sqrt{2}}$ in the case of an ideal hcp crystal with $c = \sqrt{8/3}a_0$).

For estimations of the diffusion constant not only the geometry of the crystal but also

Table 3: All vector representation connections between adjacent O and BT sites.

$O_1 \rightarrow BT_1$	$\left(0, \frac{a_0}{\sqrt{3}}, -\frac{c}{4}\right)$ $\left(\frac{a_0}{2}, -\frac{a_0}{2\sqrt{3}}, -\frac{c}{4}\right)$ $\left(-\frac{a_0}{2}, -\frac{a_0}{2\sqrt{3}}, -\frac{c}{4}\right)$	$BT_1 \rightarrow O_1$	$\left(0, -\frac{a_0}{\sqrt{3}}, \frac{c}{4}\right)$ $\left(-\frac{a_0}{2}, \frac{a_0}{2\sqrt{3}}, \frac{c}{4}\right)$ $\left(\frac{a_0}{2}, \frac{a_0}{2\sqrt{3}}, \frac{c}{4}\right)$
$O_1 \rightarrow BT_2$	$\left(0, -\frac{a_0}{\sqrt{3}}, \frac{c}{4}\right)$ $\left(-\frac{a_0}{2}, \frac{a_0}{2\sqrt{3}}, \frac{c}{4}\right)$ $\left(\frac{a_0}{2}, \frac{a_0}{2\sqrt{3}}, \frac{c}{4}\right)$	$BT_2 \rightarrow O_1$	$\left(0, \frac{a_0}{\sqrt{3}}, -\frac{c}{4}\right)$ $\left(\frac{a_0}{2}, -\frac{a_0}{2\sqrt{3}}, -\frac{c}{4}\right)$ $\left(-\frac{a_0}{2}, -\frac{a_0}{2\sqrt{3}}, -\frac{c}{4}\right)$
$O_2 \rightarrow BT_1$	$\left(-\frac{a_0}{2}, -\frac{a_0}{2\sqrt{3}}, \frac{c}{4}\right)$ $\left(\frac{a_0}{2}, -\frac{a_0}{2\sqrt{3}}, \frac{c}{4}\right)$ $\left(0, \frac{a_0}{\sqrt{3}}, \frac{c}{4}\right)$	$BT_1 \rightarrow O_2$	$\left(\frac{a_0}{2}, \frac{a_0}{2\sqrt{3}}, -\frac{c}{4}\right)$ $\left(-\frac{a_0}{2}, \frac{a_0}{2\sqrt{3}}, -\frac{c}{4}\right)$ $\left(0, -\frac{a_0}{\sqrt{3}}, -\frac{c}{4}\right)$
$O_2 \rightarrow BT_2$	$\left(0, -\frac{a_0}{\sqrt{3}}, -\frac{c}{4}\right)$ $\left(-\frac{a_0}{2}, \frac{a_0}{2\sqrt{3}}, -\frac{c}{4}\right)$ $\left(\frac{a_0}{2}, \frac{a_0}{2\sqrt{3}}, -\frac{c}{4}\right)$	$BT_2 \rightarrow O_2$	$\left(0, \frac{a_0}{\sqrt{3}}, \frac{c}{4}\right)$ $\left(\frac{a_0}{2}, -\frac{a_0}{2\sqrt{3}}, \frac{c}{4}\right)$ $\left(-\frac{a_0}{2}, -\frac{a_0}{2\sqrt{3}}, \frac{c}{4}\right)$

its energetic profile for hydrogen migration has to be known. The *nudged elastic band*(NEB)-method offers access to finding minimum energy-paths and saddle-points, i.e. transition states, for migration paths based on first principles [25].

First, an initial trajectory from one stable side to the other is assumed. Copies of the system with positions along the trajectory are created, all of which are held by artificial spring forces apart in a preferably equidistant way. The trajectory which is built by these nodes is then relaxed influenced by the spring forces and the forces given by the energy hyper surface. This allows for an estimation of the saddle-point and its position.

The mass of the migrating particle is not considered in DFT calculations because the electronic configuration is calculated. Therefore no isotope effect does arise from the energy profile. The energy profile for path BT→O→BT calculated by Ferry et al. [17] is shown in figure 15. Table 4 summarizes all energy barriers that were found by different authors. The path $BT - O - BT$ was found to have the lowest activation barrier. This path therefore dominates the diffusion behaviour of hydrogen within the system. A visualization of the data is shown in figure 16.

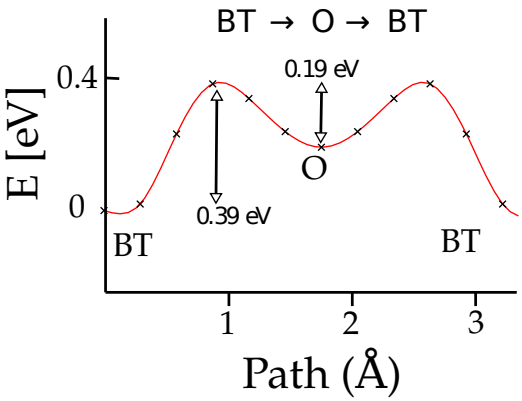

Figure 15: Hydrogen migration energy profile in the perfect crystal. Picture provided with kind permission by Laura Ferry [17].

Table 4: Summary of published diffusion barriers obtained by NEB calculations from various groups. All groups found the BT and O positions to be the only stable interstitial positions. All barriers in eV.

path	Ferry et al. [17]	Ganchenkova et al. [21]	Zhang et al. [59]
BT→O	0.39	0.38	0.4
O→BT	0.19	0.16	0.2
O→ BO → O	-	0.6	0.61
BT→ BO →BT	-	0.8	-
O →C →O	-	-	0.53
BT →C →BT	-	-	0.73

At moderate temperatures only the path with minimal barrier contributes significantly. For beryllium even at $T = T_{melt} \approx 1500$ K the thermal energy $k_B T_{melt} \approx 0.12$ eV is fairly below these barriers, so that the path BT-O-BT is dominating interstitial motion.

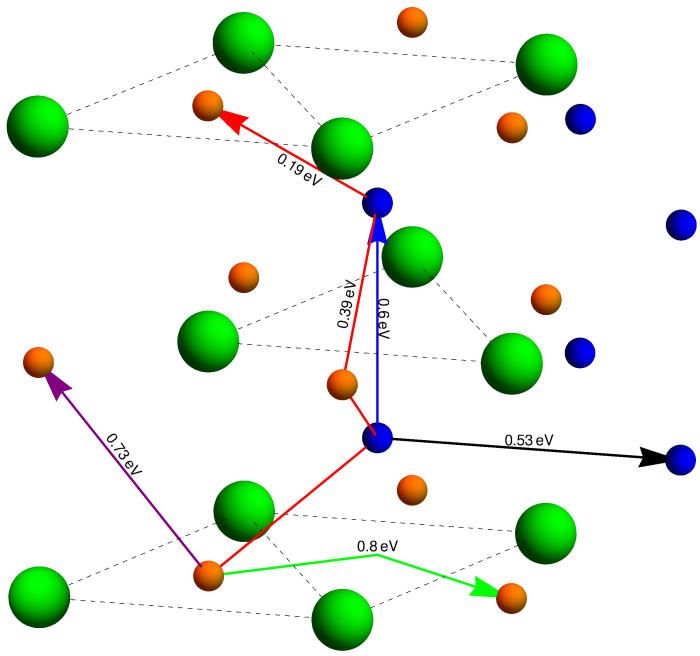

Figure 16: Visualization of distinct diffusion paths. Be-atoms in basal planes are connected with virtual bonds (dashed lines) for eye-guidance.

Ganchenkova et al. [21] give approximate forms of the potential around BT and O positions fitted by quadratic functions where $r = \sqrt{x^2 + y^2}$ denotes the distance from equilibrium position within the basal plane and z the distance along the c-axis

$$E_{\mathrm{BT}}(r,z) = E_{\mathrm{BT}}(0) + (4.7r^2 + 0.57z^2)\frac{\mathrm{eV}}{\mathring{A}^2}, \tag{2.7}$$

$$E_{\mathrm{O}}(r,z) = E_{\mathrm{O}}(0) + (1.4r^2 + 2.0z^2)\frac{\mathrm{eV}}{\mathring{A}^2}. \tag{2.8}$$

The path connecting adjacent BT and O positions (compare Table 3) can always be parametrized by

$$\overline{BT,O}(\tau) = \left(1/\sqrt{3}\cos\phi, 1/\sqrt{3}\sin\phi, \pm c/4\right)\frac{\tau}{\lambda} \text{ with } \tau \in [0,\lambda]. \tag{2.9}$$

Inserting the path $\overline{BT,O}$ into (2.7) and (2.8) we end up with a one-dimensional potential $E = E_0 + \frac{1}{2}kx^2$ which is restricted to the migration path with force constants

$$k_{BT} \approx 6.77 \text{ eV}/\mathring{A} \tag{2.10}$$

$$k_O \approx 3.18 \text{ eV}/\mathring{A} \tag{2.11}$$

From the one-dimensional equation of motion along the trajectory $\mathbf{x}_{\overline{BT,O}}$ we find the vibration frequency along the paths

$$\nu = \frac{1}{2\pi}\sqrt{\frac{k}{m}} \approx \frac{1}{2\pi}\sqrt{\frac{k}{m_p}}\frac{1}{\sqrt{A}} \tag{2.12}$$

$$\nu_{BT} \approx \frac{3.9 \cdot 10^{13} \text{ Hz}}{\sqrt{A}} \tag{2.13}$$

$$\nu_O \approx \frac{2.7 \cdot 10^{13} \text{ Hz}}{\sqrt{A}} \tag{2.14}$$

where we have used that masses of neutrons and protons are nearly identical. The mass number of the involved isotopes is denoted by A ($A = 1$ hydrogen [protium], $A = 2$ deuterium, $A = 3$ tritium). Hence, an isotope effect emerges here.

The transition rate from hydrogen in an interstitial site to an adjacent interstitial site can be computed using Vineyard's theory of thermally activated processes (see App. A.2). The transition rate Γ $[s^{-1}]$ depends on the energy barrier and a prefactor that in principle involves vibrational frequencies ν_i(in equilibrium position) and ν_i'(in transition state) of all atoms within the crystal

$$\Gamma = \nu^* exp\left(-\frac{\Delta E}{k_B T}\right) \tag{2.15}$$

$$\nu^* = \frac{\prod_{i=1}^{N}\nu_i}{\prod_{i=2}^{N}\nu_i'}. \tag{2.16}$$

Unfortunately, the normal frequencies ν_i are not known. This would require computationally expensive phonon calculations on the basis of DFT. However, a crude approximation can be performed if one assumes that the vibrational frequencies of beryllium atoms do not change, depending on the position of the hydrogen atom, i.e. $\nu_i = \nu_i'$. This means (adjacent) beryllium atoms do not "notice" a change in their potential if the hydrogen atom is either in the stable position or in the transition state. This yields for the prefactor $\nu^* = \nu_1$ which is the vibration frequency of the migrating hydrogen atom around its equilibrium site in direction of the transition path given in (2.13) and (2.14).

For this approximation the transition frequency Γ_{BT} from BT to O sites and vice-versa (Γ_O) is

$$\Gamma_{BT} = \nu_{BT} \exp\left(-\frac{\Delta E_{BT}}{k_B T}\right) \tag{2.17}$$

$$\Gamma_O = \nu_O \exp\left(-\frac{\Delta E_O}{k_B T}\right) \tag{2.18}$$

It has to be noted that the transition attempt frequency ν^*, in the limits of this simple approximation, is in the order of the Debey-frequency $\nu_D \approx 10^{13}\ Hz$.

2.3. Atomistic description of diffusion

In a solid, the diffusing particles have to overcome certain energy barriers of height ϵ which are governed by the microscopic structure of the material. According to classical statistical physics particles at thermal equilibrium are distributed according to the Boltzmann distribution $\rho = \rho_0 \exp(-E/k_B T)$, with normalization ρ_0. Therefore, a fraction of $\rho_0 \int_\epsilon^\infty \exp(-E/k_B T) dE = \rho_0 k_B T \exp(-\epsilon/k_B T)$ will be able to surmount adjacent energetic barriers at a given time and contribute to diffusion. Therefore the temperature-dependence of diffusivity is governed by the microscopic energy barriers in the system: $\epsilon = E_D$. Note, that this dependence comes out very naturally in Vineyard's theory. This statement holds in case quantum effects like tunnelling are negligible and the Boltzmann equation is applicable. [19]

Therefore, for a wide range of problems diffusion in solids is usually taken as an Arrhenius law

$$D(T) = D_0 \exp\left(-\frac{E_D}{k_B T}\right). \tag{2.19}$$

Now, we want to relate the prefactor D_0 to microscopic properties. Diffusion takes place as a successive sequence of random jumps. The probability to overcome the energetic barriers for a single atom is small, hence jumps that reach farther than the first neighbour site are even more improbable and can be neglected for a single jump attempt.

For simplicity, we will assume a perfect hcp crystal ($c/a = \sqrt{8/3}$) for the moment. The effect of anisotropy will be taken into account later.

The total displacement after n random steps can be written as:

$$\mathbf{R} = \sum_{i=1}^{n} \mathbf{r}_i \tag{2.20}$$

where $\mathbf{r}_i$ are the vectors between interstitial positions. As we have seen before, these vectors are usually different depending on which interstitial site the considered atom is located before step i. This is related to the low symmetry of the hexagonal crystal lattice (compared with cubic crystal lattices).

The total length of the displacement is

$$\mathbf{R}^2 = \sum_{i=1}^{n} \mathbf{r}_i^2 + 2 \sum_{i=1}^{n-1} \sum_{j=i+1}^{n} \mathbf{r}_i \cdot \mathbf{r}_j \tag{2.21}$$

with equal length of all jumps $\sqrt{\mathbf{r_i}^2} = \sqrt{\mathbf{r_i} \cdot \mathbf{r_i}} = \frac{a_0}{\sqrt{2}}$. Next we average over an ensemble of particles. With the assumption of uncorrelated steps (the probability of any jump does not depend on directions of previous jumps), i.e. $\langle \cos \Theta_{i,j} \rangle = 0$, the double sum vanishes

$$\langle \mathbf{R}^2 \rangle = \langle n \rangle \, a_0^2/2. \tag{2.22}$$

With the average number of jumps in time t given by $\langle n \rangle = tZ\Gamma$, where Γ denotes the transition frequency from one equilibrium location within the crystal to the next one.

The diffusion in three dimensional isotropic media is known to follow the *Einstein-Smoluchowski-Relation*[41, p.58ff]

$$Var(\mathbf{R}) = \langle \mathbf{R}^2 \rangle - \langle \mathbf{R} \rangle^2 = 6Dt, \tag{2.23}$$

i.e. the mean-square displacement of the diffusant is linearly increasing in time with speed determined by the diffusion coefficient. Where we have used that the mean value $\langle \mathbf{R} \rangle$ is zero.

Comparison with (2.22) yields

$$D = \frac{\Gamma Z d^2}{6}, \tag{2.24}$$

$d = a_0/\sqrt{2}$ is the distance between adjacent interstitial BT and O sites. The transition rate is $\Gamma = \nu \exp(-\Delta E/k_B T)$ where ΔE denotes the change in energy between equilibrium and transition state.

The description here used distinct jumps each with the same energy barrier. Nevertheless, it was shown above that for Be the process is a two-step process with energy barrier $E_1 = 0.39$ eV and $E_2 = 0.19$ eV. By means of Monte Carlo simulations in a 1D random walk simulation we will show later that the lower barrier E_2 does not significantly contribute to macroscopic diffusion but instead leads to a correction factor of order unity for the diffusion of a one-step process with the higher barrier E_1.

This leads to a preliminary diffusion constant of hydrogen isotopes in beryllium

$$D(T) = \frac{\nu_{BT} a_0^2}{2\sqrt{A}} \exp\left(-\frac{E_1}{k_B T}\right) \tag{2.25}$$

$$\approx \frac{1.0 \cdot 10^{-6}}{\sqrt{A}} \exp\left(-\frac{0.4 \text{ eV}}{k_B T}\right) \frac{m^2}{s}. \tag{2.26}$$

2.4. Monte Carlo model

In order to take the two-step nature of the diffusion mechanism into account and to study the influence of the distorted lattice structure a three dimensional random-walk model that resembles the full geometry of the problem is built.

The position within the perfect crystal is uniquely defined by specifying the indices i, j, k, l corresponding to

$$\mathbf{R}^{\mathbf{i}}_{\mathbf{jkl}} = j\mathbf{a}_1 + k\mathbf{a}_2 + l\mathbf{a}_3 + \mathbf{b}_i, \tag{2.27}$$

where $\mathbf{b}_i$ indicate the four possible interstitial positions for hydrogen within the unit-cell (BT_1, BT_2, O_1, O_2).

A jump between a lattice site to an adjacent site is uniquely defined by stating the relation between old and new coordinates $i, j, k, l \rightarrow i', j', k', l'$. According to the vector representation paths given above (section 2.2) these are implemented in a C++ code. For each of the four interstitial positions in the unit-cell, there are three paths to one of the two high-symmetry positions of other kind, i.e. 24 distinct paths in total. So the exact crystal structure is represented in the simulation.

The calculation proceeds in 10,000 equidistant time steps, for each the particle "jumps" to an adjacent site with probability $exp(-\Delta E/k_B T)$ where ΔE is assigned to 0.4 eV for BT- and 0.2 eV for O-positions. This process is repeated for $N_{part} = 10^6$ particles at distinct temperatures. The numbers are chosen such that a) convergence of the statistics is observed and b) the random number generator does not get into periodicity issues. Figure 17 shows the trajectory of a single particle.

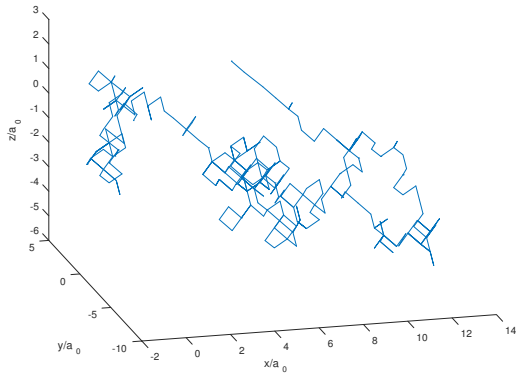

Figure 17: Trajectory of a single particle with 10,000 jump attempts at 1200 K

The time steps are approximately related to the physical time by the inverse frequency factor $\tau = \nu_{BT}^{-1}$ because the jump BT $\rightarrow$ O is the rate-limiting one due to its higher barrier of 0.4 eV. For the given number of steps N_t we simulate the evolution of the system for $t = N_t Z \nu_{BT}^{-1} \approx 2.1 \cdot 10^{-9} s$.

At each time step n the mean and the variance among the ensemble of particles is calculated

$$\langle \mathbf{R}_n \rangle = \frac{1}{N_{part}} \sum_{i=1}^{N_{part}} \mathbf{R}_i, \tag{2.28}$$

$$\langle \mathbf{R}_n^2 \rangle = \frac{1}{N_{part}} \sum_{i=1}^{N_{part}} \mathbf{R}_i^2, \tag{2.29}$$

$$Var(\mathbf{R}_n) = \langle \mathbf{R}_n^2 \rangle - \langle \mathbf{R}_n \rangle^2 . \tag{2.30}$$

Using (2.23) the diffusion constant is obtained at certain temperature T. The linear behaviour of the variance with number of time steps indicates that sufficiently large amount of statistics is included.

Repeating the calculation for different temperatures for 1) all energy barriers $\Delta E = 0.4\ eV$ like in the analytic calculation and 2) $\Delta E = 0.2$ eV in octahedral positions and $\Delta E = 0.4$ eV in basal-tetrahedral positions like in the real system we obtain the plot in figure 18. The anisotropy is studied by considering diffusion parallel to basal planes $\langle X_n^2 + Y_n^2 \rangle$ and perpendicular to them $\langle Z_n^2 \rangle$.

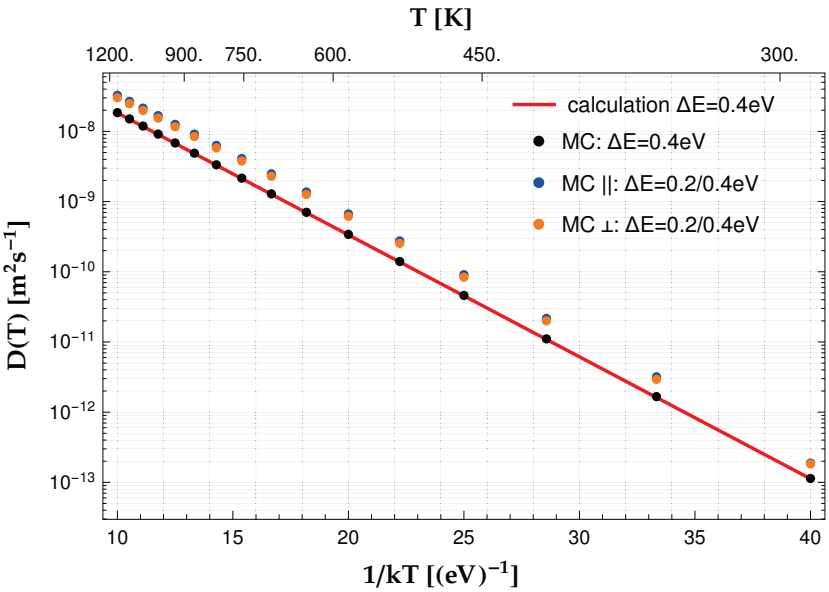

Figure 18: Comparison between previously calculated diffusivity and results of the random-walk model. The black dots were calculated using a perfect hcp crystal lattice, with barriers of 0.4 eV for each jump. The good agreement with the calculation shows that enough statistics is included in the simulation. The blue and the orange dots correspond to calculations in which the lattice distortion $c/a = 1.57$ and the two-step nature of the jump process was used.

The analytic calculation and the random walk model compare very well. Furthermore the two-step nature of the diffusion process speeds up diffusion slightly, compared to the case where each barrier is 0.4 eV. An exponential fit to the two-step data yields

$$D_{||}(T) = \frac{1.89 \cdot 10^{-6}}{\sqrt{A}} e^{-\frac{0.40\ eV}{k_B T}} \frac{m^2}{s}, \tag{2.31}$$

$$D_{\perp}(T) = \frac{1.73 \cdot 10^{-6}}{\sqrt{A}} e^{-\frac{0.40\ eV}{k_B T}} \frac{m^2}{s}. \tag{2.32}$$

As expected the exponential term indicates that the diffusion speed is mainly dominated by the height of the highest barrier, which is $\Delta E = 0.4$ eV for Be.

Figure 19 shows that there is a considerable disagreement between experimental data and our predicted hydrogen diffusivity in beryllium. Many authors consider the diffusivity reported by Abramov et al. $6.7 \cdot 10^{-9} exp(-0.294/k_B T) \frac{m^2}{s}$ [1], which was obtained from gas-driven permeation experiments on high-purity polycrystalline (99.8 wt%-purity) Be-samples, as the most reliable value. They also included the effect of oxide layers in their analysis by multilayer permeation theory. Nevertheless, the actual measurement were performed at only six distinct temperature values, from which two data points were omitted due to bad comparison to the others. Furthermore, it is visible that the literature data themselves have a relatively large scatter over two orders of magnitude. The data indicates a rise in diffusion speed with increasing temperature, which is also expected from the theoretical point of view.

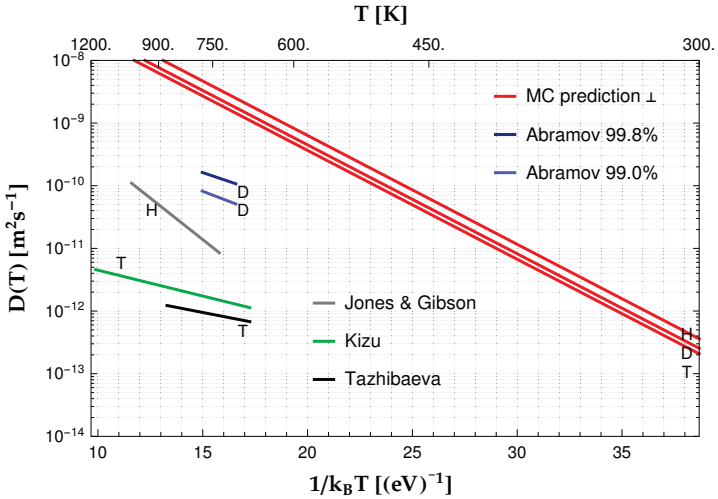

Figure 19: Comparison between our prediction based on theoretical treatment and random walk simulation and experimental data published by Abramov et al.[1] (for 99.0% and 99.8% purity), Jones & Gibson [30], Kizu et al. [33], Tazhibaeva et al. [53]. For comparison BeO diffusivity is $\sim 10^{-16} m^2/s$ for temperature $T = 1200$ K [54].

The discrepancy between theory and experiment could be explained by keeping in mind that beryllium has a high tendency of binding oxygen on the surface and the diffusivity in BeO was reported to be orders of magnitude lower [54], which could yield wrong results in the literature due to surface contamination. Also the presence of impurities within the material can drastically alter the diffusion behaviour. Even for the relatively clean Be sample of Abramov with "only" 0.2% of impurities a significant slowing down of diffusion could occur if the impurities provide trap sites for the deuterium atoms. Another possible explanation is that assumptions in our calculation do not hold, i.e. either 1) classical treatment for H in Be is not applicable or 2) the assumption of equal frequencies of nearest neighbour atoms in the vicinity of the jumping hydrogen particle is not justified. 2) could in principle be resolved by doing computationally expensive phonon calculations on the basis of DFT calculations, which would then provide corrections to the frequency factor.

2.5. Diffusion with temperature ramp

It will be assessed whether it is adequate to model thermal desorption spectroscopy experiments, by an initial configuration, that evolves according to the diffusion equation with a temperature dependant diffusion coefficient. The temperature evolves according to $T(t)$.

$$\begin{cases} \partial_t c(x,t) = D(T(t))\partial^2_{xx} c(x,t) \\ c(0,t) = 0 \\ c(L,t) = 0 \\ c(x,0) = f(x), \quad x \in (0,L) \\ T(t) \text{ given function, } t \in [0,t_e] \end{cases} \tag{2.33}$$

2.5.1. Analytical solution

Equation (2.33) can indeed be solved analytically using a separation ansatz

$$c(x,t) = \tau(t)\chi(x) \tag{2.34}$$

$$\Rightarrow \tau'(t)\chi(x) = D(t)\tau(t)\chi''(x) \tag{2.35}$$

$$\Leftrightarrow \frac{\tau'(t)}{\tau(t)D(t)} = \frac{\chi''(x)}{\chi(x)} \equiv -k^2 = const. \tag{2.36}$$

The fact that the left hand side only depends on time and the right hand side only depends on space states that both sites must be constant to fulfil the equation. We call this constant $-k^2$ for later convenience, we do not make any restrictions on k, in particular we do not claim it to be real.

This yields two ordinary differential equations

$$\tau'(t) = -k^2 D(t)\tau(t) \tag{2.37}$$

$$\chi''(x) = -k^2\chi(x). \tag{2.38}$$

From which the spatial solution is directly obtained

$$\chi(x) = Acos(kx) + Bsin(kx). \tag{2.39}$$

Accounting for boundary conditions yields

$$A = 0 \tag{2.40}$$

$$k = \frac{n\pi}{L}, \qquad n \in \mathbb{N}. \tag{2.41}$$

We restrict n to numbers in $\mathbb{N}$, because negative values for n would yield solutions that are linearly dependent to the ones we already found. $n = 0$ is also taken out because this yields the trivial solution.

Additionally, it is easy to get a solution for (2.37), it is given by:

$$\tau(t) = Cexp\left(-\frac{n^2\pi^2}{L^2}\int_0^t D(t')dt'\right) \tag{2.42}$$

By considering a linear combination for all possible n we get:

$$c(x,t) = \sum_{n=1}^{\infty} B_n \sin\left(\frac{n\pi x}{L}\right) \exp\left(-\frac{n^2\pi^2}{L^2}\int_0^t D(t')dt'\right) \tag{2.43}$$

The constants B_n now have to be determined using the initial configuration $f(x)$.

$$c(x,0) = \sum_{n=1}^{\infty} B_n \sin\frac{n\pi x}{L} = f(x) \tag{2.44}$$

$$\Leftrightarrow \sum_{n=1}^{\infty} B_n \int_0^L \sin\frac{n\pi x}{L}\sin\frac{m\pi x}{L}dx = \int_0^L f(x)\sin\frac{m\pi x}{L}dx \tag{2.45}$$

$$\Leftrightarrow B_n = \frac{2}{L}\int_0^L dx f(x)\sin\frac{n\pi x}{L} \tag{2.46}$$

From a given initial configuration the exact solution can therefore be obtained.

Let us assume, we have determined all the B_n. We are actually interested in the outflux of the sample at either of the sides $x = 0$ or $x = L$.

The particle flux at a given position is given by Fick's first law (in 1D-form).

$$j(x,t) = -D(t)\partial_x c(x,t) \tag{2.47}$$

We end up with:

$$j(0,t) = -D(t)\sum_{n=1}^{\infty} B_n \frac{n\pi}{L} \exp\left(-\frac{n^2\pi^2}{L^2}\int_0^t D(t')dt'\right) \tag{2.48}$$

For a linear heating ramp (which is used in an ideal TDS experiment) and the assumption that the diffusion constant follows an Arrhenius law, we have

$$D(t) = D_0 \exp\left(-\frac{E_D}{k_B(T_0 + \alpha t)}\right). \tag{2.49}$$

Where α denotes the heating rate [Ks^{-1}], E_D the diffusion barrier [eV] and D_0 the diffusion prefactor [$\mathrm{m}^2\mathrm{s}^{-1}$].

Indeed the integral

$$\int_0^t exp\left(-\frac{1}{a+x}\right) dx \tag{2.50}$$

is well known in mathematics. By substitution it can be represented using the generalised incomplete gamma function, which is defined as

$$\Gamma(s, x_0, x_1) = \int_{x_0}^{x_1} t^{s-1} e^{-t} dt. \tag{2.51}$$

Therefore we get

$$\int_0^t exp\left(-\frac{1}{a+x}\right) dt' = \Gamma\left(-1, \frac{1}{a+t}, \frac{1}{a}\right). \tag{2.52}$$

The time integral of the diffusion constant is

$$\int_0^t D(t')dt = \frac{D_0 E_D}{\alpha k_B} \Gamma\left(-1, \frac{E_D}{k_B(T_0 + \alpha t)}, \frac{E_D}{k_B T_0}\right). \tag{2.53}$$

Further analytic evaluation of the lower incomplete gamma function is not possible, nevertheless for given values of T_0, E_D, α and t numerical values are obtainable, e.g. from *Mathematica* [56]. These can be obtained up to arbitrarily high precision. Alternatively, (2.50) can be integrated numerically since the integrand is sufficiently smooth.

Analytic Result

$$j(0,t) = -D(t) \sum_{n=1}^{\infty} B_n \frac{n\pi}{L} \exp\left[-\frac{n^2\pi^2}{L^2} \frac{D_0 E_D}{\alpha k_B} \Gamma\left(-1, \frac{E_D}{k_B(T_0 + \alpha t)}, \frac{E_D}{k_B T_0}\right)\right] \tag{2.54}$$

Remarks:

a) the B_n are the Fourier coefficients of the given initial distribution $f(x)$. E.g. in case we assume a starting configuration $\sin(\frac{\pi x}{L})$, we have $B_n = \delta_{n,1}$ and the sum vanishes.

b) if we do not have a temperature ramp, i.e. $T = const \Rightarrow D(t) = D = const$ we reproduce the result of the time-independent solution $c(x,t) = \sum_{n=1}^{\infty} B_n \sin\left(\frac{n\pi x}{L}\right) \exp\left(-\frac{n^2\pi^2}{L^2} Dt\right)$

Diffusion length $\mathcal{L}$

In order to estimate the length scale on which diffusive processes happen we introduce a new quantity called diffusion length. A measure of the dimensionality length can be found from (2.43)

$$\mathcal{L}(t) = \sqrt{\int_0^t D(t')dt'}. \tag{2.55}$$

It sets the length scale on which diffusion can take place from time 0 to time t. In the case of absent temperature ramp ($\alpha = 0 \Rightarrow \mathcal{L} = \sqrt{D(T_0)t_{wait}}$), i.e. during implantation time or at post-irradiation relaxation time which are on the order of minutes to hours (we will use $t_{wait} = 1000$ s for simplicity), the diffusion length at temperature T_0 is compared for the diffusion constant by Abramov and our predicted value for deuterium migration within the material.

Table 5: Diffusion length at different constant temperatures within 20 minutes. These values exceed the experimentally observed retention depth (for $E_{prim} = 1$ keV) of a few hundred nm. Indicating that mobility of hydrogen must be reduced by other mechanisms.

	Temperature T_0	diffusion length
Abramov:	300K	9 μm
$D = 6.7 \cdot 10^{-9}\ \frac{m^2}{s} exp(-0.294/k_B T)$	600K	150 μm
	900K	390 μm
	1200K	620 μm
our prediction:	300K	124 μm
$D_{\|\|} = 1.89/\sqrt{2} \cdot 10^{-6}\ \frac{m^2}{s} exp(-0.4/k_B T)$	600K	2100 μm
	900K	5500 μm
	1200K	8800 μm

This indicates that hydrogen cannot remain in interstitial positions in the beryllium lattice. Otherwise, hydrogen would either immediately desorb into the vacuum or, in the presence of surface barriers, migrate much deeper into the material as observed experimentally. In order to explain the depth profiles of only a few hundred nanometers either diffusion must be much slower or immobilization of hydrogen by binding in defects occurs. This will be assessed in Section 3.3.2.

2.5.2. Comparison to numerical solutions

If a model is developed it is always useful to test it against analytically solvable problems. The CRDS code introduced in 1.4 is compared here with the previously developed solution (2.54) of an initial profile which evolves according to the diffusion equation in presence of a linear heating ramp (2.33). Due to the high values of $\mathcal{L}$(see above) a simulation on the length scale of the experimentally observed retention depth is not suitable for these tests, because the majority of hydrogen desorbs from the sample after 1 s for profiles of the size of 100 nm. Therefore, the following calculations do not correspond to ion-implantation experiments. However, for experiments in which the profiles are extended through the whole sample, like in gas-loading experiments, these calculations might be applicable.

Three different profiles are investigated: a) a sine profile, b) a Gaussian and c) a step profile.

$$a)\frac{\Phi\pi}{2L}\sin\frac{\pi x}{L} \tag{2.56}$$

$$b)\frac{\Phi}{\sqrt{2\pi}\sigma}exp\left(-\frac{(x-L/2)^2}{2\sigma^2}\right) \tag{2.57}$$

$$c)\frac{4\Phi}{L}\Theta(L/4-x) \tag{2.58}$$

All of which are normalized to the same amount of total hydrogen per area $\int_0^L c(x,0)dx = \Phi = 10^{20}$ m^{-2}. The heating-ramp starts at $t = 0$ with $\alpha = 1$ K/s, the corresponding time-evolution is depicted in figure 20 using our predicted diffusion value $D_{||}$.

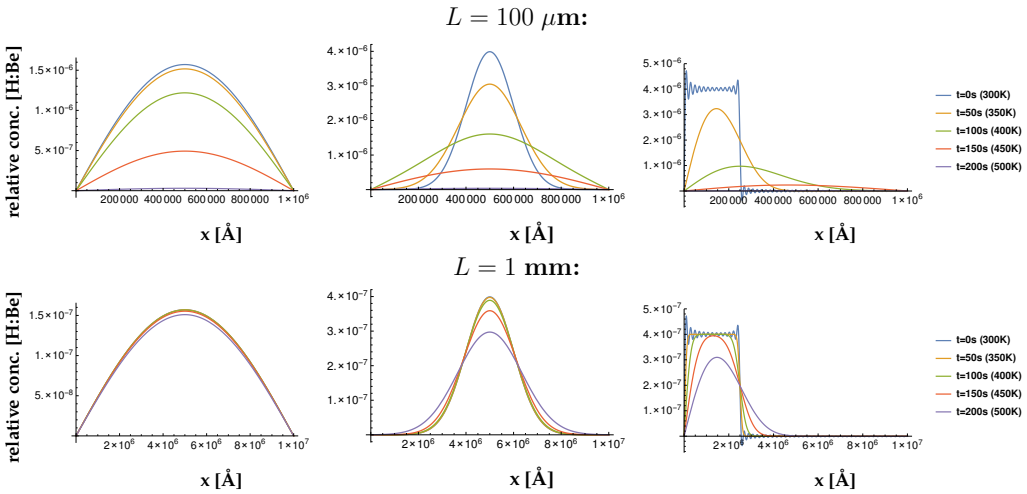

Figure 20: Time evolution of different concentration profiles.

Eq. (2.43) demands for numerical solutions to cut off the series after a finite number of terms. For the simulations these were a) 1, b) 25, c) 100. In the case of the step profile bad

resolution is observed which is however common to Fourier decompositions. As time evolves the solution is smoothed due to decay of fast oscillation terms.

The corresponding thermal desorption spectra are shown in table 6 for Abramov's and our diffusion constant and compare results obtained by the analytic solution with results from the CRDS code.

Table 6: TDS for different retention profiles using only diffusion. Black curves (•) represent the analytic solutions. For comparison we used the CRDS code and disabled all reactions except for diffusion (•). The agreement is very good except for the step profile at $t = 0s(T = 300K)$, where a high flux is observed due to the steep gradient of the step-profile.

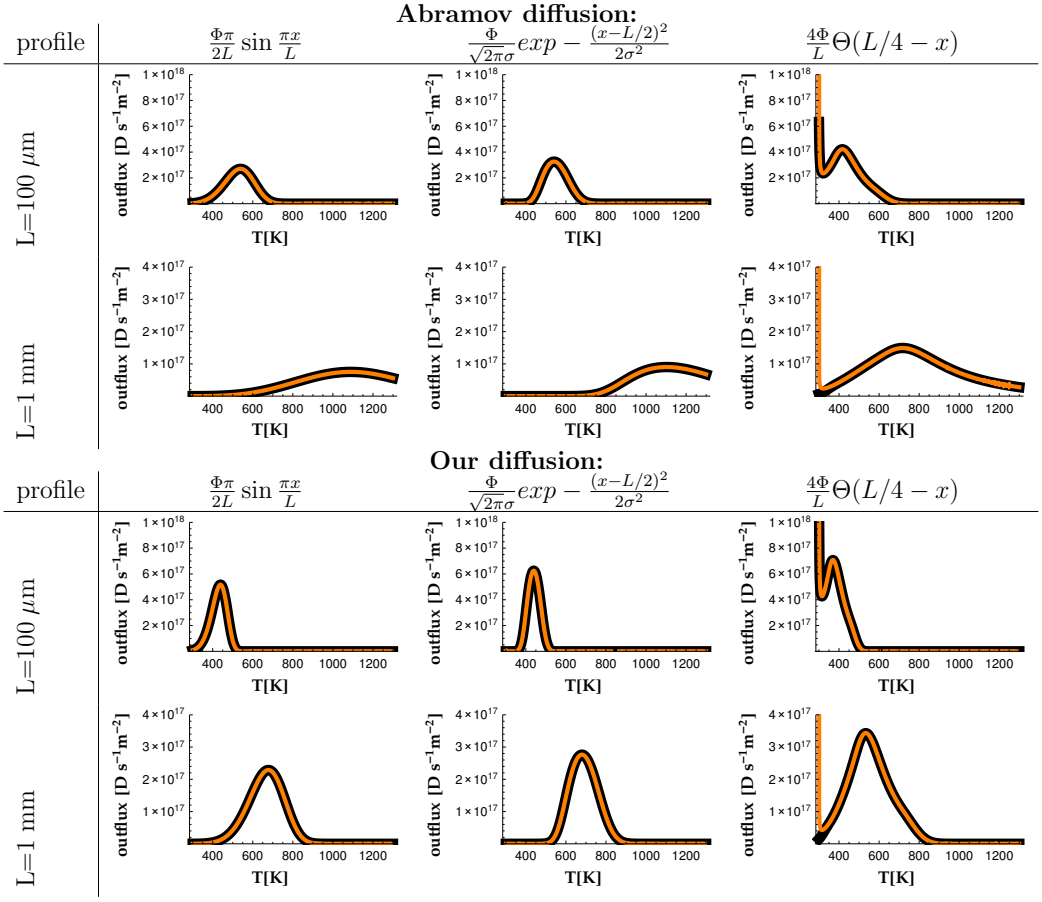

The comparison shows very good agreement between analytical description and CRDS solution. Deviations arise only in the case of the step profile for which the discrepancy at small t is attributed to an insufficient amount of Fourier terms that is used in the analytic model.

2.6. Conclusion

Ab initio data shows that hydrogen remains in interstitial positions of the beryllium lattice. A prediction for hydrogen diffusivity in Be was developed from the microscopic parameters which shows an isotope effect $D \propto m^{-\frac{1}{2}}$ and is two order of magnitude larger compared to experimental values. Contradictions may be explained by surface and/or bulk contaminations on the experimental site or the approximation of formula (2.16) on the theoretical site.

In either description, explanation of TDS spectra based on diffusive processes is not possible.

However, the treatment of diffusive processes in presence of temperature evolution offers possibility for testing the accuracy of the CRDS simulations which shows very good agreement.

3. Binding mechanisms of H in defects

It has been shown that the length scale of diffusion is orders of magnitude beyond the retention depth which is observed experimentally, e.g. by NRA measurements. Obviously diffusion alone cannot explain results from TDS experiments and observed depth profiles. Additional mechanisms need to be considered that immobilize hydrogen in the bulk.

Here we assess if the binding of hydrogen atoms by vacancies can solve this contradiction.

There are studies on the basis of ab initio calculations by several groups, i.e. Ganchenkova et al. [21], Ferry et al. [17] [18] and Zhang et al. [60] who have investigated vacancies in beryllium and their interaction with hydrogen. Results will be reviewed and energetic profiles of the trajectory between interstitial and vacancy sites based on calculations by Ferry et al. [17] will be shown. Based on this data the model is readily refined. The diffusivity of vacancies is examined and ambiguities in earlier CRDS modelling studies by Piechoczek et al. [48] are discussed. Afterwards the model will be extended to account for the possibility to store multiple hydrogen atoms in a single vacancy which leads to good qualitative agreement to experimental TDS spectra at low fluences.

3.1. Environment of vacancies

In the following, the term "vacancy" is used for the environment up to the nearest neighbour atom instead of just the missing atom itself.

A selection of high-symmetry points which is needed in the following is depicted in figure 21. According to the previous case, the same notation as used by Ferry et al. is used [17]. In the vicinity of the empty site new high-symmetry points arise because some positions that were equivalent in the bulk have distinct environments now. The positions within the basal plane near the vacant site are called BT_V and BO_V in accordance with the notation in the undisturbed lattice. The points T_2 and BT_2 are aligned with the c-axis above/below the vacant site. The BT' position is located in the same basal plane as the vacant site which again has basal tetrahedral configuration.

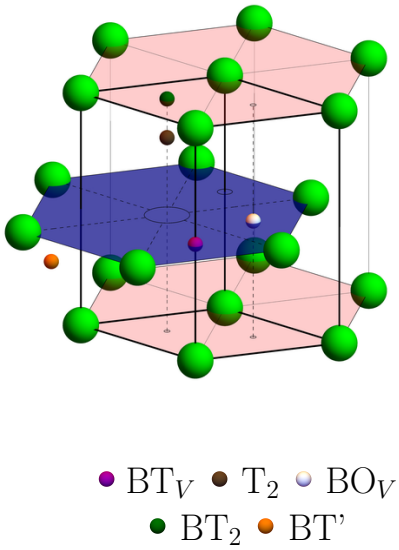

Figure 21: High-symmetry positions around a vacancy.

Many groups investigated the formation energy of vacancies in beryllium Ganchenkova et al. 0.78 eV [21], Ferry et al. 0.87 eV [17] and Middleburgh et al. 1.09 eV [42]. The relative amount of intrinsic (thermally produced) vacancies in the material can be estimated using the formula $C_V = exp(-\frac{\Delta G}{k_B T})$ with Gibbs free energy change $\Delta G = \Delta E + p\Delta V - T\Delta S$, if volume and entropy change are neglected, which is usually ad-

equate for point defects. At room-temperature this leads to $\approx 10^{-13}$ (using the lowest value by Ganchenkova).

For comparison we consider the concentration in the case of a homogenous implantation profile up to depth h, i.e. a step profile, that contains a certain amount of hydrogen. The total amount of hydrogen in the sample is $\int_0^L c(x,t)dx$ (which is approximately equal to fluence Φ for $\Phi < \Phi_c$ and approximately Φ_c for $\Phi > \Phi_c$). The relative concentration of hydrogen in the material retention zone can be estimated from

$$c_{loc} = \frac{\int c(x,t)dx}{h\rho_{Be}}. \tag{3.1}$$

For $E_{prim} = 1$ keV/D the retention profile may be approximated by a step profile that reaches to 50 nm, for higher primary energy the retention depth increases accordingly.

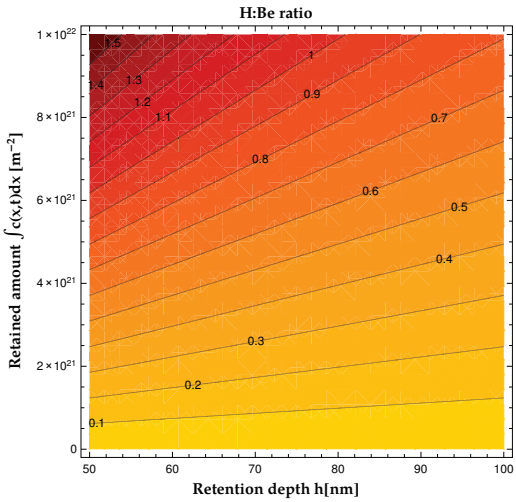

Figure 22: Contour plot of the relative concentration of hydrogen to beryllium atoms if a step-profile of depth h is assumed.

The local concentration of hydrogen in the sample is much higher than the concentration of intrinsic vacancies. Therefore, we conclude if hydrogen release from the high-temperature peak is caused due to binding of vacancies, then these vacancies cannot be thermally produced. These must be created in collision cascades during ion implantation in order to yield concentrations in the percent region.

3.2. Vacancy-hydrogen complex

Indeed vacancy-hydrogen complexes are found to be stable. The authors report consistently that a) up to 5 hydrogen atoms may be stored inside a single vacancy, b) no formation of hydrogen molecules within the vacancy is observed, c) the two-distinct stable high-symmetry positions in the vacancy are T_2-position and BT_V-positions, the latter one being energetically slightly more favourable [21][17][59]. These stable positions are off-center nearly-T_2 and nearly-BT_V-positions which are in the following simply called T_2 and BT_V. Small deviations from the position will let the hydrogen position relax towards T_2 or BT_V. The vacant site (V) itself presents an unstable position for hydrogen with nearly 1.2 eV energy higher than BT_V.

An overview of all stable high-symmetry points in the vacancy and the corresponding binding energies for different filling-levels are depicted in figure 23. Binding energies are calculated as $E_b^{VH_n} = E_c^H + E_c^{VH_{n-1}} - E_c^{VH_n}$, where E_c is the configuration energy in the DFT calculation by Ganchenkova et al. [21]. The data indicates the most favourable filling order as $BT_V \rightarrow 2BT_V \rightarrow 3BT_V \rightarrow 3BT_V{+}T_2 \rightarrow 3BT_V{+}2T_2$. Note, that these are energy differences between

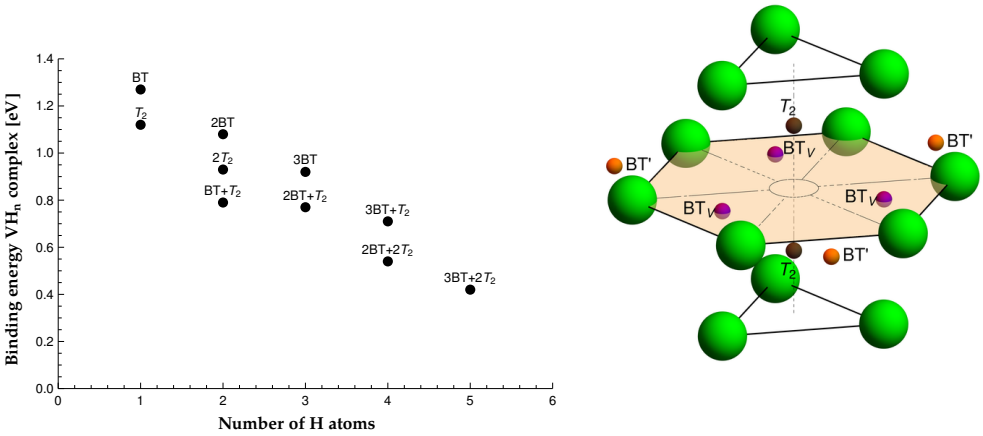

Figure 23: Left: binding energies of Stable hydrogen positions for different number of hydrogen atoms in a vacancy [21]. Right: all stable hydrogen positions in a vacancy.

bulk interstitial and vacancy levels, the plot does not give information about the barrier that is needed for the transition from one state to the other.

Calculations based on the nudged elastic band methods (NEB) were performed for every filling level by Ferry et al. [17]. The energy profiles that were obtained based on this method for a single hydrogen in the vicinity of a vacancy is shown in figure 24 for two distinct paths both involving a BT'-position. It can be seen that the energy level at the BT' position is energetically equivalent to an interstitial BT position in the bulk.

An atom can be considered to have escaped from the basin of attraction of a vacancy, i.e. it is "detrapped", if thermal excitations will not lead to an almost certain retrapping afterwards, i.e. hydrogen atoms that reach O positions can be considered to be detrapped. Atoms in BT' need to overcome a barrier of only 0.2 eV to fall into a vacancy but 0.39 eV to migrate deeper into the bulk. Therefore, the BT' position cannot be considered as a "detrapped" state. The total detrapping barrier – as we will call it in the following – is therefore defined as the energy difference between the most stable vacancy site that can be occupied, i.e. BT_V (for filling up to $n = 3$), and the transition energy level to an interstitial state which has isotropic energy landscape, i.e. an O-position that can be reached from BT'. This definition leads to a detrapping barrier of ~ 1.5 eV for a single hydrogen atom in a vacancy. Fine structures of the energetic profiles are in the following not considered by our model.

The trapping barrier is governed by the diffusion barrier in the crystal, i.e. 0.4 eV according to the data presented in section 2.

Similar investigations can be done for a vacancy that already contains $n - 1$ atoms. The energy profiles for motion of the n^{th} atom along distinct paths are summarized in figure 25. For simplicity, only the minimum barrier paths are shown. The shift of the position of the minima with rising filling level is attributed to the volume increase of the configuration due to hydrogen presence.

a) path 1: BT' - BO_V - BT_V

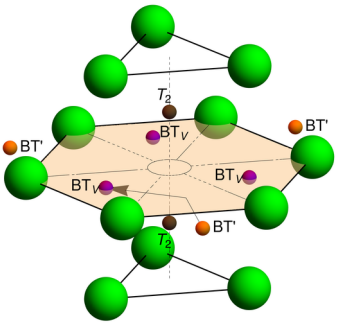

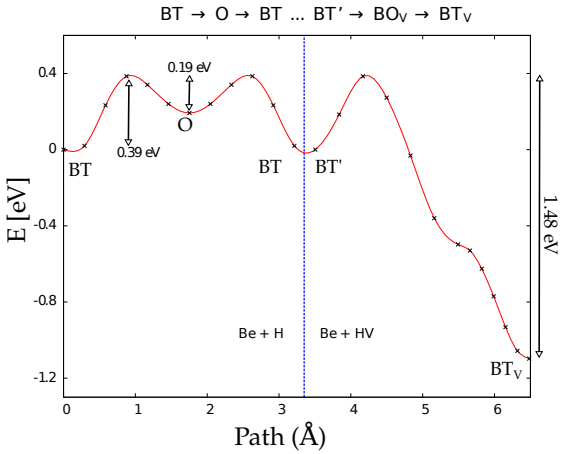

b) path 2: BT' - T_2 - BT_V

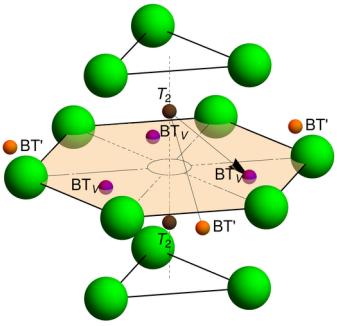

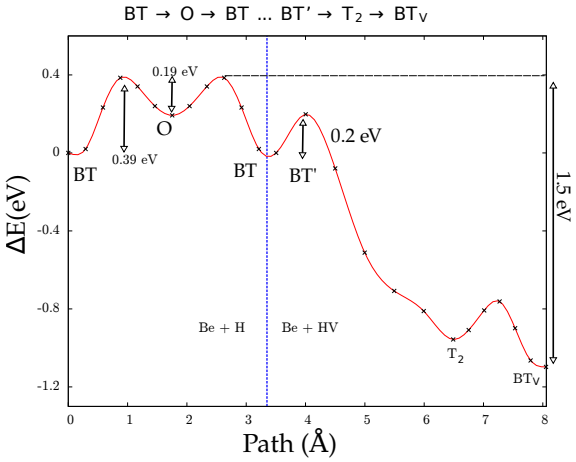

Figure 24: Trapping and detrapping path for a single hydrogen atom in the vicinity of a vacancy. Detrapping barriers are $\sim$ 1.5 eV for both paths. Trapping barriers are governed by the diffusion barriers 0.4 eV. Solid lines for eye-guidance only. Energy profiles provided with kind permission by Laura Ferry [17].

Note, that for the total barrier the energy level to the transition state to O must be taken into account, which is at 0.4 eV in the energy profiles in figure 25. Approximate values for the trapping and detrapping barriers are shown in table 7 to summarize the values that will be used in the following.

a) path 1: BT' - BO_V - BT_V
for the 1^{st}, 2^{nd} and 3^{rd} hydrogen atom

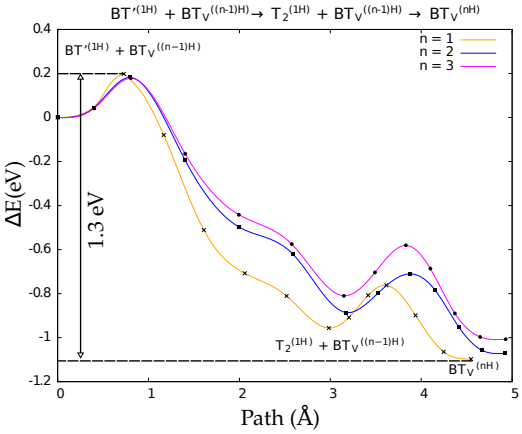

b) path 3: BT' - T_2
for the 4^{th} and 5^{th} hydrogen atom

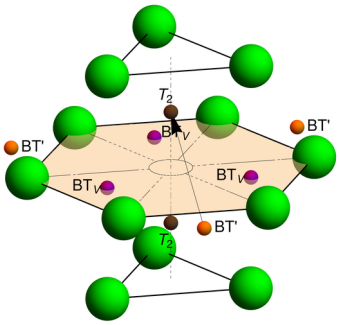

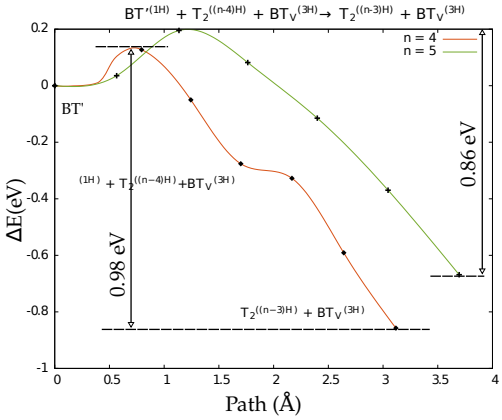

Figure 25: Summary of lowest barrier paths for (de)trapping processes up to the 5^{th} hydrogen atom. Solid lines are for eye-guidance only. Energy profiles provided with kind permission by Laura Ferry [17].

Table 7: Summary of barriers for trapping and detrapping that are used in the following

n hydrogen atoms per vacancy	1	2	3	4	5
detrapping barrier [eV]	1.50	1.45	1.40	1.20	1.05
trapping barrier [eV]	0.40	0.40	0.40	0.40	0.40

3.3. From first-principles to rate-equation modelling

Next, we are going to relate the microscopic parameters, i.e. vibration frequencies and energy barriers with macroscopic parameters that will be captured in the macroscopic rate equations.

3.3.1. Detrapping: VH → H + V

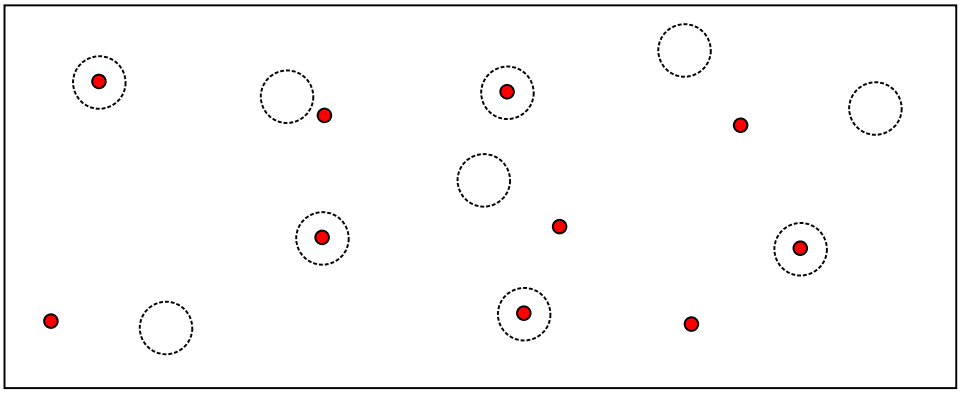

Figure 26: A system of mesoscopic volume V with N_H hydrogen atoms, N_{VH} simply filled vacancies and N_V empty vacancies. Ω_V is set of all points that are located within dashed circles, each of which having volume V_t. Expressions for trapping and detrapping rates are derived below.

Consider a volume V with N_{VH} singly occupied H-filled vacancies as shown in figure 26. The transition probability $p_{dt} = \nu_{dt} \exp\left(-\frac{E_{dt}}{k_B T}\right)$ per unit-time can be calculated by means of thermally activated processes. The total number of hydrogen emitted from trap sites is then $p_{dt} N_{VH}$. Division by the considered volume gives the number of hydrogen atoms that are detrapped per volume per unit-time

$$\Gamma_{dt} = p_{dt} \frac{N_{VH}}{V} = \nu_{dt} \exp\left(-\frac{E_{dt}}{k_B T}\right) c_{VH}. \tag{3.2}$$

3.3.2. Trapping: H + V → VH

The case of trapping is more involved because two species of particles are needed for the reaction. The probability per time p_t that H is being trapped in V is valid for the case of H being in the basin of attraction of a vacancy, i.e. hydrogen is located in a certain volume V_t centred around a vacant lattice site. The set of points in the basin of attraction of vacancies is denoted by $\Omega_V \subset \mathbb{R}^3$. Only hydrogen that has a certain distance not too far away from the vacant lattice site may be captured. Therefore, the trapping probability may be written as

$$p\{trapping\}(\mathbf{x}) = \begin{cases} p_t & \text{if } \mathbf{x} \in \Omega_V \\ 0 & \text{if } \mathbf{x} \notin \Omega_V \end{cases}. \tag{3.3}$$

By averaging over volumes on a mesoscopic length scale, the total amount of hydrogen being trapped per second is accordingly $p\{trapping\} N_H = p_t N_H \frac{N_V V_t}{V}$. Division by the system volume V yields the number of hydrogen atoms that are trapped per volume per second

$$\Gamma_t = p_t c_H c_V V_t. \tag{3.4}$$

For beryllium we have seen that the basin of attraction may be defined as the volume up to BT' positions, from which trapping is more probable than migration to adjacent O sites (see figure 24 b)). Actually the trapping mechanism that we have assessed only accepted trapping from these sites within the basal plane. However, there are more paths with similar barriers which lead to quasi spherical symmetric trapping [17]. Therefore, a reasonable assumption is to take the trapping volume V_t as all sites within a radius smaller than the BT' distance from the vacancy. This definition yields a trapping radius $r_t = \frac{2a_0}{\sqrt{3}}$ which leads to a trapping volume of $V_t = \frac{4}{3}\pi r_t^3 \approx 75.4\mathring{A}^3$. The per-time probability is again related to a frequency factor and an activation barrier $p_t = \nu_t \exp\left(-\frac{E_t}{k_B T}\right)$. The value of V_t is fixed in the following because it is sufficient to vary $\nu_t[\mathrm{s}^{-1}]$ for parameter studies.

Remark: In earlier CRDS calculations e.g. done by Piechoczek et al. [48] $\Gamma_t = p_t \frac{c_H c_V}{\rho_{Be}}$ was used, where ρ_{Be} is the volume density of the undisturbed beryllium crystal to account for the correct dimensionality of the expression, which would correspond to a trap radius of only $1.3\mathring{A}$, which is apparently too small. With our treatment the trapping rate increases by a factor of ~ 9.3 compared to Piechoczek's rate. We will revisit the work by Piechoczek in section 3.6.

3.4. Simple CRDS

In the ARTOSS experiments the implantation region has a lateral area of a few mm^2, whereas the depth to which the hydrogen atoms are trapped is just a few hundred nanometres deep. From a modelling point of view we can therefore treat the system as a one-dimensional system if the implantation profile is sufficiently homogeneous[2] and only consider the in-depth distribution of hydrogen.

To account for the effect of hydrogen immobilization due to trapping in vacancies two 'species' are considered: mobile/solute hydrogen c_H and immobile/trapped hydrogen c_{VH}. In the atomistic picture the mobile particles correspond to hydrogen atoms in interstitial positions and the immobilized ones to hydrogen in vacancy sites. The two species are then coupled by trapping and detrapping terms, which leads to a system of coupled partial differential equations (3.5). The boundary conditions were chosen to be of Dirichlet type, i.e. surface recombination is not rate-limiting in this model.

$$\begin{cases} \partial_t c_H(x,t) = \underbrace{D_H(T(t))\partial^2_{xx} c_H(x,t)}_{diffusion} - \underbrace{\Gamma_t}_{trapping} + \underbrace{\Gamma_{dt}}_{detrapping} \\ \partial_t c_{VH}(x,t) = \quad + \Gamma_t \quad - \quad \Gamma_{dt} \\ c_H(x,t=0) = 0 \\ c_{VH}(x,t=0) = c_V(x) \\ c_i(x=0,t) = c_i(x=L,t) = 0 \qquad \text{for } i \in \{H, VH\} \end{cases} \tag{3.5}$$

[2] In principle, also inhomogeneous profiles with varying local fluences can be treated by this model by performing multiple calculations at according fluences. The desorption fluxes of each simulation are then superposed according to the experimental implantation profiles. Unfortunately, for measurements performed by Reinelt the implantation profiles are unknown.

As shown earlier in figure 7 TDS spectra do not change significantly on the time-scale of hours after ion-implantation if the sample is kept at room temperature. Which indicates the sample is in a (quasi-) thermodynamic equilibrium after ion bombardment. This encourages the idea of starting the simulation with an initial profile of trapped hydrogen instead of using source terms[3]. To see if a given configuration is stable at room-temperature a waiting time of 1000 s is used before the temperature ramp starts. A schematic view of the simulation system is shown in figure 27.

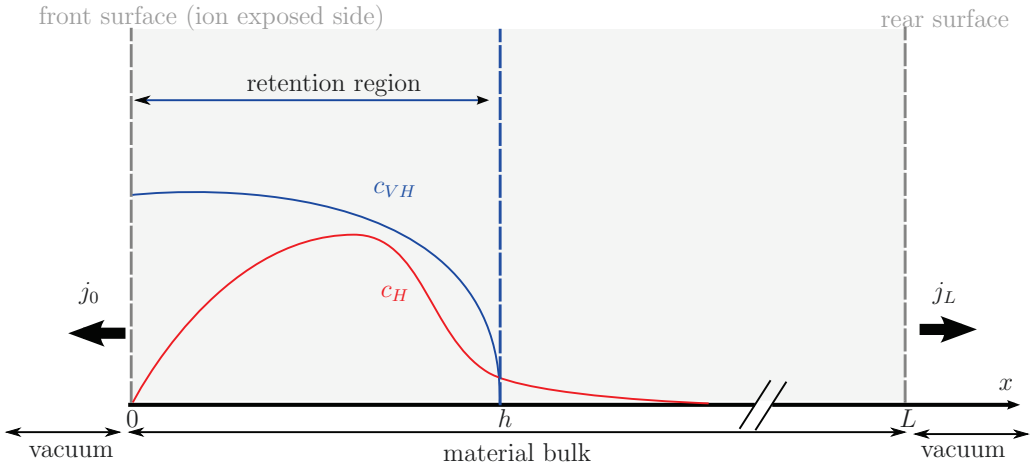

Figure 27: The one-dimensional representation of the sample of thickness L is shown. After volume averaging spatially dependant concentrations c_i [m^{-3}] for every particle/defect-species i are considered.

The PDE system (3.5) is solved numerically using the *Wolfram Mathematica* solver *NDSolve*[56], for computational details see appendix A.4. From the solution, i.e. the functional form of $c_i(x,t)$, the desorption flux at the left/right side of the sample can be calculated using Fick's law

$$j_0(t) = D_H(T(t))\partial_x c_H(x,t)|_{x=0} \tag{3.6}$$
$$j_L(t) = -D_H(T(t))\partial_x c_H(x,t)|_{x=L} \tag{3.7}$$

by numerical differentiation at the boundaries. Note, that the fluxes are chosen positive if hydrogen flows out of the sample. After multiplication with the area of the implantation zone these directly relate to desorption rates that are measured experimentally.

[3] In earlier CRDS studies, a source term $S_i[\mathrm{m}^{-3}\mathrm{s}^{-1}]$ was added that accounts for the implantation of hydrogen ions, the corresponding implantation profiles can be obtained from other codes (e.g. SDTrimSP [16]) that simulate the implantation process based on binary-collision approximation of projectile and bulk particles. However, this raises the complexity of the simulations because it is less clear how the dynamics of defect creation influence the simulation. As will be shown later, the retention profile has small influence on the TDS spectra therefore a better starting point for modelling is at the relaxed system after implantation.

The model (3.5) indeed conserves the total particle number. The change of the total number of hydrogen in the system is given by

$$\frac{d}{dt}N_H = \partial_t \int_0^L (c_H(x,t) + c_{VH}(x,t))dx \tag{3.8}$$

$$\overset{(3.5)}{=} \int_0^L D_H(T(t))\partial_{xx}^2 c_H(x,t)dx \tag{3.9}$$

$$= D_H(T(t))\partial_x c_H(x,t)|_{x=0}^{x=L} \tag{3.10}$$

$$= -j_0(t) - j_L(t). \tag{3.11}$$

So the amount of hydrogen only changes by desorption from the surfaces.

Time-evolution of the profiles obtained by CRDS simulation with the parameters given in table 8 is shown in figure 28. No significant detrapping is observed at temperatures below 500 K. Only the desorption flux on the ion-exposed (left) side of the sample is considered, because the contribution from the right side is four orders of magnitude smaller and can therefore safely be neglected.

The following calculations are done with parameters given in table 8 if not stated otherwise.

Table 8: Overview of parameters used in the following calculations. For the chosen initial profile the H:Be-ratio is $\sim 17\%$ in the retention zone.

Mechanism	prefactor	energy barrier	Exp. parameter	value
H diffusion	$D_0 = 1.89/\sqrt{2} \cdot 10^{-6}$ m^2/s	$E_D = 0.4$ eV	Fluence	$\Phi = 10^{21}$m^{-2}
Detrapping	$\nu_{dt} = 10^{12}$ s^{-1}	$E_{dt} = 1.5$ eV	Sample size	$L = 0.5$ mm
Trapping	$\nu_t = 10^{13}$ s^{-1}	$E_t = 0.4$ eV	heating	$\alpha = 1$ K/s
			retention depth	$h = 50$ nm

The introduction of binding states resolves the contradiction between very small retention depths ($\sim$ couple of 100 nm) and the fast diffusion ($\sim$ 10 μm after 1000 s of diffusion time using the Abramov value). The corresponding TDS spectrum is also shown, which consists of a single peak at 755.2 K.

In the following, some qualitative parameter studies within a reasonable parameter range will be shown to estimate the impact of different parameters on TDS spectra. Only one parameter is varied at a time.

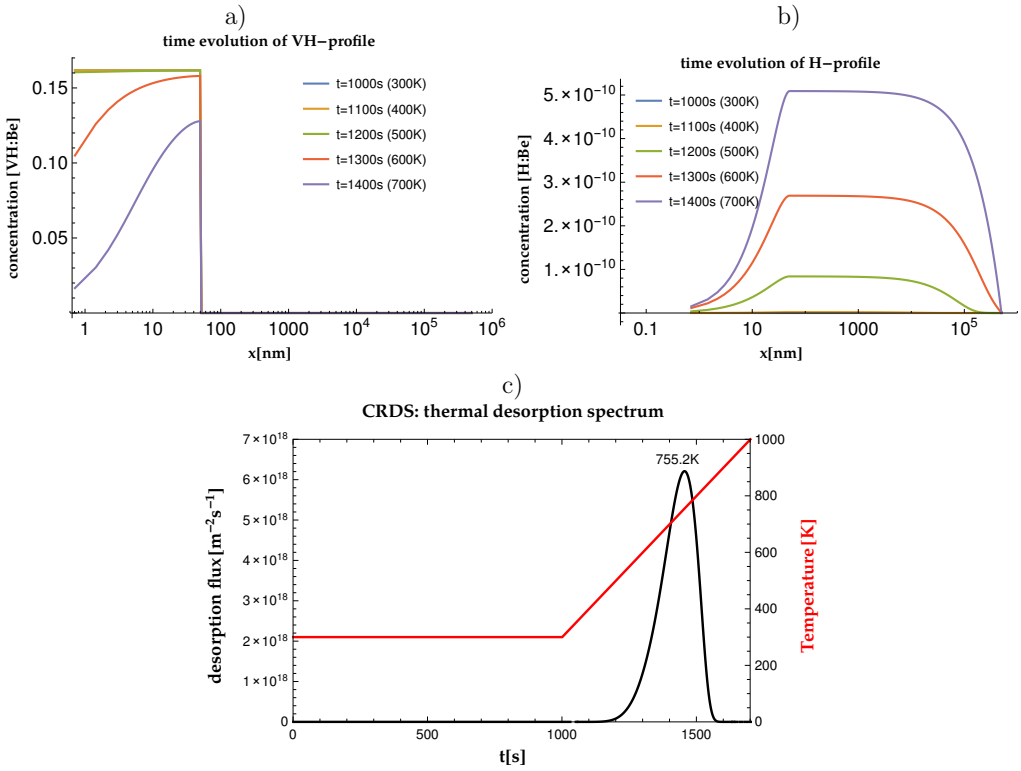

Figure 28: Calculation for the simple CRDS model. A waiting time of 1000s is used to check if the initial profile is stable. At that time a linear heating ramp starts. a) Time evolution of $c_{VH}(x,t)$, b) Time evolution of $c_H(x,t)$, c) corresponding TDS spectrum. No desorption before the start of the heating ramp is observed. Release starts above 500 K.

3.4.1. Dependence on retention profile

Different initial profiles are compared. Step-profiles that drop to zero at depth $h = 50, 100$ and 200 nm are compared along with Gaussian profiles with mean $\mu = 50, 100$ nm and standard deviation $\sigma = 25, 50$ nm, respectively. The results are shown in figure 29.

The corresponding TDS spectra show a weak dependency on the initial profile. Nevertheless, this partly explains why the high-T peak shifts to higher temperatures with increasing ion energy. Due to higher energy of the ions these are deposited deeper in the material. Furthermore, increased energy brings a higher amount of defects. This effect will be discussed below.

For the following calculations we will proceed with step profiles, because the shape of the retained hydrogen is not well known and TDS results do not strongly alter for different initial profiles.

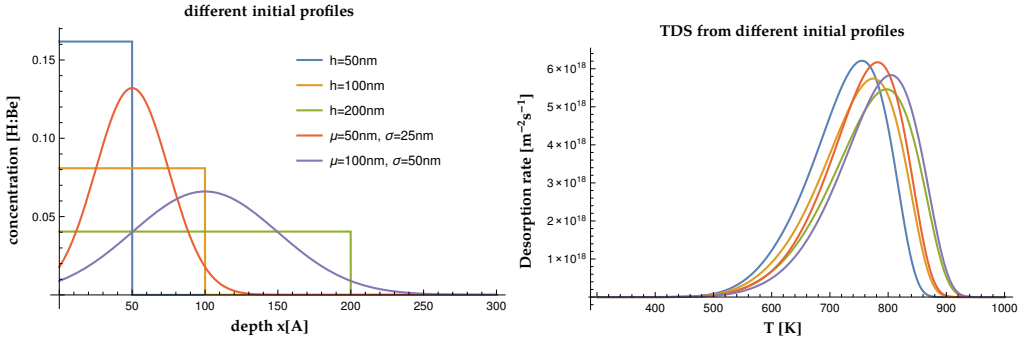

Figure 29: Left: Different initial profiles of trapped hydrogen that were investigated. Step-profiles with depth $h = 50$ nm, 100 nm, 200 nm and Gaussian profiles with mean values of 50 μm/100 μm and standard deviation $\sigma = 25$ μm/50 μm, respectively. All curves are normalized to the same amount of hydrogen $\Phi = 10^{21}$ m^{-2}. Right: Corresponding TDS spectra.

3.4.2. Dependence on diffusion constant

Next, the influence of the diffusion constant is investigated. Figure 30 shows TDS profiles for different diffusion prefactors and energy barriers that can be chosen. The parameters are chosen such that the diffusion reaches from the experimentally observed diffusivities up to values which correspond to ten times faster diffusion compared with the theoretical value. The barriers were altered in a reasonable range around the data that is indicated by DFT.

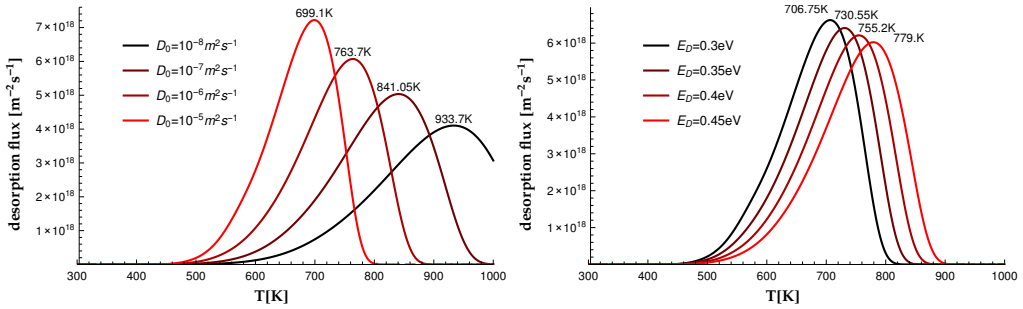

Figure 30: Left: diffusion prefactor, Right: diffusion barrier

As can be seen from these calculations, the peak position strongly depends on the diffusion constant. In order to get a well elaborated interpretation of TDS data a better estimate for the diffusion constant is clearly needed. The broad scatter of diffusion data, that is discussed above, allows peak shifts in the range of far over 200 K.

Figure 31 shows a direct comparison between the theoretical diffusion value according to (2.31) and the value by provided Abramov. The effect of crystal anisotropy on hydrogen diffusion is negligible. It is therefore sufficient to treat hydrogen diffusion in Be as an isotropic

process. Nevertheless, the choice of using Abramov's or our value has significant influence on the TDS spectra. However, this will not influence the qualitative results presented in this thesis.

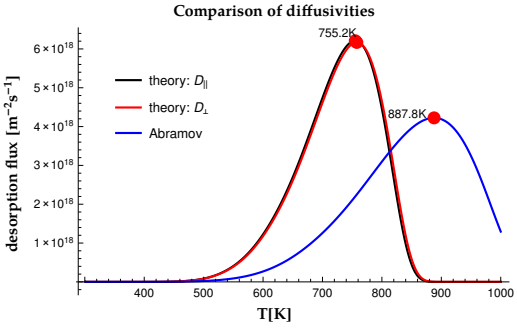

Figure 31: Influence of different diffusion constants on TDS spectra. The influence of crystal anisotropy on hydrogen diffusion is very small, whereas the difference between our prediction and Abramov's value is significant resulting in a peak position difference of above 130 K.

3.4.3. Dependence on detrapping properties

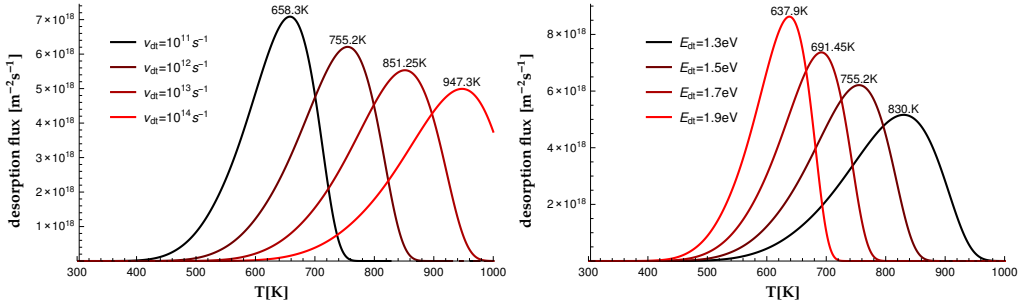

Figure 32: Left: detraping frequency factor, Right: detrapping barrier

The height of the detrapping barrier is strongly influencing the thermal release properties. The attempt frequency ν_{dt} has also a significant influence on the spectrum. Nevertheless, it is believed that it should be in the range of the Debey frequency, which sets the time scale for properties related to the lattice. In the sense that detrapping is enabled by lattice motion (phonons) which periodically alter the height of the detrap barrier it is a well-motivated assumption to set $\nu_{dt} = \nu_D \approx 10^{13}\ \mathrm{s}^{-1}$. However, it is often needed to adjust ν_{dt} to match the peak positions of experimental data. Here, $\nu_{dt} = 10^{12}\ \mathrm{s}^{-1}$ was chosen as default value.

Note, that these results hold for any kind of binding state, which not necessarily must be vacancies, as long as the detrapping from these states can be described by an Arrhenius law.

Still, the fact that the high-temperature peaks are observed in high-purity single crystalline samples indicate that the corresponding defects must be irradiation induced and since they are already observed at low fluence mono-vacancies are a very reasonable explanation for the HT-peak.

3.4.4. Dependence on (re)trapping properties

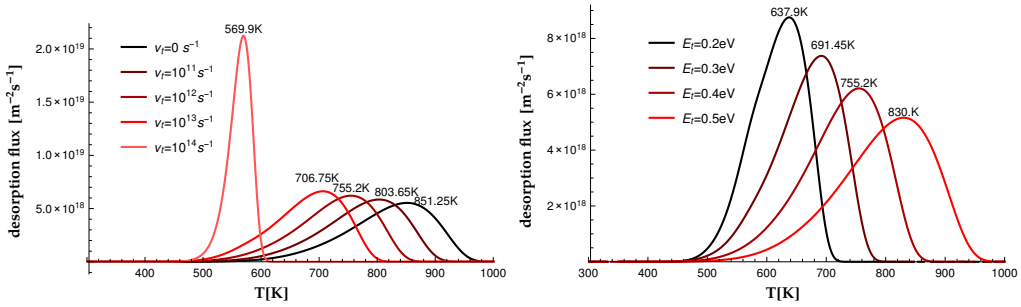

Figure 33: Left: traping frequency factor, Right: trapping barrier

Trapping is a very subtle mechanism because it greatly affects the retention properties. For the special case $\nu_t = 0$ trapping is completely disabled, which means that as soon as hydrogen is able to leave a trap side it will not be trapped again. The emission temperature is much lower and the peak very sharp. During a TDS experiment the continuous trapping and detrapping cycles strongly depend on the efficiency of trapping. The continuous trapping is usually called retrapping. The peak position of the spectrum can be altered by over $200K$ just by the (re)trapping mechanism. Therefore, the concentration of vacancies that are available for trapping plays an equally important role, which will be revisited in section 3.5.

3.4.5. Dependence on heating rate α

With increasing heating rate the peaks shift to higher temperatures, because there is less time for a reaction at a particular temperature T to happen.

Note, that integrals in this plot are not comparable, if one wants to compare integrals at different heating rates one should either consider the desorption flux vs. time diagram or scale the desorption fluxes by α^{-1}.

Experimentally, low heating ramps are more challenging because the signal measured per second by the mass spectrometers becomes very small, therefore α should be chosen so small that experimental noise in the mass spectrometers signal is still tolerable, but fine structures in the TDS spectra are not overshadowed by peaks from different reactions that might be present.

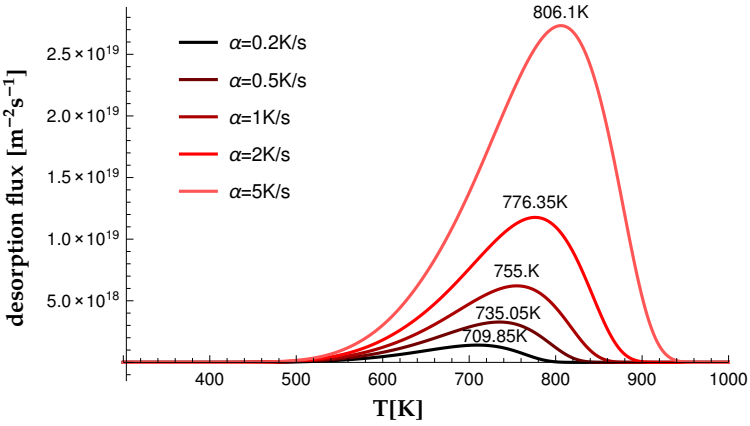

Figure 34: Heating rate

3.4.6. Dependence on fluence Φ

For this calculation it was assumed that the amount of vacancies is proportional to the amount of hydrogen that is implanted, which should hold for low fluences. The ratio was arbitrarily set as H:V=1. Due to the non-linearity of the PDE-system (3.5), the peak position changes if the amount of hydrogen and/or vacancies is modified. Figure 35 shows a shift of the maximum by roughly 60 K for fluences in the range of $10^{20} - 10^{21}$ m^{-2}. Physically, this is attributed to the increase of trapping in the large fluence calculation due to a higher absolute number of available vacancies.

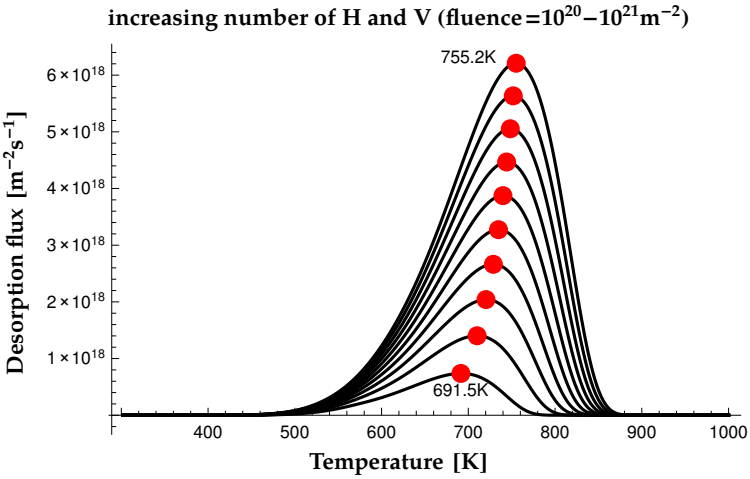

Figure 35: Peak shift due to increased amount of hydrogen and vacancies.

However, emergence of a second peak, observed in experiments under increased fluences, does not occur at the current description because no mechanism exists in the model that would allow for it. The possibility of having all binding states, i.e. vacancies, filled and remaining hydrogen in interstitial positions, would in the current description result in desorption at room temperature due to the very fast diffusion behaviour. Mechanisms that allow for retention after saturation of vacancies will be discussed in section 4.

3.4.7. Summary of parameter dependencies on TDS

Table (9) summarizes the main results in this section for the simple model studied above. The effect of each parameters on the peaks position T_{peak} and its width s_{peak} is indicated by the notation $\nearrow$= rising, $\searrow$ = decreasing.

Table 9: Summary of qualitative impact of parameters in the simple model.

Variable	Description	Influence on TDS
Φ	**fluence:** total amount of implanted hydrogen per unit area	$\Phi \nearrow \Rightarrow$ integrated hydrogen amount $\nearrow$, $T_{peak} \nearrow$ if also the amount of vacancies increases accordingly
h	**retention depth:** depth up to which hydrogen is retained in the sample, at higher depth the hydrogen concentration is essentially zero	Weak dependence on depth and shape of the retention profile, $h \nearrow \Rightarrow T_{peak} \nearrow$
α	**heating rate** temperature increase in K/s	$\alpha \nearrow \Rightarrow$ signal $\searrow$, $T_{peak} \nearrow$
D_0	**diffusion prefactor** sets the time constant for the diffusion	$D_0 \nearrow \Rightarrow T_{peak} \searrow, s_{peak} \searrow$
E_D	**diffusion barrier** sets the fraction of particles that are participating at diffusive transport	$E_D \nearrow \Rightarrow T_{peak} \nearrow$
ν_{dt}	**detrap attempt frequency** sets the time constant for the detrapping process, in first approximation it is set to the Debey frequency which gives the time constant of lattice motion	$\nu_{dt} \nearrow \Rightarrow T_{peak} \searrow$
E_{dt}	**detrap energy barrier:** sets fraction of particles able to escape trap sites	$E_{dt} \nearrow \Rightarrow T_{peak} \nearrow$, $s_{peak} \nearrow$ strong influence on peak position & width
ν_t	**trap attempt frequency:** see detrap attempt frequency	$\nu_t \nearrow \Rightarrow T_{peak} \nearrow$, $s_{peak} \nearrow$
E_t	**trap energy barrier:** see detrap barrier	$E_t \nearrow \Rightarrow T_{peak} \nearrow, s_{peak} \nearrow$

The TDS spectra strongly depend on the binding energies, i.e. the detrapping barrier, and therefore can be obtained by thermal desorption spectroscopy by comparison to the simulation.

However, other parameters like diffusivity and trap concentrations have also great influence on the peak position which makes the decision which parameters have to be chosen to match an experimental spectrum rather challenging due to the large set of parameter choices that match a single curve.

3.5. Mobile defects

From the previous discussion it is obvious that the presence of defects is directly linked to retention properties of the material. Thus, the defects motion should also be considered. A summary of published energy barriers for vacancy diffusion $E_{D,V}$, based on DFT calculations, is given in table 10.

Table 10: Summary of vacancy diffusion barriers published in the literature[a]. All values in eV.

direction	Ferry et al. [17]	Allouche [4]	Middleburgh[42]
$\|\|$ to basal plane: $[11\bar{2}0]$	0.66	0.72	0.72
$\perp$: to basal plane: [0001]	0.83	0.72	0.89

[a]The given barriers do not necessarily correspond to diffusion strictly along or perpendicular to the basal plane, but rather give the minimal barriers for transitions that can be projected onto corresponding directions

Using the values from Ferry et al. we find for the characteristic diffusion length at room temperature (assuming $D_V(T) = a_0^2 \nu_D \exp\left(-\frac{E_{D,V}}{k_B T}\right)$ for a characteristic time $t = 1000$ s)

$$\sqrt{D_V t} \approx \begin{cases} 65 \text{ nm} & \text{for } [11\bar{2}0] - \text{direction} \\ 2 \text{ nm} & \text{for } [0001] - \text{direction.} \end{cases} \tag{3.12}$$

Comparing these diffusion lengths with the typical retention depth of the order of 100 nm, we see that diffusion along the $[11\bar{2}0]$-direction is comparable with this value. In case the surface orientation is aligned with the $[11\bar{2}0]$-direction, a non-negligible amount of vacancies that is created during ion bombardment approaches the surface, which is a sink for vacancies. In the case of [0001]-orientation vacancy migration takes place parallel to the surface, in this case the vacancy diffusion length (in $[11\bar{2}0]$-direction) needs to be compared with the size of the implantation zone (3 mm$\gg$ 100 nm). A change of vacancy distribution over time at room temperature is therefore not expected for a crystal whose surface is aligned with the [0001]-direction. Note that the diffusion length scales with the square root of time, so considering even much longer times ($\approx$3 hours for ion implantation duration) will not affect the validity of the argumentation here.

In figure 36 an artificial profile of empty vacancies of depth 50 nm is allowed to diffuse. Depending on the crystal orientation, motion towards the surface happens either with barriers 0.66 eV of 0.83 eV. For a [0001]-oriented surface, diffusion of vacancies during ion exposure at room temperature is observable but not significant. As soon as the temperature ramp starts the diffusion is fast enough to significantly reduce the number of vacancies in the system. For

[11$\bar{2}$0]-direction diffusion is fast enough to remove the majority of vacancies from the system at room temperature. Note, that these calculations were done without presence of hydrogen atoms, which are thought to immobilize vacancies. However, it has not yet been studied by means of ab initio methods whether VH-complexes are mobile or not. Nevertheless, here we have shown that in principle the surface orientation can play a crucial role if it comes to defect migration of vacancies. The same argumentation holds qualitatively for grain boundaries in polycrystalline materials which offer a sink for lattice defects. Nevertheless, the influence of this effect depends strongly on the grain size. If the grain size is much larger than the typical retention depth h no significant difference to single-crystals is expected. Note, that there is a scatter among the DFT data given in table 10. Using parameters by Middleburgh would quantitatively change the defect migration. Unfortunately, experimental data for defect migration in beryllium is not available. Therefore, the discussion of defect migration and its influence on TDS spectra must remain on a qualitative level here.

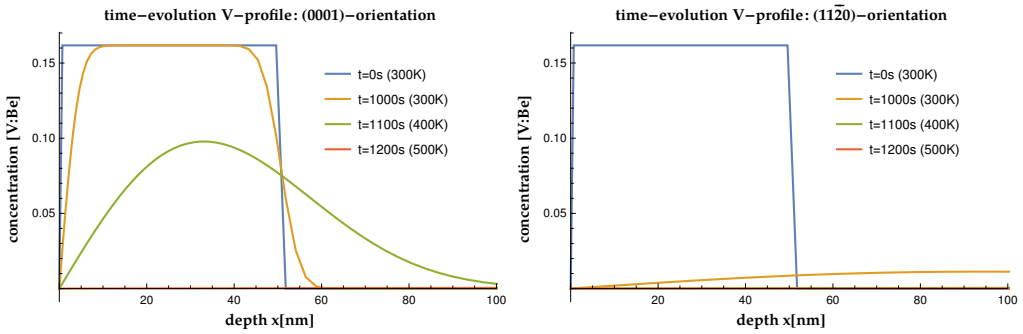

Figure 36: Time evolution of artificial empty vacancy profiles. Left: surface is [0001]-oriented. Right: surface is [11$\bar{2}$0]-oriented.

Next, we implement the vacancy diffusion in the model to study the effect on a TDS spectrum. This can be achieved by introducing a new mobile species, i.e. empty vacancies

$$\begin{cases} \partial_t c_H(x,t) &= D_H(T(t))\partial^2_{xx} c_H(x,t) - \Gamma_t + \Gamma_{dt} \\ \partial_t c_V(x,t) &= D_V(T(t))\partial^2_{xx} c_V(x,t) - \Gamma_t + \Gamma_{dt} \\ \partial_t c_{VH}(x,t) = & \qquad\qquad +\Gamma_t - \Gamma_{dt} \end{cases} . \tag{3.13}$$

Again, the desorption flux at the surfaces is calculated using

$$j_0(t) = D_H(T(t))\partial_x c_H(x,t)|_{x=0} \tag{3.14}$$

$$j_L(t) = -D_H(T(t))\partial_x c_H(x,t)|_{x=L} \tag{3.15}$$

once $c_H(x,t)$ is known.

Resulting TDS spectra are shown in figure 37 for vacancy diffusion barriers ranging from 0.5 eV to 1.7 eV. The impact on the spectra is again significant. The mechanism of vacancy

diffusion essentially takes out empty vacancies from the system, thus reducing the effect of retrapping. Note, that the curve for 0.5 eV almost coincides with spectra where retrapping was completely disabled (compare figure 33 for $\nu_t = 0\ s^{-1}$).

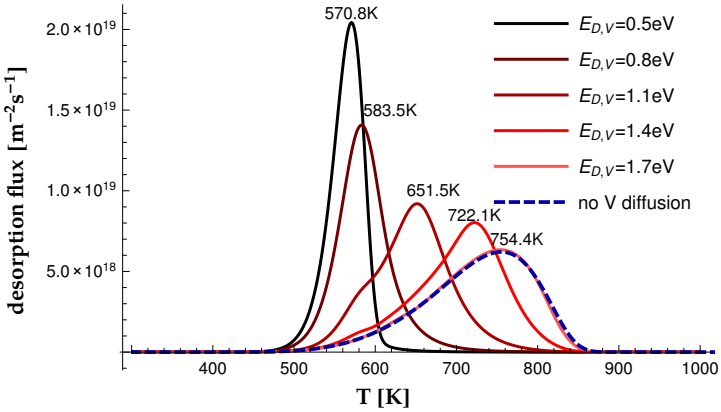

Figure 37: Effect of vacancy diffusion barrier, the reference refers to the previous calculation without vacancy diffusion term.

The influence of defect motion was also studied by Piechoczek [48], who considered self-interstitial (SIA) beryllium atoms and mono vacancies in CRDS calculations. By annihilation processes ($SIA + V \rightarrow -$) the amount of vacancies in the system is significantly changed after collision cascades. Here, we try to show how ambiguous treatment of SIA-motion and annihilation processes are. Literature values for SIA diffusion are summarized in table 11.

Table 11: Self-interstitial diffusion barriers published in the literature[a]. All values in eV.

direction	Ferry [17]	Allouche [4]	Middleburgh [42]
$\|\|$ to basal plane: $[11\bar{2}0]$	0.12	0.12	0.64
$\perp$: to basal plane: $[0001]$	0.27	0.97	0.99

[a]The given barriers do not necessarily correspond to diffusion strictly along or perpendicular to the basal plane, but rather give the minimal barriers for transitions that can be projected onto corresponding directions

With the same estimations as given above, using the values in table 11, we find using the values given by Ferry

$$\sqrt{Dt} \approx \begin{cases} 2 \text{ mm} & \text{for } [11\bar{2}0] - \text{direction} \\ 0.1 \text{ mm} & \text{for } [0001] - \text{direction.} \end{cases} \tag{3.16}$$

Which is clearly much higher than the extension of the retention zone (depth of the irradiated region), and even can compare with the size of the implantation zone (lateral extension of the irradiated sample region). If these values are trustworthy, self interstitials will move away

very fast after their creation, eventually annihilating with either vacancies, grain boundaries or surfaces. Note, that the values given in table 11 show a huge discrepancy. Taking the $\perp$-values from Allouche or Middleburgh results in diffusion length in the order of $1\mathring{A}$. The huge uncertainty regarding self-interstitial motion and having no knowledge about the rate of annihilation processes are the main reasons for not taking the ion-implantation process into account for the simulations presented in this thesis. The restriction on predefined profiles furthermore has the benefit of directly being able to link profiles to corresponding TDS spectra.

3.6. Ambiguities in earlier CRDS calculations

The latest publication on CRDS modelling by Piechoczek et al. [48] dealt with the effect of the crystal orientation on desorption spectra. The model is two-dimensional in space in order to account for anisotropic diffusion processes which occur with different speed perpendicular and parallel to the basal plane. Here we want to discuss the main aspects of the previous model and give improvement to weaknesses in the description.

$$\partial_t c_i(x,z,t) = \left(D_i^x(T)\partial_{xx}^2 + D_i^z(T)\partial_{zz}^2\right) c_i(x,z,t) + R_i(\{c\},T) + S_i(x,z,t) \tag{3.17}$$

The additional source term $S_i(x,z,t)$ can be obtained from binary collision codes like SDTrimSP [16], which allow for estimations of the depth distribution of interstitial hydrogen and defects that were created during collision cascades, such as self-interstitial Be atoms and monovacancies. However, for regions close to the saturation SDTrimSP can only match the experimental data by removing particles artificially from the simulation once the saturation starts. Therefore, we choose not to rely on Trim-data in this thesis.

In order to match the experimental spectra an additional reaction, called self-trapping, had to be introduced.

$$\mathrm{H} + \mathrm{V} \rightarrow \mathrm{VH}: \qquad \Gamma_{trap} = \nu_t \frac{c_V c_H}{c_{Be}} exp\left(-\frac{E_t}{k_B T}\right) \tag{3.18}$$

$$\mathrm{VH} \rightarrow \mathrm{H} + \mathrm{V}: \qquad \Gamma_{detrap} = \nu_{dt} c_{VH} exp\left(-\frac{E_{dt}}{k_B T}\right) \tag{3.19}$$

$$\mathrm{V} + \mathrm{SIA} \rightarrow -: \qquad \Gamma_{annihilation} = \nu_{an} \frac{c_V c_H}{c_{Be}} exp\left(-\frac{E_{an}}{k_B T}\right) \tag{3.20}$$

$$\mathrm{H} + \mathrm{VH} \rightarrow 2\mathrm{VH} + \mathrm{SIA}: \qquad \Gamma_{self-trap} = \nu_{st} \frac{c_H c_{VH}}{c_{Be}} exp\left(-\frac{E_{st}}{k_B T}\right) \tag{3.21}$$

The self-trapping reaction conserves the number of H and Be atoms and is therefore a possible mechanism. Nevertheless, the mechanism that a light hydrogen atom removes a Be atom from its lattice position into an interstitial site leaving two filled vacancies behind is very unintuitive. No predictions from ab initio data if or if not these reactions can take place are present. Table 12 gives an overview of parameters used in the simulation.

A schematic view of the simulation volume is depicted in figure 38. Due to the heavy computational expense of the two dimensional code the sample size needed to be reduced to

Table 12: Parameters used in the simulation [48]. VH-complexes were assumed to be immobile $D^x_{VH} = D^z_{VH} = 0$.

Mechanism		prefactor	energy barrier
diffusion in $(11\bar{2}0)$-direction:	H	$3.1 \cdot 10^{-6}$ m^{2}s^{-1}	0.4 eV
	V	$3.1 \cdot 10^{-6}$ m^{2}s^{-1}	0.7 eV
	SIA	$3.1 \cdot 10^{-6}$ m^{2}s^{-1}	0.4 eV
diffusion in (0001)-direction:	H	$7.7 \cdot 10^{-6}$ m^{2}s^{-1}	0.4 eV
	V	$7.7 \cdot 10^{-6}$ m^{2}s^{-1}	0.7 eV
	SIA	$7.7 \cdot 10^{-6}$ m^{2}s^{-1}	0.004 eV
trapping		10^{13} s^{-1}	0.4 eV
detrapping		$5 \cdot 10^{10}$ s^{-1}	1.7 eV
annihilation		10^{13} s^{-1}	0.4 eV
self-trapping		10^{13} s^{-1}	0.004 eV

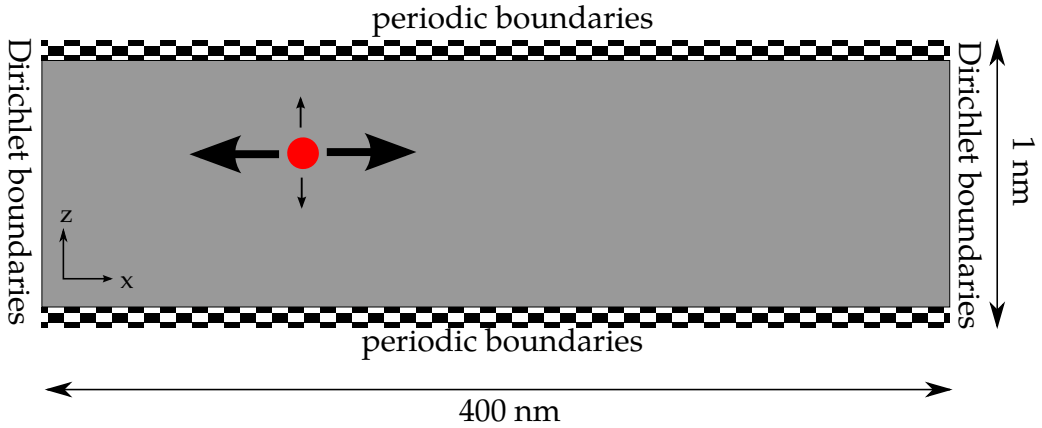

Figure 38: Simulation volume used by Piechoczek [48]. SIA motion is strongly anisotropic (here shown for (0001)-surface orientation).

$L_x = 400$ nm. The second dimension had a length of $L_z = 1$ nm, for which periodic boundary conditions were used.

Figure 39 shows comparison to experimental data obtained by Oberkofler on single-crystals with different crystal orientations. These measurements were performed at 0.7 K/s with $E_{prim} = 1$ keV/D and $E_{prim} = 3$ keV/D.

However, the second dimension in the simulation was redundant. Since the influx term was chosen to be homogeneous in z, and since the mechanisms did not have a dependence on z the profile remains homogeneous in z for all times t. We repeated Piechoczek's calculations with the one-dimensional code. Comparison is shown in figure 40. Note, that at simulation size $L_x = 400$ nm a huge desorption flux is observed at the back of the sample, which is affecting the comparibility to experiments in which a sample of size 0.5 mm is used. The reduction of complexity to one dimension drastically increases efficiency and accuracy. The

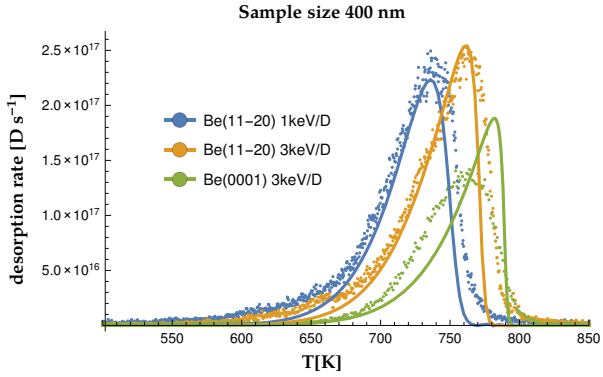

Figure 39: Experimental data and simulation results published by Piechoczek [48].

simulation cell may be chosen much larger. A comparison with simulations at 4 μm thickness shows a significantly reduced flux at the back. Unfortunately, the so obtained data lowers the agreement with experimental data compared to previous results.

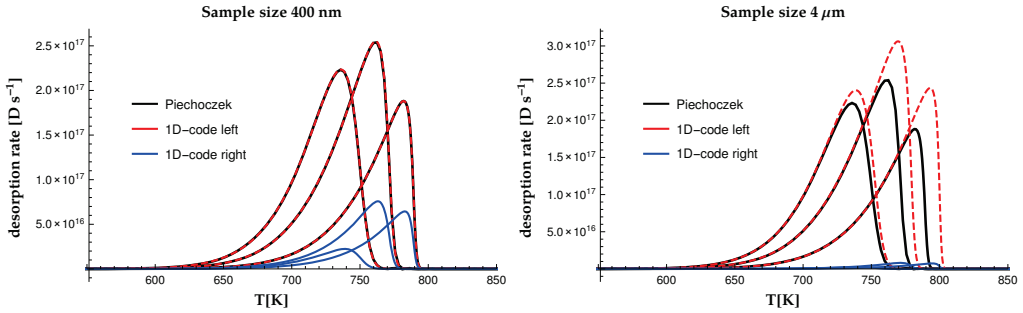

Figure 40: Repetition of Piechoczek's calculations [48] using the 1D-code. Parameters were chosen as given in table 12. Left: sample size $L = 400$ nm as in Piechoczek's calculation. The desorption flux at the rear side yields a non-negligible contribution to the total desorption. Right: sample size increased to $L = 4$ μm. The influence of rear side desorption is significantly reduced, thus increasing the desorption at the front side.

Nevertheless, the description given by Piechoczek still allows to, at least qualitatively, account for the effect of crystal orientation in simulations. Eventhough, the parameters chosen are partly baseless (SIA diffusion does not match the DFT data) and the additional reaction of self-trapping is not very intuitive. In the next chapter we will show that it can be replaced by another much clearer mechanism.

3.7. Multiple trapping

As indicated by DFT (see section 3.2), a vacancy can store up to five hydrogen atoms, the energy barriers for hydrogen release depends on the occupation number of sites within one vacancy. It is therefore expected that the mechanism of storing multiple atoms in one vacancy is relevant for interpretation of thermal desorption spectra. This process is referred to as – multiple trapping – in the following. The model is extended by additional reactions

$$\mathrm{H}+\mathrm{VH}_n \rightarrow \mathrm{VH}_{n+1}$$
$$\mathrm{VH}_{n+1} \rightarrow \mathrm{VH}_n + \mathrm{H} \text{ for } 0 \leq n < 5$$

that account for the different energy barriers depending on the occupation of sites within vacancies.

Accordingly, the additional trapping and detrapping processes are thermally activated processes, which increases the parameter space even further. A similar derivation as given in section 3.3 holds

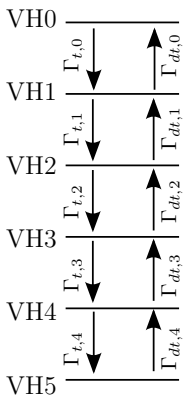

$$\Gamma_{t,n} = V_t \nu_{t,n} \exp\left(-\frac{E_{t,n}}{k_B T}\right) c_H c_{VHn}, \tag{3.22}$$

$$\Gamma_{dt,n} = \nu_{dt,n} \exp\left(-\frac{E_{dt,n}}{k_B T}\right) c_{VHn}. \tag{3.23}$$

Nevertheless, the reaction rate should only alter due to the barriers corresponding to different filling levels. The reaction prefactor should be comparable. Therefore we state: $\nu_{t,n} = \nu_t$ and $\nu_{dt,n} = \nu_{dt}$. For trapping the barrier height is below the diffusion barrier, therefore we set the value for the trapping reaction equal to the value of the diffusion barrier, which then is the rate-limiting process for trapping.

$$\begin{cases} \partial_t c_H & = D_H \partial^2_{xx} c_H + \sum_{i=1}^{5} \Gamma_{dt,i} - \sum_{i=0}^{4} \Gamma_{t,i} \\ \partial_t c_{VH_0} & = D_V \partial^2_{xx} c_{VH_0} + \Gamma_{dt,1} - \Gamma_{t,0} \\ \partial_t c_{VH_1} & = -\Gamma_{dt,1} + \Gamma_{dt,2} - \Gamma_{t,1} + \Gamma_{t,0} \\ \partial_t c_{VH_2} & = -\Gamma_{dt,2} + \Gamma_{dt,3} - \Gamma_{t,2} + \Gamma_{t,1} \\ \partial_t c_{VH_3} & = -\Gamma_{dt,3} + \Gamma_{dt,4} - \Gamma_{t,3} + \Gamma_{t,2} \\ \partial_t c_{VH_4} & = -\Gamma_{dt,4} + \Gamma_{dt,5} - \Gamma_{t,4} + \Gamma_{t,3} \\ \partial_t c_{VH_5} & = -\Gamma_{dt,5} + \Gamma_{t,4} \\ c_i(x=0,t) & = c_i(x=L,t) = 0 \quad \text{(BC)} \\ c_i(x,t=0) & = c_i(x) \quad \text{(IC)} \end{cases} \tag{3.24}$$

The total number of hydrogen atoms within the system

$$N_H = \int_0^L c_H + c_{VH_1} + 2c_{VH_2} + .. + 5c_{VH_5} dx \tag{3.25}$$

is indeed a conserved quantity. This can be checked, according to the derivation given in (3.8), by taking the time derivative. Insertion of (3.24) (all trapping and detrapping terms cancel out) leads to

$$\partial_t N_H = \int_0^L D_H \partial_{xx}^2 c_H dx \tag{3.26}$$

$$= D_H \partial_x c_H \big|_{x=0}^{x=L} \tag{3.27}$$

$$= -j_0(t) - j_L(t). \tag{3.28}$$

So the change of particle number per unit area is given by the fluxes at the surfaces at $x = 0$ and L, as expected.

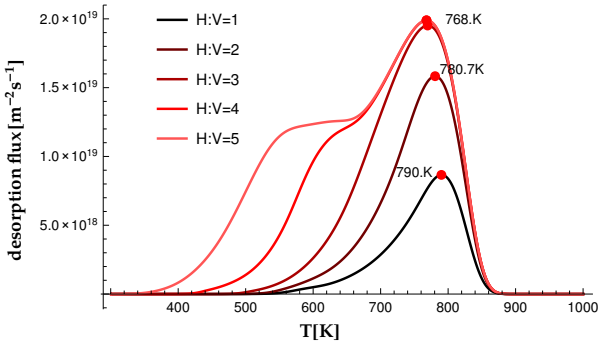

Figure 41: For each calculation the initial profile is kept a step profile with vacancies filled to level n for H:V= n.

The simulation in figure 41 was done for different initial profiles in which each with different initial filling level. E.g. for H:V=1 the system contains $\Phi_V = 10^{21}$ m^{-2} vacancies, each filled with a single hydrogen atom and for H:V=2 each vacancy contains 2 hydrogen atoms. It was made sure that this artificial choice had no big influence on the TDS spectra. Different simulations where all hydrogen, initially in interstitial positions, was allowed to relax, therefore yielding a distribution of different filling levels (partially VH_1, VH_2, etc.), resulted in similar spectra. The binding states corresponding to VH_4 and VH_5, which belong to filled T_2 sites, are different in nature compared to the states with filled BT_V sites, which have comparable energy. Therefore, a shoulder left of the high-T peak emerges which corresponds to the lower binding energies of 1.20 and 1.05 eV.

Not only does multiple trapping yield a shoulder to the high temperature peak, it also gives a steep decay at the right flank of it. Therefore, the mechanism of multiple trapping is a very convenient substitution in the model for the rather unintuitive self-trapping reaction.

A limit exists for the number of hydrogen that can be stored in the system, i.e. $\Phi_H = 5\Phi_V$ where $\Phi_H = \int_0^L (c_H + \sum_{n=1}^5 n c_{VH_n}) dx$ and $\Phi_V = \sum_{n=0}^5 \int_0^L c_{VH_n} dx$. Any additional hydrogen, that will be stored in interstitial sites, immediately flows out during relaxation time, which corresponds to the implantation time in the experiment. Therefore, yielding a reduction of the total retention. A plausible mechanism for the reduction of retention that is seen for high

fluences can thus be suggested: the total amount of vacancies in the system is saturated at a certain fluence, limiting the amount of hydrogen that can be stored within the sample. Other mechanisms like partial opening of gas-filled channels in the material are also plausible.

We will revisit this topic in section 4.

3.8. Comparison to experimental data for low fluences

An attempt to reproduce a set of TDS spectra obtained by Oberkofler [45] by means of the current CRDS model is shown in figure 42. The steep decay at the righthand side could be achieved due to the multiple trapping mechanism. Thus an entirely physically motivated model description for experimentally observed data is given.

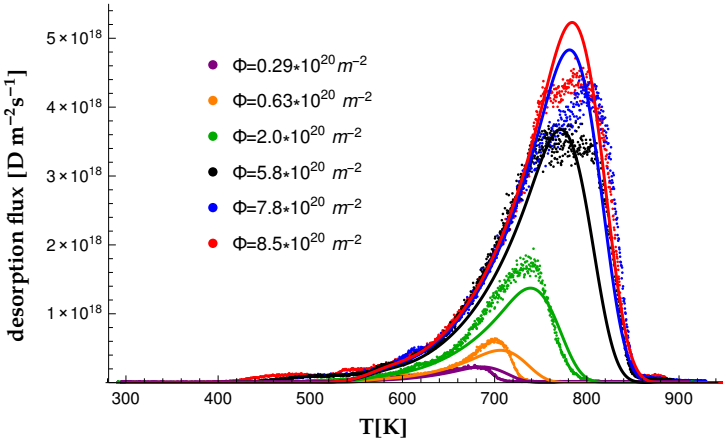

Figure 42: Direct comparison between data provided by M. Oberkofler [45] to CRDS-simulations for the low-fluence regime. To reproduce the data vacancy diffusion had to be omitted, indicating that vacancy diffusivity is much slower than predicted by DFT calculations. The experimental TDS spectrum was divided by the implantation area $A = 12$ mm^2 (value given by Oberkofler) for comparison with the simulation.

The parameters that were used are shown in table 13. The detrapping frequency has to be chosen one order of magnitude below the Debey frequency and the detrapping energies needed slight adjustment compared to previously discussed values. For the initial distribution it was chosen that all hydrogen is stored each in a vacancy. Note, that the TDS spectrum does not change significantly, if the distribution alters to a combination of VH_1, VH_2 and VH_3 states, due to the similar barriers for these states.

3.9. Conclusion

The introduction of binding states, of whatever kind, solves the contradiction between very low retention depth and the fast diffusivity of hydrogen in the sample in ion implantation

Table 13: Parameters used in the simulation. Diffusion constant was chosen slightly lower (40%) compared to the previous cases due to the better fit to experimental data.

Mechanism		prefactor	energy barrier
diffusion in $[11\bar{2}0]$-direction:	H	10^{-6} m^{2}s^{-1}	0.4 eV
	V	-	-
trapping[a]		$72\mathring{A}^3 \cdot 10^{13}$ s^{-1}	0.4 eV
detrapping		10^{12} s^{-1}	1.5, 1.45, 1.4, 1.20, 1.05 eV
Experimental parameters			
fluence Φ		chosen as in the experiment	
initial profile		step-profile with depth $h = 50$ nm (H:V=1)	
heating rate α		0.7 K/s	
sample size		$L = 0.5$ mm (like in the experiment)	

[a]See section 3.3.2 for the explanation of the volumetric multiplier in the prefactor.

experiments. In particular, mono vacancies provide very efficient trap sites for hydrogen atoms. The fact that the HT-peak is observed in high-purity single crystalline materials suggests that this peak is caused due to defect creation by keV ions, thus mono vacancies are expected to be produced. According to DFT calculations these provide binding energies up to 1.5 eV which is sufficient to explain the high temperature desorption.

Parameter studies were provided which revealed that the amount of vacancies in the system has a significant influence on the peak position in TDS spectra. The diffusivity of vacancies seems to be contradictory to experiments due to the complete disabling of retrapping. Either vacancy diffusion barriers are much higher than suggested by DFT data or vacancies get immobilized by other mechanisms, e.g. cluster formation. Unfortunately, the amount of data provided by DFT for systems with more than one vacancy is rather scarce. Divacancies were shown to be unstable unless hydrogen is present [17]. If the so formed divacancies release hydrogen at comparable temperatures compared to mono vacancies, the picture would still be the same. Hydrogen gets detrapped, divacancies dissemble and leave the sample due to fast V diffusion. In case that larger clusters of vacancies are stable even without hydrogen, these could solve the problem of the lack of retrapping in the presence of vacancy diffusion. Unfortunately, this speculation is baseless at this point.

It was shown that experimental curves can be reproduced if no vacancy diffusion is assumed. A satisfactory description of experimental data that includes vacancy diffusion without strong alternation of other parameters (e.g. detrapping barrier) could not be achieved.

4. Surface effects

Desorption from the bulk material into the vacuum involves the recombination of hydrogen atoms on the surface, which may provide the rate-limiting step in the sequence of reactions in a TDS experiment. In this section the extension of the previous model by surface processes will be assessed.

The experiment performed by Lossev & Küppers [37] who have studied the desorption from a Be(0001)-surface reveal a desorption peak at 450 K which is remarkably close to the low-temperature peaks of $[11\bar{2}0]$-oriented Be observed in ARTOSS experiments. Therefore, we investigate whether desorption from hydrogen on the surface can explain the emergence of low temperature peaks in TDS spectra at high fluences and if yes, investigate why it does not show up at low fluences.

First, a review of the experiment performed by Lossev & Küppers is given. An analytical solution to first and second order desorption with temperature evolution from hydrogen-covered surfaces is given, which indicates that the desorption rate, as indicated by Lossev & Küppers, is probably too fast. The CRDS-model is then readily extended to account for the phenomenology of surface accumulation of hydrogen isotopes by introducing energetic barriers at the surface.

The presence of surface barriers gives rise to the emergence of a low-T state that is visible in TDS, which is also stable at room temperature. Nevertheless, the model fails to give satisfactory explanation of the reduction of retention with increasing fluence, which was reported by many experiments. Possible explanations are discussed.

4.1. Desorption from Be(0001)-surface

Lossev & Küppers [37] adsorbed low-energy (thermal 1600 K) atomic deuterium D on a beryllium surface. The measurement was done for a) an oxidized surface and repeated for b) a surface that was sputtered with argon ions. The amount of residual oxygen on the cleaned surface was estimated as 0.1 monolayers. A schematic setup of the experiment and the results of the TDS measurement are shown in figure 43.

It has shown that, unlike molecular hydrogen, atomic hydrogen does adsorb endothermically on beryllium with a sticking coefficient near one. Lossev & Küppers report a desorption from the Be(0001)-surface according to eq. (4.1), which was obtained from data of the desorption peak near 450 K from the cleaned Be-surface, with desorption rate factor $\kappa_{des} = 10^{-8}\ m^{-2}$ and desorption barrier of $E_{des} = (0.87 \pm 0.09)$ eV

$$\frac{d\sigma(t)}{dt} = -\kappa_{des} exp\left(-\frac{E_{des}}{k_B T}\right)\sigma(t)^2. \tag{4.1}$$

$\sigma(t)$ denotes the surface concentration of deuterium atoms per unit-area. The desorption is therefore a process of second order, which is in agreement with the expectation because for desorption from the surface the reaction $H + H \rightarrow H_2$ must take place which involves two particles.

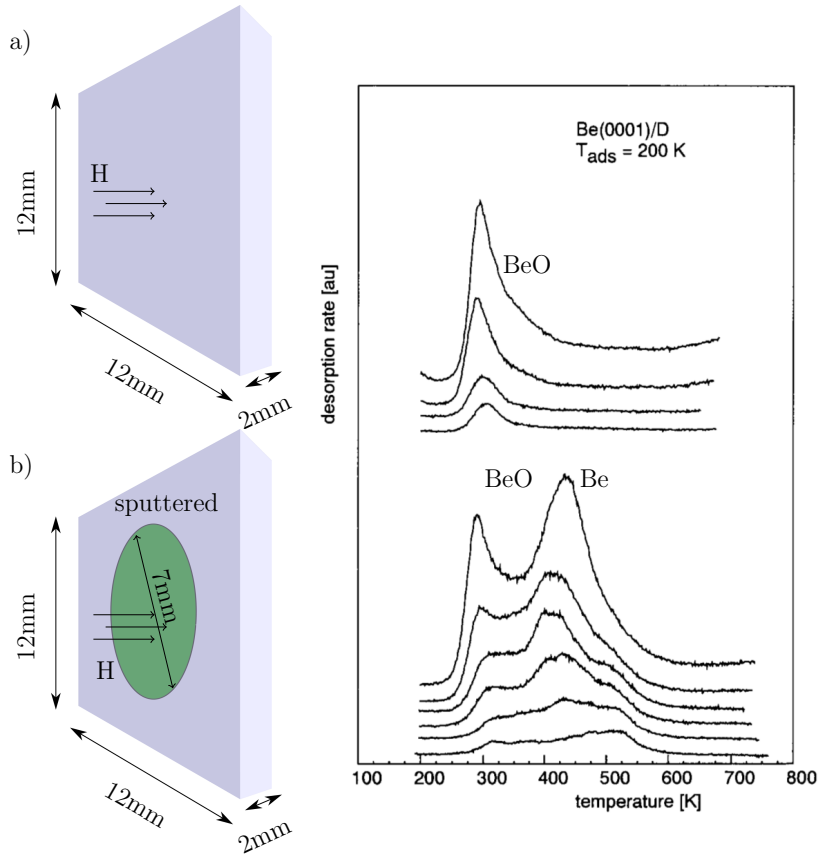

Figure 43: Schematic view of the experimental procedure performed by Lossev & Küppers [36] (on the left). Atomic D is adsorbed on a) oxidized surface b) partially cleaned Be(0001)-surface. TDS was performed starting from $T_0 = 200$ K with heating ramp $\alpha = 2.5$ K/s. The lower set of TDS curves (on the right) corresponds to the cleaned Be surface that reveals an additional hydrogen release peak at 450 K compared to the oxidized surface (the upper set of curves) where only one peak at 320 K is observed. Different curves in each set correspond to different exposure times. Experimental data plot is taken from [36]

The experiment has shown a sticking coefficient near 1 on either the oxidized and the clean surface for atomic deuterium D, whereas D_2 adsorption was not observed. The peak position is approximately at 450 K. After 80 L (1 Langmuir $= 1.33 \cdot 10^{-4}$ Pa s) of exposure they estimate the saturation coverage of the surface of $1.1 \cdot 10^{19} D/m^2$ which corresponds to a D:Be-ratio of roughly 50%, considering only Be atoms from the first monolayer.

Similar desorption curves were observed for the H_2 and HD signals, excluding an isotope effect.

Direct recoil spectrometry measurements, which are only sensitive for the first monolayer, performed by Zalkind et al. [58] confirm that the majority of adsorbed hydrogen is located on the surface region instead of subsurface layers.

In the following, we will give surface coverages in fractions of the theoretical maximum surface density $\sigma_{max} = \sigma_{Be(0001)}$ which refers to a coverage of 1 hydrogen atom per Be atom at the surface [8]. Other authors have slightly different values for the maximum coverage, e.g. $\sigma_{max} = 4/3\sigma_{Be(0001)}$ [3]. Above the maximum coverage instantaneous desorption of hydrogen molecules takes place.

According to the adsorption and desorption behaviour and the results from the previous chapter a schematic energy profile of hydrogen in beryllium which holds for low surface coverage can be sketched like shown in figure 44.

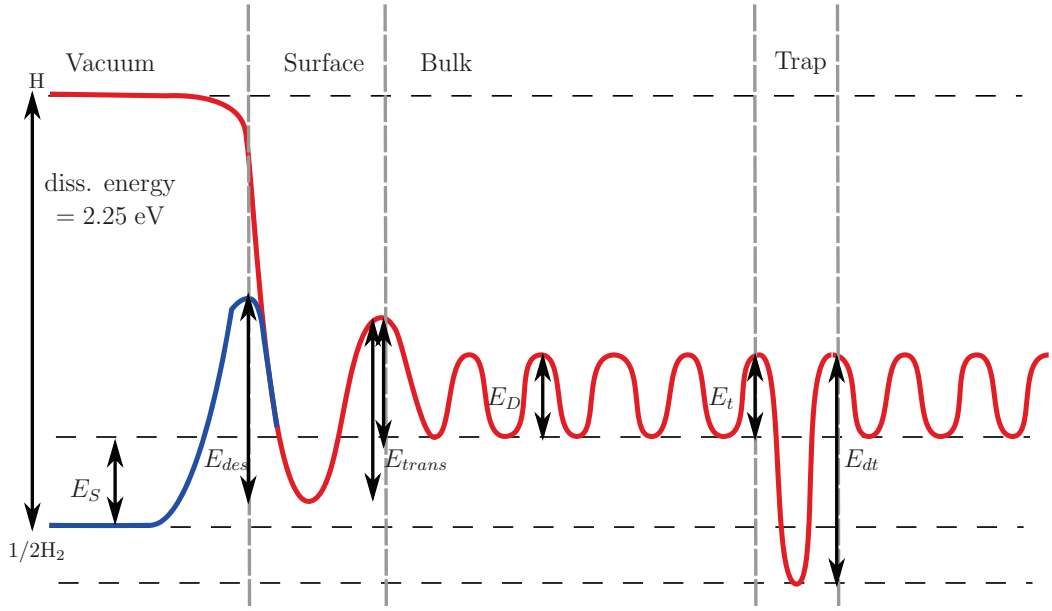

Figure 44: Schematic energy profile for hydrogen in beryllium. Different energy barriers are present: diffusion E_D, trapping in vacancies E_t, detrapping from vacancies E_{dt}, transition between bulk and surfaces sites E_{trans}(may be different depending on the direction), desorption E_{des}, solution energy E_S

4.2. Analytic treatment of second order desorption processes

In this section an analytical treatment of the desorption process for second order desorption is given [4]. An exact solution for the desorption flux can be calculated. We will investigate the

[4] A similar approach can be used to calculate the desorption flux based on first-order desorption processes. The derivation is given in Appendix A.3.

case of a linear heating ramp $T(t) = T_0 + \alpha t$.

Experimentally, it was found that the desorption behaviour follows a second-order thermally activated process

$$\frac{d\sigma(t)}{dt} = -\kappa(T(t))\sigma(t)^2, \tag{4.2}$$

$$\kappa(t) = \kappa_{des} \exp\left(-\frac{E_{des}}{k_B(T_0 + \alpha t)}\right), \qquad \kappa_{des}, E_{des} > 0 \tag{4.3}$$

$$\sigma(0) = \sigma_0. \tag{4.4}$$

This is a non-linear ordinary differential equation which indeed has a simple solution.

First, we consider the temperature-independent case (no heating ramp $\alpha = 0$)

$$\frac{d\sigma(t)}{dt} = -\kappa\sigma(t)^2. \tag{4.5}$$

We obtain the solution

$$\sigma(t) = \frac{\sigma_0}{1 + \sigma_0 \kappa t}, \tag{4.6}$$

which can be checked by inserting into (4.5).

This motivates the ansatz $\sigma(t) = \frac{\sigma_0}{1+\sigma_0 f(t)}$ with t-dependent coefficient, which has the same functional form except for a general time-dependent function in the denominator. Inserting into (4.2), we find

$$\sigma(t) = \frac{\sigma_0}{1 + \sigma_0 \int_0^t \kappa(T(t'))dt'} \tag{4.7}$$

as solution for the problem with given temperature evolution. Again, this can be checked by insertion in (4.2).

In the case of a linear heating ramp we encounter an integral of the form (2.52) which was assessed above for the case of temperature-dependent diffusion.

Accordingly we find

$$\int_0^t \kappa(T(t'))dt' = \frac{\kappa_{des} E_{des}}{\alpha k_B} \Gamma\left(-1, \frac{E_{des}}{k_B(T_0 + \alpha t)}, \frac{E_{des}}{k_B T_0}\right). \tag{4.8}$$

The desorption flux is equal to the instantaneous rate of change of the surface occupation

$$j_{des}(t) = \frac{d}{dt}\sigma(t) = \kappa(T(t))\sigma(t)^2 \tag{4.9}$$

$$= \kappa_{des} \exp\left(-\frac{E_{des}}{k_B T(t)}\right) \left(\frac{\sigma_0}{1 + \sigma_0 \frac{\kappa_{des} E_{des}}{\alpha k_B} \Gamma\left(-1, \frac{E_{des}}{k_B T(t)}, \frac{E_{des}}{k_B T_0}\right)}\right)^2. \tag{4.10}$$

The result for different initial coverage levels using the parameters $\kappa_{des} = 10^{-8}$ m^{2}s^{-1} and $E_{des} = 0.87$ eV, as reported by Lossev & Küppers, is shown in figure 45. Until ≈ 300 K no

desorption takes place. Note, that the reported peak position is badly reproduced when using the proposed parameters. For half coverage ($\sigma_0 = 0.5\sigma_{max}$) the peak is at 371.1 K (experiment 450 K). Shifting the energy barrier by the provided error (which leads to $E_{des} = 0.96$ eV does also not yield a peak position that is in agreement with the experimentally determined value, which indicates that the given parameters are wrong. Desorption should be slower in order to match the experimental data.

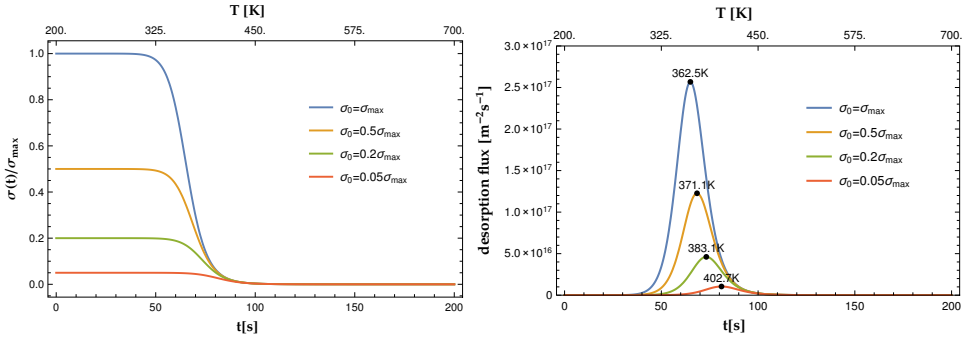

Figure 45: Desorption simulation using the same parameters as Lossev & Küppers: $\alpha = 2.5\ K/s, T_0 = 200K$. Linear heating starts at $t = 0$. Left: time evolution of surface occupation for different initial occupations. Right: corresponding TDS spectrum. The peak temperatures are lower than the experimentally observed value (450 K).

Figure 46 shows a curve for the following desorption form

$$\frac{d\sigma(t)}{dt} = -2 \cdot 10^{-9} m^2 s^{-1} \cdot \sigma(t)^2 exp\left(-\frac{1.0\ eV}{k_B T}\right) \tag{4.11}$$

which fits the peaks position for half-coverage well.

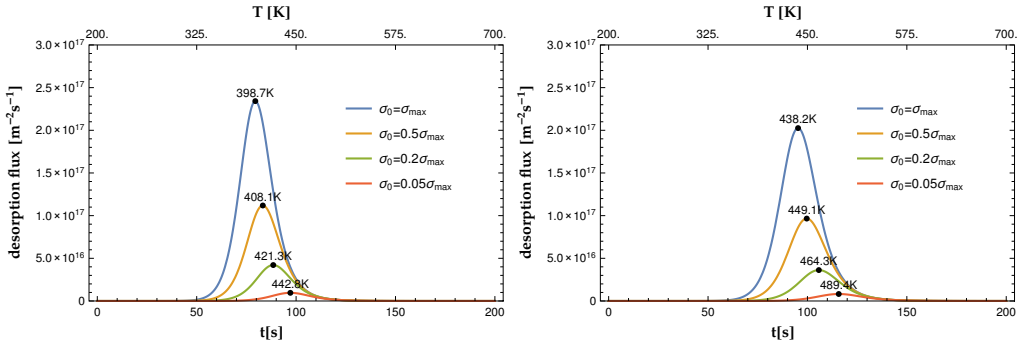

Figure 46: Left: desorption energy shifted by experimental error ($E_{des} = 0.96$ eV). Right: $E_{des} = 1.0$ eV, $\kappa_{des} = 2 \cdot 10^{-9}$ m^{2}s^{-1}

Using these parameters it is also useful to investigate how fast desorption at room temperature is. Figure 47 shows the time evolution of hydrogen surface coverage over four months ($\approx 10^7$ s). Using the parameters provided by Lossev & Küppers significant desorption occurs during the first 1000 seconds.

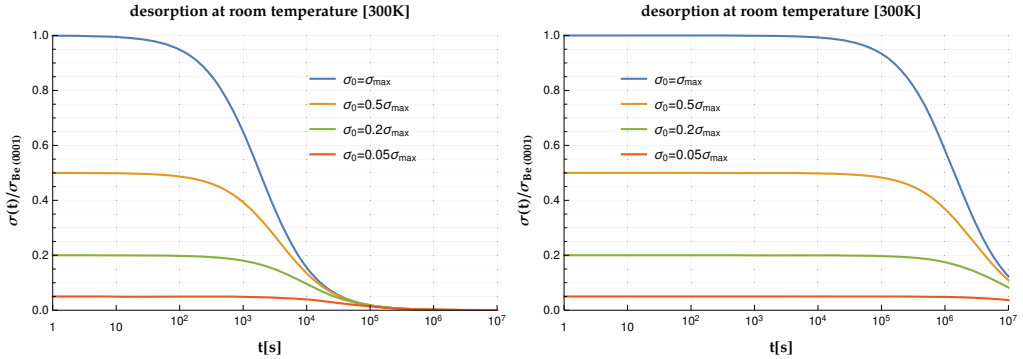

Figure 47: Desorption from hydrogen covered surfaces at room temperature. Left: using the parameters provided by Lossev & Küppers a significant amount of hydrogen desorps on the time scale of hours. Right: for $\kappa_{des} = 2 \cdot 10^{-9}$ m^{2}s^{-1}, $E_{des} = 1.0$ eV significant reduction is seen after some months.

Note, that Reinelt verified that the LT-peak in ARTOSS experiments remains unchanged during 15 hours of post-implantation waiting time at room-temperature (compare figure 7). Therefore, if we assume that the LT-peak is caused by desorption of hydrogen from the surface, then Lossev & Küppers values cannot be correct. In reverse conclusion, if their parameters are correct then the low temperature peak in implantation experiments cannot be caused by surface desorption. However, if the surface desorption is indeed slower, room temperature desorption is not observed on this time scale and the surface hypothesis remains a valid explanation.

The ARTOSS setup also allows to perform similar experiments as done by Lossev & Küppers under even better defined conditions. It is therefore recommended to repeat these. If desorption at room temperature is observable, then the hypothesis of surface desorption as explanation for the LT-peak is falsified.

4.3. Comparison between low temperature peak and surface desorption

The similarity in peak position of surface desorption and the LT-peak states the question if the nature of the latter one can be caused by surface desorption.

Therefore, as a first check the fitting of a second order desorption process (4.9) to the LT-peak is assessed. However, this procedure is difficult due to the previously discussed inhomogeneous implantation profile that was used in the experiments by Reinelt, resulting in partially oversaturated regions whereas other regions remain below the saturation threshold. The resulting TDS spectra then contains a superposition of contributions from all regions as schematically depicted in figure 48. Therefore, the data is not useful for quantitative analysis.

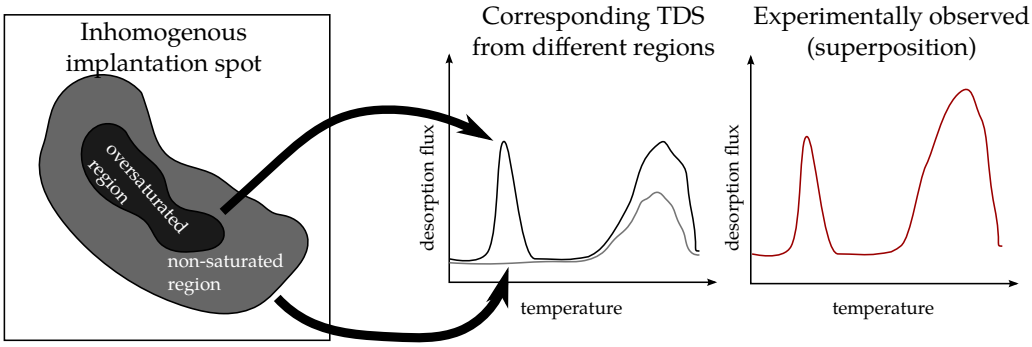

Figure 48: Effect of inhomogeneous implantation profiles. Contributions from regions that were exposed to different fluences are observed simultaneously in an experiment.

Unfortunately, no other data for single-crystalline samples is available. Therefore, we use data by M. Oberkofler obtained from polycrystalline samples [43] shown in figure 49. Differences in TDS spectra of single- and polycrystalline materials were found to be small for implantation at low fluences [45]. Here we try to outline why this should also hold for high fluences.

The effect of grain boundaries can in principle change the outcome of the measurement. However, the grain size of roughly 10 μm (in the used sample) is much larger than the retention depth ($\sim$ 100 nm). We have seen that due to binding in vacancies the in-depth diffusion is effectively disabled. Due to the isotropy of hydrogen diffusion we can therefore also assume that diffusion in lateral direction is also not significant. Only hydrogen in very close vicinity of grain boundaries (some nanometres) can reach grain boundaries (at room temperature). Therefore, the majority of hydrogen that is implanted is trapped in the grains, which then acts like retention in a single crystal with particular surface orientation, the fraction of hydrogen in grain boundaries is much smaller. Also desorption from different crystal surface orientations can lead to different desorption temperatures, still the peak position is very comparable to the position of the peak found by Reinelt (compare figure 5), just the height is much larger. The height difference can be explained in two different ways: a) experimental issue: due to the strongly inhomogenous implantation profile in Reinelt's measurement the fraction of oversatured area is comparable to undersaturated regions, superposition of desorption from these regions yields a comparable HT-peak (which is present in both regions) but a reduced LT-peak (which appears only in the super-saturated case), b) trapping and fast desorption in grain-boundaries yields desorption that corresponds to a LT-peak. However, b) can be excluded because the LT-peak does not show up at low fluences. Therefore, the height-difference in the LT-stage between Reinelt's single-crystalline and Oberkofler's polycrystalline sample can only be attributed to the inhomogeneous implantation profile. According to this argumentation we state that there is no conceptual difference visible in the LT-stage between single- and polycrystals. We suggest to verify this experimentally, by repeating Oberkofler's experiment with a single-crystal sample keeping the ion exposure as homogeneous as possible in the implantation region.

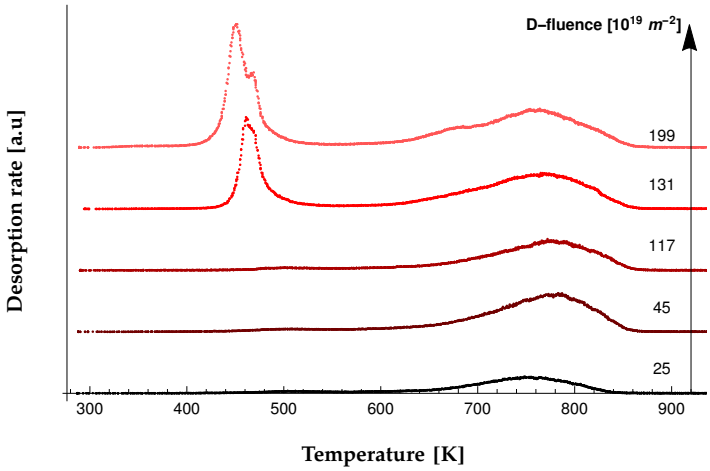

Figure 49: Data by M. Oberkofler using polycrystalline Be [43]. $E_{prim} = 1$ keV/atom, $\alpha = 0.7$ K/s, implantation area $A = 4 \times 4$ mm^2. Threshold fluence between $1.17 - 1.31 \cdot 10^{21}$ Dm^{-2}, 0.3 ML oxide layer, 10 μm grain size

The amount of hydrogen in the low-temperature stage can be obtained by integration over the desorption signal for temperature range $300 - 550$ K taking into account the (well-defined) implantation region of $A = 16$ mm^2. This results in $1.6 \cdot 10^{20}$ m^{-2} and $2.6 \cdot 10^{20}$ m^{-2} for the two low-temperature peaks in figure 49. Comparison to the surface density of Be atoms on the (0001)-surface $\sigma_{Be(0001)} = 2.2 \cdot 10^{19}$ m^{-2} indicates that the amount of hydrogen desorped in the low-temperature stage cannot originate from an undisturbed surface. To desorb the observed amount of hydrogen from surfaces the area must be increased by at least one order of magnitude. Atomic force microscopy (AFM)-measurements performed by Reinelt allowed for determination of the surface roughness, which exceeded the nominal area by 15 ± 5 % [51]. This surface roughening was caused by the repeated ion bombardment during ion implantation and annealing cycles. However, the AFM measurement could only resolve objects larger than ~ 10 nm. Any roughness on scales smaller than that, e.g. the 1.1 nm "bubbles" observed in the bulk by Markin et al. by TEM studies [40] or channels connecting to the surface of similar size could still be present to increase the surface area that can be covered by hydrogen atoms. Markin et al. suggested that the bubbles form an interconnected network that eventually connects to the surface, effectively increasing the surface area tremendously. Figure 50 shows a scheme of a material surface that allows for such a surface increase. For our model this case can simply be considered by using a much larger surface area.

Now we check if the curves obtained by second order desorption (4.9) can be brought into agreement with the low-temperature peak. We use the values $E_{des} = 1$ eV and $\kappa_{des} = 2 \cdot 10^{-9}$ m$^2 s^{-1}$, that reproduced the peak position for the data by Lossev & Küppers. We assume that the initial surface coverage is equal to the saturation value reported by them, i.e. half-coverage $\sigma_0 = 0.5\sigma_{Be(0001)} \approx 1.1 \cdot 10^{19}$ m^{-2}. The occupied area A is then determined such

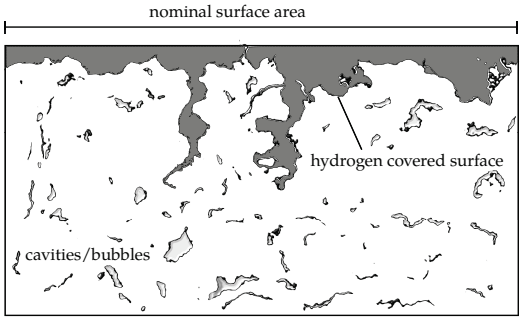

Figure 50: Schematic view of material surface

that the total amount of hydrogen in the model is equal to the amount in the experiment, the desorption rate [Ds^{-1}] is then given by $Aj_{des}(t)$. The result is shown in figure 51.

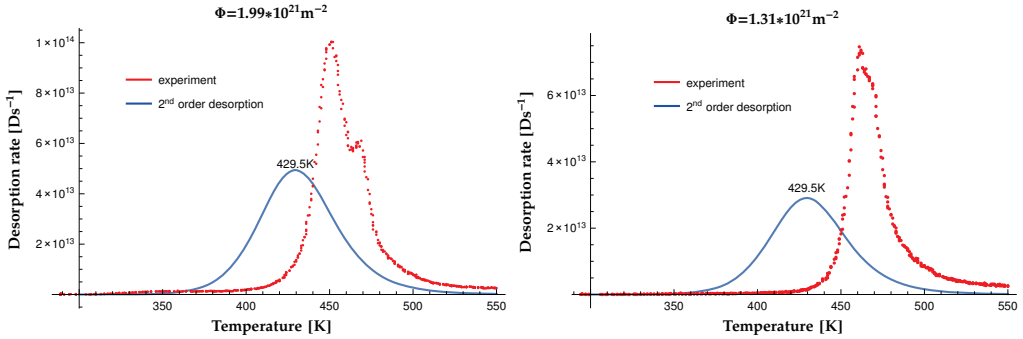

Figure 51: Comparison for second order desorption according to (4.9) with the LT-peak observed in ion-implantation experiments.

The agreement is rather bad. Note, that the change in peak position with respect to figure 46 is caused by the different heating rate. Attempts to fit (4.9) by a least square-method varying E_{des} and κ_{des} did also not lead to satisfactory results. Also higher initial concentrations σ_0 did not improve the results.

Furthermore, the possibility of first-order desorption was also considered, which results in narrower peaks. The deriviation of the corresponding desorption flux is given in appendix A.3. A reasonable fit is shown in figure 52.

The peak width is comparable to the experimental data. However, the asymmetry of the peak is not reproduced. The experimental data shows a steep rise at low T and and smooth decay at higher T, for the first order desorption the opposite is true.

No satisfactory agreement could be achieved using either first or second order desorption behaviour. It must be assumed that the exact peak shape cannot be reproduced by surface desorption processes or the form of the desorption function is fundamentally different.

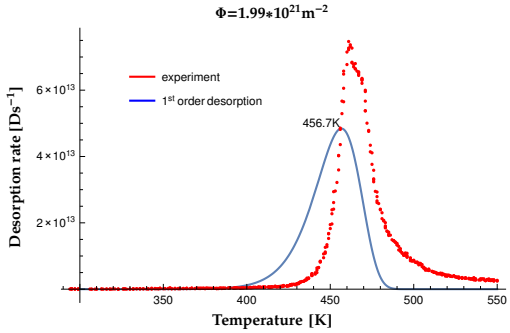

Figure 52: Best fit result obtained by a fitting with first order desorption curve.

4.4. Extension of the CRDS model by surface effects

As indicated by gas loading experiments by Lossev & Küppers [37] there exists a certain energy barrier on the surface of the sample which prevents desorption of atomic hydrogen. Therefore, the CRDS model is extended to account for accumulation of hydrogen atoms on the surface area and allow for its molecular desorption which depends on temperature and surface occupation, i.e. by the functional form of (4.2). We have seen that the exact peak form of the LT-peak cannot be reproduced by fitting the experimental data by first or second order desorption terms. However, it will be shown that many experimental features can be explained on a qualitative level by surface effects. Furthermore, the extension of the CRDS code by surface effects extends the variety of experiments that can be modelled, e.g. adsorption experiments.

Introduction of a flux limiting process at the surface can be modelled by using Neumann boundary conditions

$$\partial_x c_H(x,t)|_{x=0} = \frac{j_0(t)}{D(T(t))}, \tag{4.12}$$

$$\partial_x c_H(x,t)|_{x=L} = -\frac{j_L(t)}{D(T(t))}. \tag{4.13}$$

In the previous description the fluxes $j_0(t)$ and $j_L(t)$ were determined by the gradient of the concentration field, here the opposite holds. We state expressions for the fluxes and the boundary condition is adjusted accordingly. In the end this is needed to conserve the total particle number. Again, the sign for $j_{0/L}(t)$ is chosen such that the flux is positive for flow direction pointing from bulk to surface.

The surface occupation $\sigma(t)$ is introduced (on front and back of the sample: $\sigma_0(t)$ and $\sigma_L(t)$), i.e. hydrogen atoms per unit area on the surface. The time evolution of $\sigma(t)$ is given by the sum of fluxes

$$\frac{d\sigma_0(t)}{dt} = j_0(t) - j_0^{des}(t), \tag{4.14}$$

$$\frac{d\sigma_L(t)}{dt} = j_L(t) - j_L^{des}(t). \tag{4.15}$$

The main idea is, that hydrogen may diffuse through the bulk but as soon at it reaches the surface it may occupy empty sites on the surface. The description of processes in the bulk remains unchanged (see (3.24)). If the surface is saturated with hydrogen, i.e. if there are no empty sites, the flux from bulk to surface must go to zero. This phenomenology is accounted for by using the following form

$$j_x(t) = \nu_{trans} a_0 \exp\left(-\frac{E_{trans}}{k_B T}\right)\left(1 - \frac{\sigma_x(t)}{\sigma_{max}}\right) c(x,t), \qquad \text{with x} = 0 \text{ or } x = L. \tag{4.16}$$

The rate of the transition (bulk $\rightarrow$ surface) is determined by the frequency ν_{trans}, which is as first bias set to the Debey frequency. To account for the dimensionality of a flux a constant of dimension length is added, i.e. the lattice constant a_0.

Hydrogen occupies free sites at the surface and may desorb into the vacuum if a H_2 molecule can be formed. This needs a certain amount of energy.

$$j_x^{des} = \kappa_{des} \exp\left(-\frac{E_{desorb}}{k_B T}\right) \sigma_x(t)^2, \qquad \text{with x} = 0 \text{ or } x = L. \tag{4.17}$$

A schematic view of the energy profile of the material (Figure 44) is reproduced in figure 53 with the variety of mechanisms that affect hydrogen retention and release depicted. As in the previous studies hydrogen may diffuse through the bulk and binding in the vicinity of vacancies takes place. From the subsurface layers the atoms may migrate to the surface. Desorption from the surface to the vacuum happens by recombination of two atoms. The opposite effect of chemisorption of hydrogen molecules is also depicted. However, experimentally it is found that for beryllium this does not occur [37], apparently the energy barrier for chemisorption is too high. However, the current implementation of the code also allows for extensions to take adsorption processes into account. The model outlined here has the same functional forms as the models discussed by Pick & Sonnenberg [46] and Baskes [9] for hydrogen desorption from metal surfaces.

The model is based on the following idea: vacancies and self-interstitial atoms are produced during collision cascades during ion implantation. The amount of hydrogen in vacancies is directly linked to the integrated HT-peak, which does not grow arbitrarily large for rising fluences. In the range of the saturation region Φ_c the amount of vacancies is therefore limited to some saturation value. This maximum amount of vacancies can be estimated to be 20 % of the critical fluence threshold Φ_c because each vacancies can store up to five hydrogen atoms. As soon as $\Phi > \Phi_c$ further hydrogen cannot be stored in vacancies. Saturation is reached.

To study the fluence dependence of the new model, we choose a somewhat artifical setup. The vacancies in the systems are provided according to a given step profile of depth $h = 50$ nm.

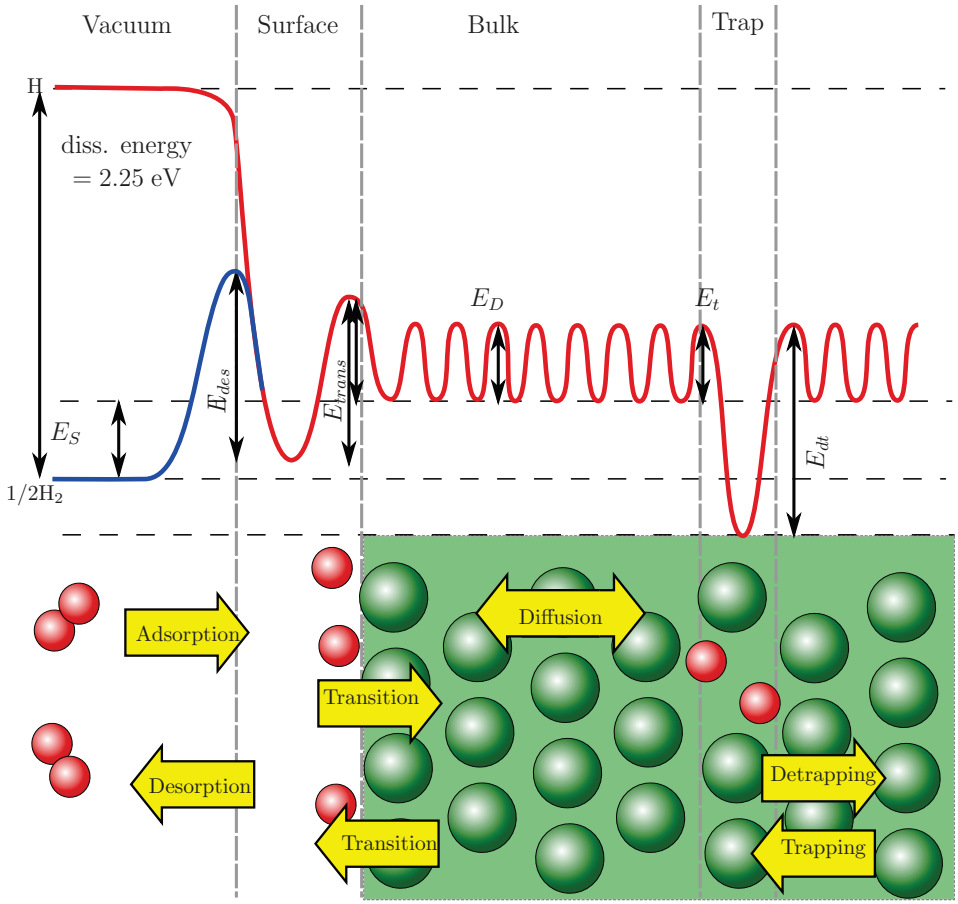

Figure 53: Schematic view of the energetic profile of hydrogen in Be with key processes indicated.

The amount is chosen such that $\Phi_c \approx 10^{21}$ m^{-2} hydrogen atoms can be stored in the vacancies, i.e. $\int_0^L c_V(x, t = 0)dx = 2{\cdot}10^{20}$ m^{-2}. The hydrogen atoms are then provided by a volume source term $S_H(x, t)$ $[m^{-3}s^{-1}]$ for a duration of $t_{pulse} = 500$ s. With this choice of the configuration, hydrogen that is provided to the system at the start of the implantation is certainly trapped. Once all vacancies are filled, additional hydrogen migrates in interstitial positions and may populate the surface region, i.e. on walls of channels, this is favored by the very fast diffusivity. In order to be able to store enough hydrogen on surfaces we increased the nominal surface by a factor of 40. The calculation was done for fluences ranging from $\Phi = 0.2 - 1.4 \cdot 10^{21}$ m^{-2}, with expected saturation above $\Phi = 10^{21}$ m^{-2}. The result is shown in figure 54, other parameters are summarized in table 14. In order to separate the high- and low-temperature peaks the

detrap frequency has to be reduced. Furthermore, the detrap energies for the 4^{th} and 5^{th} hydrogen atom per vacancy has to be raised slightly.

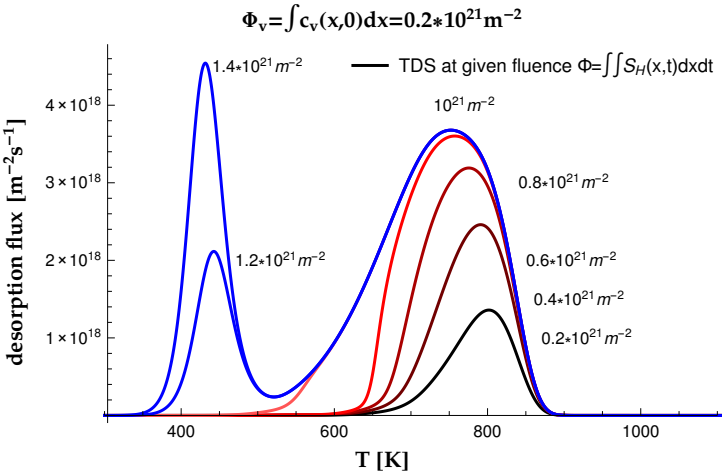

Figure 54: CRDS simulation including surface effects for different fluences. As soon as vacancies are saturated hydrogen may occupy other binding states, here the surface. Fluences of the different calculations as labels at the corresponding curves. Simulation parameters are given in table 14.

Table 14: Parameters used in the simulation. Detrapping properties had to be adjusted to seperate low- and high-temperature peak.

Mechanism	prefactor	energy barrier
diffusion H	$\frac{1.89}{\sqrt{2}} \cdot 10^{-6}$ m^{2}s^{-1}	0.4 eV
V	-	-
trapping	$72\mathring{A}^3 \cdot 10^{13}$ s^{-1}	0.4 eV
detrapping	10^{11} s^{-1}	1.5, 1.45, 1.4, 1.30, 1.30 eV
transition	10^{13} s^{-1}	0.4 eV
desorption	$2 \cdot 10^{-9}$ m^{2}s^{-1}	1.0 eV

Simulation parameters	
fluence Φ	$0.2 - 1.4 \cdot 10^{21}$ m^{-2}
initial vacancy profile	step-profile with depth $h = 50$ nm
hydrogen source term	gaussian: center at 30 nm and width 15 nm
heating rate α	0.7 K/s
sample size	$L = 0.5$ mm

Indeed, the simulation shows saturation of the high-temperature region as indicated experimentally. Hydrogen populates the surface which leads to the LT-peak as soon as all vacancies

are filled. The LT-peak rises with increasing fluence (in accordance with experiments by Haasz et al. [24]). The evolution of the surface coverage is depicted in figure 55. As soon as vacancies are filled, hydrogen migrates through the bulk and eventually reaches the surface. For the chosen parameters there is no significant hydrogen desorption at room temperature. Desorption starts at ≈ 380 K.

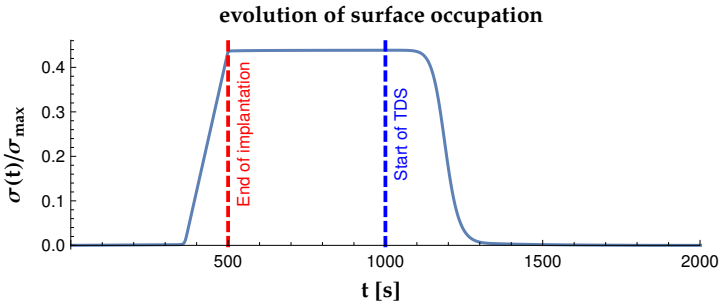

Figure 55: Time-evolution of surface coverage during the simulation for highest fluence $\Phi = 1.4 \cdot 10^{21}$ m^{-2}.

The extension of the model by surface effects introduced some new parameters for desorption (E_{des} and κ_{des}) and for bulk-surface transition (ν_{trans} and E_{trans}). The latter two were found to have no big influence (for reasonable choices of the parameters) on the high temperature peak because at high temperatures the transition does not significantly hinder the flux from bulk to surface. Therefore, the previous discussion of parameter studies for the model with Dirichlet boundary conditions still holds.

The effect of the desorption parameters were studied independently from CRDS modelling in the previous section.

The current model allows for a qualitative comparison to experiments done by M. Reinelt (shown in figure 5). The result is shown in figure 56. In order to match peak positions of the low- and high-temperature desorption stage, adjustments to the parameters presented in table 14 have to be done. The detrap barriers of the 4^{th} and 5^{th} hydrogen per vacancy are reduced to 1.2 eV and 1.15 eV, respectively. Furthermore, the simulation allowed for diffusion of empty vacancies with barrier 0.83 eV. As discussed in section 3.5 this leads effectively to a shift of the HT-peak to lower temperatures. This was compensated by reducing the detrap frequency to $\nu_{dt} = 5 \cdot 10^9$ s^{-1}.

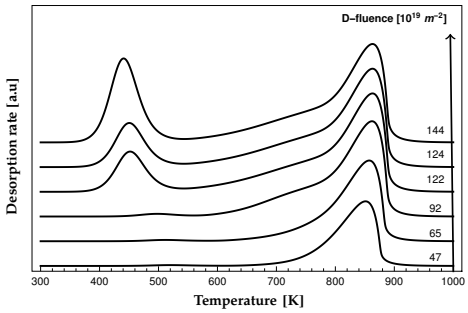

Figure 56: Simulation of measurements by Reinelt [50] (cf. figure 5).

A direct comparison to experimental data is not possible due to the previously discussed inhomogeneities in the implantation profile (Section 4.3). Still, the important features of the experimental data can be reproduced qualitatively.

4.5. Coverage dependant desorption barrier

The model still lacks the reduction of retention with rising fluence which is observed above the critical threshold Φ_c as shown in figure 8. Principally, this can be caused by room-temperature desorption from the sample surface. However, if we allow for room temperature desorption the low-temperature peak in this model will vanish after sufficient waiting time. Which stands in contradiction to the experiment. However, in a more realistic description the desorption barrier should also depend on the local concentration σ. Therefore, a desorption behaviour of the form

$$j^{des} = \kappa_{des} \exp\left(-\frac{E_{des}(\sigma)}{k_B T}\right) \sigma^2 \tag{4.18}$$

is suggested.

This description allows desorption to happen at low temperatures if the concentration is high enough. However, the exact form of $E_{des}(\sigma)$ is unknown. Nevertheless, it can be assumed that in the case of low-coverage the desorption barrier is approximately constant and drops to zero (recombination even at 0 K) for maximum coverage. Assuming continuity yields a curve like shown in figure 57. The functional form used here is $E_{des}(\sigma) = E_{des}(0)\,(1 - \exp\,(-5\,(1 - \sigma/\sigma_{max})))$ which however has no physical meaning. The rate of the decay is an estimation and is used for impact studies on TDS spectra for which we use the same parameters as given in table 14. The validity of the calculation from the last section is still given because even for the highest fluence the surface coverage did not exceed 40%, which results only in small deviations from 1 eV.

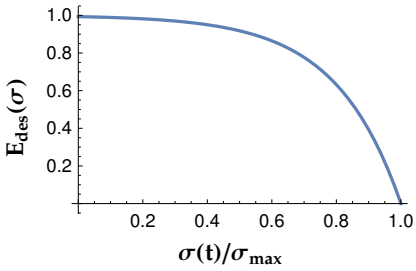

Figure 57: Hypothetical function trace of the desorption barrier.

Figure 58 shows the time evolution of the desorption flux for fluences ranging between $0.2 - 4 \cdot 10^{21}$ m^{-2}. Hydrogen is implanted into the sample for 500 s like in the previous calculation. For additional 500 s the sample is kept at room temperature to observe the desorption. Comparing to a real experiment this time can be thought of as being part of the implantation time, for which no desorption measurements are possible. At $t_{ramp} = 1000$ s the heating ramp starts and the TDS is obtained as usual. Like in the previous description, for low fluences the vacancies in the bulk are populated, then as saturation sets in the surface gets filled. Once the surface concentration is high enough to significantly reduce the desorption barrier, room temperature desorption starts. For this calculation the equilibrium surface coverage of 60% is found, which is just the amount where no more significant desorption occurs.

The amount of hydrogen that is retained in the sample (before the TDS starts) can than be calculated from $\int_{t_{ramp}}^{t_{end}} j_0^{des}(t)dt$, or alternatively by integrating the bulk concentrations at t_{ramp}. It equals 100% of the implanted hydrogen for low fluences. Note, that the saturation of the sample sets in a little above the critical threshold Φ_c not directly at the threshold. Which is also visible in figure 8.

The description indeed allows for desorption at room temperature by keeping a finite low temperature peak in the spectra. This also holds for much longer waiting times, e.g. months, due to the increase of the barrier with decreasing coverage. However, there is a major drawback in this model. The release of hydrogen from the LT-states starts for high fluences as soon as the temperature ramp starts, i.e. at 300 K, which is not observed experimentally. For much longer waiting times between implantation and heating this still holds. This could only be cured in the model by assuming desorption barriers which are not continuous with respect to the coverage, which however is not physical. Therefore, this solution is also not satisfactory.

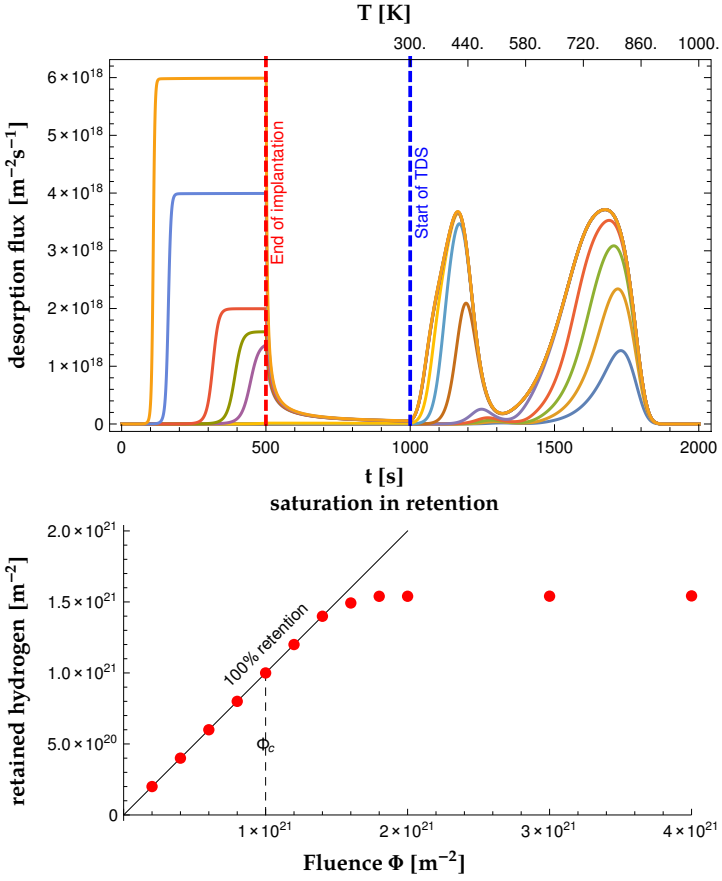

Figure 58: Top: desorption behaviour of sample with fixed amount of vacancies with different levels of hydrogen filling $\Phi = 0.2 - 4 \cdot 10^{21}$ m^{-2}. As soon as all vacancies are filled and the surface reaches saturation, hydrogen desorbs into the vacuum (at room temperature), which reduces the retained amount of hydrogen. A finite LT-peak remains. Bottom: evolution of the retention with the amount of implanted hydrogen. The decrease in the retention is visible above Φ_c (cf. Figure 8).

4.6. Conclusion

The experiment by Lossev & Küppers shows that hydrogen desorption from a Be(0001)-surface yields a desorption spectrum with peak position remarkably close to the position of the low temperature desorption peak in ion implantation experiments. However, there are strong indications that the parameters provided by Lossev & Küppers might be incorrect.

The amount of hydrogen in the low temperature peak was found to be $\approx 2 \cdot 10^{20}$ m^{-2} for measurements with polycrystalline samples by Oberkofler, which exceeds the amount of Be atoms in the first monolayer, and therefore also the possible maximum of hydrogen on the surface, by one order of magnitude. Therefore, a much larger surface has to be assumed, which can only be caused by surface deformation on nanometer scale because Reinelt reported 15% surface increase due to surface roughening for measurements on scale above ≈ 10 nanometers.

It was shown that the low temperature peak cannot be quantatively reproduced by the form

$$j^{des}(t) = \kappa_{des} \exp\left(-\frac{E_{des}}{k_B T}\right) \sigma^n(t) \tag{4.19}$$

for first ($n = 1$) or second order ($n = 2$) desorption.

Extension of the CRDS model to account for hydrogen agglomeration on surface sites was presented by introducing Neumann boundary conditions that allow for hydrogen migration from bulk to the surface under certain restrictions. The desorption from surface sites is then given by (4.19) which allows for the emergence of a low temperature desorption stage. The properties of the high-temperature peak remain mostly unaffected by the extension of the model. Therefore, the discussions from the previous chapters are still applicable.

Introduction of a desorption barrier which depends on the surface coverage allows hydrogen desorption at room-temperature if the coverage is high enough. This mechanism gives rise to desorption during ion implantation. The desorbed hydrogen reduces the total amount of retained hydrogen in the sample. The saturation of retention is observed above the critical threshold Φ_c that was defined by saturation of available vacancies.

However, this mechanism introduces a major drawback: desorption of the LT peak starts at the beginning of the temperature ramp which stands in contradiction to the experimental observations.

5. Discussion and summary

This master thesis provides a model for description of hydrogen retention and release properties in beryllium based on rate equations. Ab initio data by various groups was presented that gives insight into atomistic processes, which built the fundament for development of a 3D-random walk Monte Carlo code. Based on analytic results and refinements using the random walk code a theoretical description of diffusion was presented. Analytic solutions were provided for diffusion and surface desorption in presence of a linear heating ramp.

The CRDS model was re-built from scratch and parameter studies for the simple setup were performed revealing the complexity of the simulations due to the large parameter space which has influence on peak positions. Extension of the model by multiple trapping led to a satisfactory substitution for the previous self-trapping mechanism. The extension of the CRDS model by surface effects allows for a description of agglomeration and desorption of hydrogen on the surface which is able to yield a qualitative description of many properties that are also observed experimentally.

In the following sections we will summarize the different mechanisms that were studied in this thesis and suggest possible experiments in order to settle open questions.

5.1. TDS features & their possible explanation

Here we summarize our understanding about the mechanisms that lead to the TDS spectra that were observed experimentally. Since other hypotheses for the emergence of the LT-peak — hydride and bubble formation — were not assessed in this thesis, we will discuss them briefly.

Surface hypothesis:

The different retention mechanisms that are involved in this model are summarized in figure 59. At low fluence the amount of vacancies increases linearly with amount of hydrogen atoms ($\propto$ fluence) due to collision cascades caused by the keV hydrogen ions that are implanted in the sample. The amount of vacancies is then reduced by annihilation processes with self-interstitial Be atoms and surfaces or grain boundaries. The treatment of these mechanisms is very ambiguous due to the lack of knowledge of reaction rates. However, it has to be assumed that the amount of vacancies comes to saturation after a certain fluence. Experimentally, this can be observed in the saturation of the HT-peak, which does not grow arbitrarily large for rising fluences. With rising fluence the ratio H:V rises, which yields formation of higher occupation numbers of the vacancies. In TDS spectra this can be observed in the shoulder left from the HT-peak, e.g. seen in figure 5 and 49. The mobility of these vacancy-hydrogen complexes is still an open question. For our model these were assumed to be immobile.

With the saturation of all existing vacancies in the retention region hydrogen migrates through the bulk in the interstitial sites. Due to the very fast diffusion most of the interstitial hydrogen approaches the nearby surface where it accumulates. Desorption at room-temperature is believed to be not present for low coverages (contradiction to Lossev & Küppers parameters). This surface also must be much larger than the nominal surface of the implantation zone, which can only be explained by nanostructure deformation of the material due to stress in the material from the implantation and the present hydrogen atoms. The low

temperature peak in TDS spectra therefore is caused by desorption from hydrogen covered surfaces. The peak does not emerge at low fluences due to the effective trapping of hydrogen in vacancies and the fact that the keV-ions penetrate some nanometers into the material before they are in energetic equilibrium with the surrounding atoms and trapped in defects. Therefore, accumulation of hydrogen at the surface cannot take place until saturation of a majority of vacancies in the system is reached.

Finally, the reduction of retention is then caused by a partial desorption from the surface during ion implantation if a certain surface coverage is exceeded. In the model this is achieved by introduction of the occupation-dependence of surface barriers E_{des}.

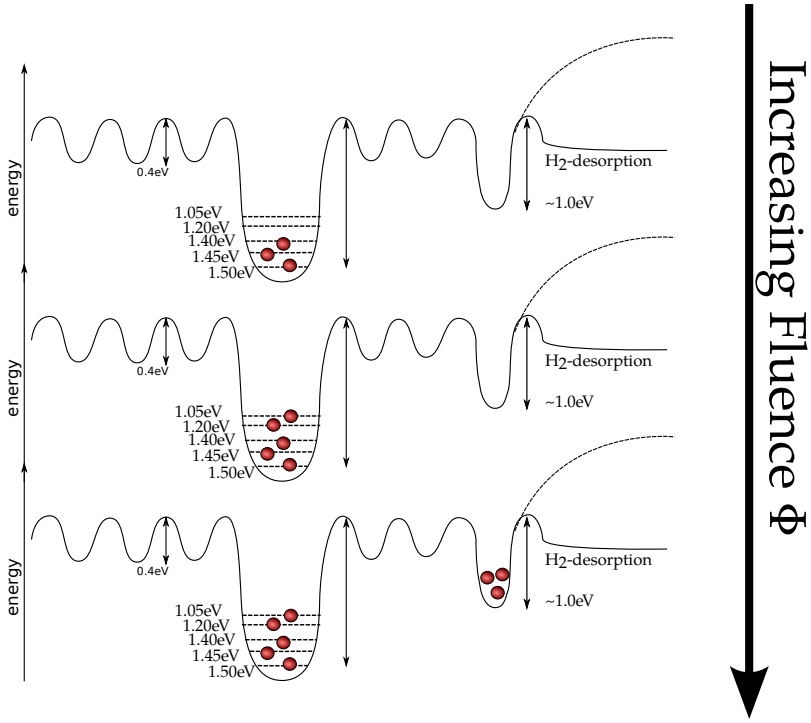

Figure 59: Schematic representation of different retention mechanisms. At small fluences vacancies are filled, then surface sites are populated.

The model however fails to reproduce the low-temperature peak quantitatively. Neither first nor second order desorption processes can be brought into agreement with the LT peak. Furthermore the introduction of the occupation-dependent barrier states the issue that the LT-peak starts to desorp at the beginning of the heating ramp which stands in conflict with the experimental data.

In conclusion, the explanation of the low temperature peak by surface desorption proved to be particularly problematic even though a huge amount of experimental features can be explained by this hypothesis.

Hydride formation hypothesis:

It is common to all descriptions that the retention mechanism at low fluence is dominated by vacancy trapping. With increasing fluence the concentration of hydrogen in the retention zone increases. At some point the concentration is high enough to modify the chemical composition of the material such that phases of beryllium hydride occur. The treatment of, most-likely amorphous, BeH_2 structures (also other stoichiometries are imaginable) is up to now very challenging by means of DFT calculations due to the vast amount of possible configurations. Due to the lack of reliable DFT data, a CRDS modelling of beryllium hydride systems is up to now without any basis.

It is reported that BeD_2 is unstable at relatively moderate temperatures. At approximately 540 K BeD_2 decomposes into its elements Be and D_2 [14]. So the emergence of the LT-peak is here linked to a decomposition process of the material instead of detrapping from binding states.

Gas bubble hypothesis:

Here the idea is that hydrogen filled vacancies agglomerate to larger vacancy clusters which then contain hydrogen in atomic and/or molecular form. It is rather challenging to model these systems by means of DFT, however for the 'smallest bubble', i.e. a divacancy, some calculations were done by Ferry et al. [17]. Her data indicates that a pair of adjacent vacancies is unstable and decomposes into two seperate vacancies. However the divicancy is stabilized by presence of hydrogen atoms. Therefore, also larger clusters of vacancies could be imaginable.

This hypothesis is supported by the experiment provided by Alimov [2] which reveals that hydrogen is retained in atomic form in beryllium for low fluences and in both, atomic and molecular form, above the critical fluence Φ_c. TEM measurements by Chernikov et al. [12] also revealed that structural deformation of Be at higher temperatures is present. At room temperature they reported cavities of up to 0.7 nm in diameter. The idea of partial connection between the bubbles and eventually also the surface provide channel systems which then would also be beneficial for the surface hypothesis which demands a strongly increased surface area. The partial connection to the surface then leads to a gas release during ion implantation which explains the observable reduction of retention above Φ_c.

In a TDS experiment the LT-peak is then explained by a combination of two processes — the desorption from channel walls and the breaking of bubbles in the bulk which release the molecular hydrogen. The cracking is triggered due to the temperature increase which yields stress in the material and a raised pressure inside of the gas-filled bubbles. Therefore, the two-peak substructure of the LT-peak, which is observed in some of the experiments, can be related to the two different mechanisms.

In this model also surface effects play a role. Therefore, the presented CRDS code is also partially usable for this mechanism.

A summary of properties commonly observed in TDS spectra is summarized in table 15 and depicted in figure 60.

Table 15: Summary of properties of thermal desorption spectra observed for beryllium and their possible explanations. (✓= treatable by means of CRDS)

TDS feature:	**explainable by:**
HT-peak	• trapping of H in V ✓
emergence of LT-peak above Φ_c	• surface barriers ✓ • beryllium-hydride • gas-filled cavities
substructure of LT-peak	• combination of previous processes?
reduction of retention above Φ_c	• occupation-dependant surface barriers ✓ • partial connection among gas-filled cavities with surface • sputtering of surface hydrogen during ion implantation
shift of high-T peak position at low-fluence	• V-diffusion ✓ • increase of total V amount (retrapping) ✓
crystal-orientation dependent peak position	• anisotropic vacancy diffusion ✓ • anisotropic SIA diffusion + annihilation mechanisms ✓
emergence of a shoulder left from the high-T peak	• multiple hydrogen per vacancy ✓
low-T peak contains majority of the hydrogen at very high fluence ($\Phi = 10^{25} m^{-2}$)	• highly increased surface area (e.g. due to porosity) ✓ • high amount of gas-filled bubbles (almost no mono-vacancies) • high amount of hydride

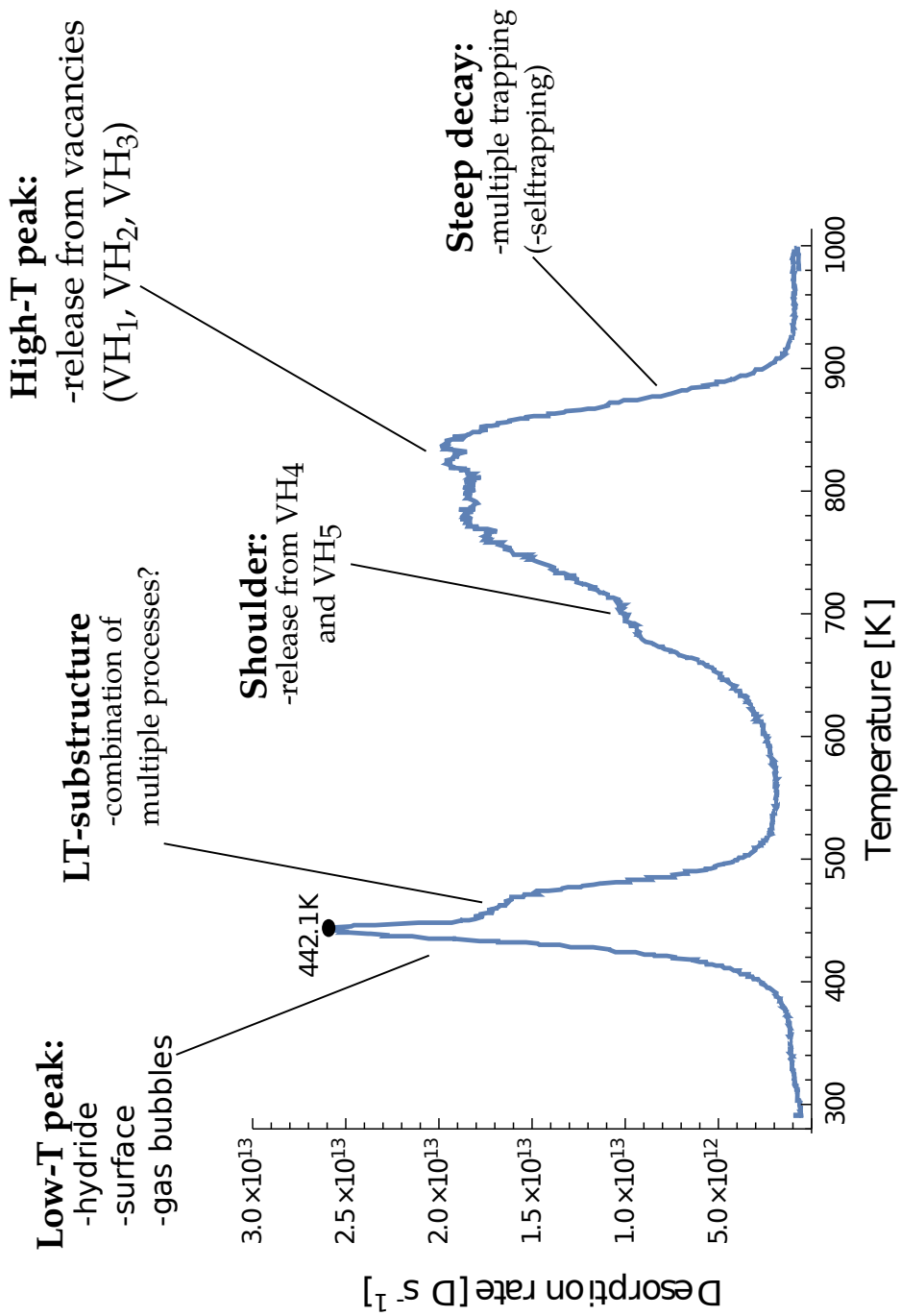

Figure 60: Summary of properties observed in TDS experiments and their possible explanation (sample BeDS29 in [50][51]).

5.2. Suggestions for future experiments

The emergence of the low temperature peak in thermal desorption spectroscopy experiments with poly- and single-crystalline beryllium is of high interest because it contains the majority of hydrogen isotopes within beryllium at fluences relevant for fusion applications.

Three different mechanisms were discussed within this master thesis. Based on the previous arguments we suggest further experiments which partially can be performed using the ARTOSS experiments in order to either disprove or verify the different hypothesis.

- **investigations of surface desorption processes:** the experiment done by Lossev & Küppers [37] gave insight into the desorption from Be(0001)-surfaces. However, the parameters provided by them seem to be contradictory to their data and also indicate desorption at room temperature. The ARTOSS experiment is capable of repeating the experiment using the atomic hydrogen source. Under the well-defined conditions of the experiment the quality of the data should be better and a detailed analysis can be performed. According to measurements by Reinelt the LT-peak does not change on time scale of hours at room temperature. If significant hydrogen surface desorption at room-temperature is observed, then the surface hypothesis can safely be considered as falsified. Also the desorption behaviour from other crystal surfaces is worth investigating. Until now there exist no desorption parameters for the $(11\bar{2}0)$-surface.
- **TEM studies of high-fluence exposed Be samples:** in order to investigate the bubble formation hypothesis nano-scale analysis of the material using transmission electron microscopy is recommended. In the measurements by Chernikov et al. [12] it is not evident if the 'lighter spots' from the TEM data are indeed gas-filled bubbles. Unfortunately, the TEM studies must be done ex-situ because ARTOSS does not have a TEM.

By using the capabilities of the ARTOSS experiment further insight can be gained into the physical processes involved in hydrogen retention in beryllium.

This thesis has shown that surface processes can qualitatively explain the emergence of low temperature peaks with increasing fluence. The exact shape could however not be reproduced either with first or second order desorption. Recommendations for possible experiments have been provided in order to get further insight into the nature of the low temperature desorption stage.

A. Appendix

A.1. Overview of experiments

A summary of all experiments provided by Reinelt is displayed in figure 61. These are sorted by fluence and heating rate. Please note, that the measurements were not performed in the given order, but rather that the sample names indicate.

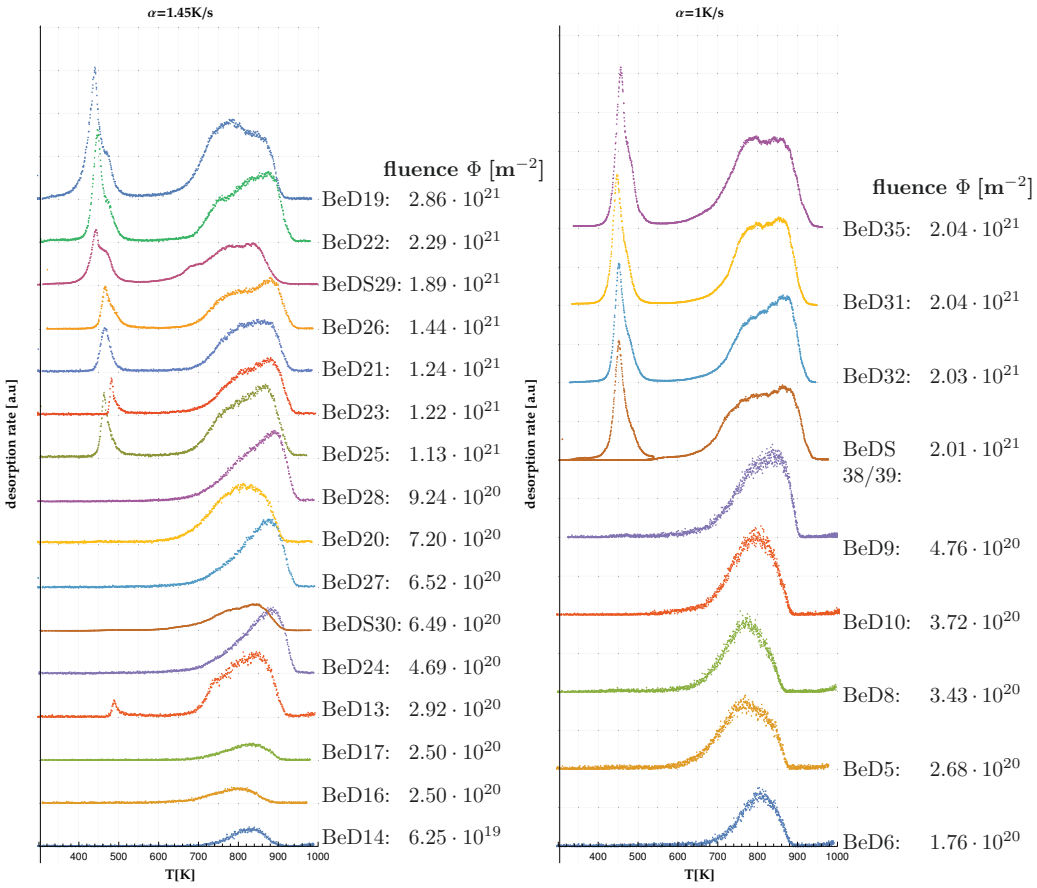

Figure 61: Summary of experimental data provided by M. Reinelt [51] sorted by fluence for $\alpha = 1$ K/s and 1.45 K/s, all measurements with $E_{prim} = 1$ keV.

Experiments with "S" in the name were performed with a different setup and calibration for which the desorption was measured in line-of-sight with a snorkel between sample and mass spectrometer. This results on the one hand in an increased signal to noise ratio but on the other hand may not be comparable due to insufficient accuracy of the calibration (compare

peak heights). It can also be observed that peak shapes alter strongly at comparable fluences which is probably related to the change of beam profiles during implantation. According to Reinelt the shape of the implantation spot changed from measurement to measurement [52]. Also the homogeneity of the implantation was not always satisfactory, it seems that the low temperature peak that is visible in BeD13 is caused by local supersaturation of particular regions of the implantation zone.

A.2. Vineyard's theory of thermally activated processes

In this section we review the paper by Vineyard [55] in which a formalism for the calculation of frequency factors of thermally activated processes is given which is based on arguments of statistical physics.

The frequency of a thermally activated process is found to follow the following expression

$$\Gamma = \tilde{\nu} \exp\left(-\frac{\Delta F}{k_B T}\right) \tag{A.1}$$

$$= \nu^* \exp\left(-\frac{\Delta E}{k_B T}\right), \tag{A.2}$$

where the free energy change $\Delta F = \Delta E - T\Delta S$, $\Delta E = E_{TS} - E_{eq}$ and $\Delta S = S_{TS} - S_{eq}$ relates to the system in the transition state and the equilibrium state.

An explicit formula for the frequency factor is given:

$$\nu^* = \frac{\prod_{i=1}^{n} \nu_i}{\prod_{i=2}^{n} \nu_i'}$$

where ν_i and ν_i' are the normal frequencies of the crystal in equilibrium and in transition-state

Assumptions:

- quantum effects are neglected
- small oscillations around stable position A and transition state P are assumed

Let a crystal contain $N/3$ atoms. The real-space coordinates of which are $(x_1, .., x_N)$ which are associated with masses $(m_1, .., m_N)$. So in total we have N spatial degrees of freedom. The potential energy of the whole system is given by $E_{pot} = E_{pot}(x_1, .., x_N)$.

A stable position of any particle (in our case: a hydrogen atom in an interstitial site or in the environment of a vacancy) is given by a local minimum in the N-dimensional configuration space denoted as A in figure 62. Another stable position B adjacent to this minimum shall exist which is connected to the previous point by an energetic barrier with saddle point P, which is part of hypersurface S of dimensionality $N - 1$. S is perpendicular to the lines of constant potential energy E_{pot}. Such that any point in configuration space that passes S with finite velocity will end up near the stable position B and vice-versa.

The total kinetic energy of the system is

$$E_{kin} = E_{kin}(\dot{x}_1, .., \dot{x}_N) = \sum_{i=1}^{N} \frac{1}{2} m_i \dot{x}_i^2. \tag{A.3}$$

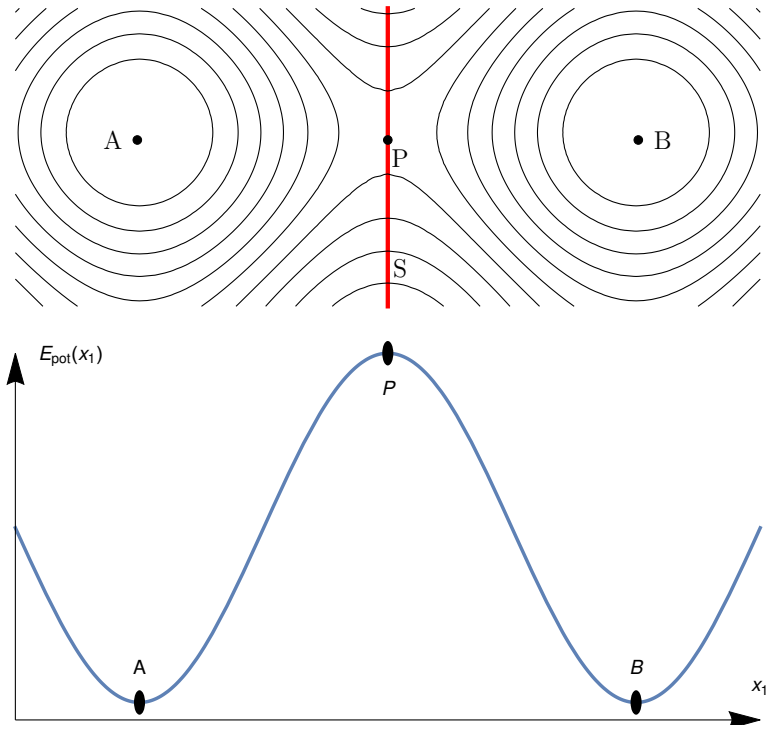

Figure 62: Top: 2D scheme of contours of the $N-1$ equipotential surfaces of E_{pot}, which is a function of all N spatial degrees of freedom. The stable positions are denoted as A and B. P marks the transition point (saddle point). S is the $N-1$ dimensional surface that seperates the basin of attraction of A from the corresponding region of B. All equipotential surfaces stand perpendicular to S. Bottom: Schematic energy profile along the trajectory between A and B if all other degrees of freedom are fixed.

For a system in thermal equilibrium the volume Q_A in the region "left" of S, and a number of points that crosses S from "left" to "right", denoted as I, defines the average transition rate Γ in $[s^{-1}]$ from A to B:

$$\Gamma = \frac{I}{Q_A} \tag{A.4}$$

Next we will determine Q_A and I.

For a classical system in thermal equilibrium the density in configuration space is given by

$$\rho = \frac{1}{Z} e^{-\frac{E_{pot}+E_{kin}}{k_B T}}. \tag{A.5}$$

Thus the number of states near A can be obtained as

$$Q_A = \frac{1}{Z}\int_A e^{-E_{pot}/k_BT}dX \quad \underbrace{\int_V e^{-E_{kin}/k_BT}dV}_{\prod_{i=1}^{N}\int_{-\infty}^{\infty} exp(-\frac{m_i\dot{x}_i}{2k_BT})d\dot{x}_i} \tag{A.6}$$

$$= \rho_0 \int_A e^{-E_{pot}/k_BT}dX, \tag{A.7}$$

where $dX = dx_1...dx_N$ and $dV = d\dot{x}_1...d\dot{x}_N$. $\rho_0 = \frac{1}{Z}\frac{(2\pi k_BT)^{N/2}}{\prod_i \sqrt{m_i}}$ is a normalization constant.

Let $dS = \{dS_1, ..., dS_N\}$ represent an element of S, then the total current of represantative points crossing S from "left" to "right" in point Y (on S) is given by $dI = dS \cdot \int V\rho(Y,V)dV$.

Thus:

$$dI = dS \cdot \int_{\mathbb{R}^N} V\rho(Y,V)d\dot{x}_1..d\dot{x}_N \tag{A.8}$$

$$= \frac{1}{Z}e^{-\frac{E_{pot}(Y)}{k_BT}}dS \cdot \int_{\mathbb{R}^N} Ve^{-\sum_i m_i\dot{x}_i^2/2k_BT}d\dot{x}_1..d\dot{x}_N \tag{A.9}$$

rotate the axis system such that the x_1-axis is parallel to dS at Y

$$dI = \frac{1}{Z}e^{-\frac{E_{pot}(Y)}{k_BT}}dS_1 \underbrace{\int_0^\infty \dot{x}_1 e^{-\frac{m_1\dot{x}_1^2}{2k_BT}}d\dot{x}_1}_{\frac{k_BT}{m_1}} \prod_{i=2}^{N} \underbrace{\int_{\mathbb{R}} e^{-\frac{m_i\dot{x}_i^2}{2k_BT}}d\dot{x}_i}_{\sqrt{\frac{2\pi k_BT}{m_i}}} \tag{A.10}$$

$$= \rho_0\sqrt{\frac{k_BT}{2\pi m_1}}e^{-\frac{E_{pot}(Y)}{k_BT}}dS_1. \tag{A.11}$$

Integration over S yields the total current

$$I = \int dI = \rho_0\sqrt{\frac{k_BT}{2\pi m_1}}\int_S e^{-\frac{E_{pot}(Y)}{k_BT}}dS_1. \tag{A.12}$$

We end up at the general result

$$\Gamma = \sqrt{\frac{k_BT}{2\pi m_1}}\frac{\int_S e^{-\frac{E_{pot}}{k_BT}}dS}{\int_A e^{-\frac{E_{pot}}{k_BT}}dX} \tag{A.13}$$

Note that the integral in the numerator is restricted to the hypersurface S, and is therefore of dimension $N-1$, whereas the integral in the denominator has dimension N, so that $[\Gamma] = s^{-1}$. This form accounts for many-body effects and is therefore very general.

In order to be able to evaluate eq. (A.13) we treat the integrals by small oscillations. Near the minimum A the potential energy may be approximated by a Taylor-series of second order. Since larger values in the exponential function decay quickly, this assumption is reasonable. The integration volumes may then be extended to $\mathbb{R}^N(\mathbb{R}^{N-1})$.

$$E_{pot} \approx E_{pot}(A) + \sum_{i=1}^{N} \frac{1}{2} m_i \omega_i^2 x_i^2. \tag{A.14}$$

The potential near the transition state (P) is handled similarly, note that the expansion only is done on the constraining surface, i.e. the direction of the actual jump is not included. On this surface P is, by construction, the minimum.

$$E_{pot} \approx E_{pot}(P) + \sum_{i=2}^{N} \frac{1}{2} m_i' \omega_i'^2 x_i'^2 \tag{A.15}$$

Inserting int (A.13) we find

$$\Gamma = \sqrt{\frac{kT}{2\pi m_1}} \frac{e^{-E_{pot}(P)/k_B T} \prod_{i=2}^{N} \int_{\mathbb{R}} e^{-\frac{m_i \omega_i'^2 x_i'^2}{2k_B T}} dx_i'}{e^{-E_{pot}(A)/k_B T} \prod_{i=1}^{N} \int_{\mathbb{R}} e^{-\frac{m_i \omega_i^2 x_i^2}{2k_B T}} dx_i} \tag{A.16}$$

$$= \frac{1}{2\pi} e^{-\Delta E/k_B T} \frac{\prod_{i=1}^{N} \omega_i}{\prod_{i=2}^{N} \omega_i'} \tag{A.17}$$

$$= e^{-\Delta E/k_B T} \frac{\prod_{i=1}^{N} \nu_i}{\prod_{i=2}^{N} \nu_i'}, \tag{A.18}$$

with the normal frequencies $\nu_i = 2\pi\omega_i$. Note, that this formula demands only knowledge about the curvature of the potential energy surface near the equilibrium position and the transition state other details of the energy landscape do not enter, in particular a possible energy difference between state A and B does not show up at all, only the barrier height is responsible for the temperature dependence of the transition rate.

A.3. First order surface desorption

First order desorption can for example be realised if atoms from the first subsurface-layer combine with atoms on the surface – in the limit of $\sigma \ll \sigma_{1st-layer}$, for which the area density of $\sigma_{1st-layer}$ can then be assumed to be not rate-limiting. In fact, Lossev & Küppers [37] reported that the peak position did not shift at higher coverages which is a property of first order desorption. The corresponding linear ordinary differential equation reads

$$\begin{cases} \dfrac{d\sigma(t)}{dt} & = -\nu_{des}(T(t))\sigma(t) \\ \nu_{des}(T) & = \nu_{des} exp\left(-\frac{E_{des}}{k_B T}\right) \\ \sigma(0) & = \sigma_0 \end{cases} \tag{A.19}$$

Again, we first consider the temperature-independent problem $\nu_{des}(T) = const = \tilde{\nu}_{des}$ with solution

$$\sigma(t) = \sigma_0 exp\left(-\tilde{\nu}_{des} t\right). \tag{A.20}$$

Accordingly, we insert the ansatz $\sigma(t) = \sigma_0 exp\,(-f(t))$ into (A.19) and find $f'(t) = \nu_{des}(T(t))$. The surface occupation therefore evolves according to

$$\sigma(t) = \sigma_0 exp\left(-\int_0^t \nu_{des}(T(t'))dt'\right) \tag{A.21}$$

which yields the desorption flux

$$j_{out}(t) = \frac{d}{dt}\sigma(t) = \nu_{des}(T(t))\sigma(t) \tag{A.22}$$

$$= \nu_{des}\sigma_0 \exp\left(-\frac{E_{des}}{k_B T(t)}\right) exp\left(-\int_0^t \nu_{des}(T(t'))dt'\right) \tag{A.23}$$

$$= \nu_{des}\sigma_0 \exp\left(-\frac{E_{des}}{k_B T(t)} - \frac{\nu_{des}E_{des}}{\alpha k_B}\Gamma\left(-1, \frac{E_{des}}{k_B T(t)}, \frac{E_{des}}{k_B T_0}\right)\right). \tag{A.24}$$

A linear heating ramp $T(t) = T_0 + \alpha t$ was assumed in the last step.

Corresponding desorption spectra for $\nu_{des} = 10^{13} s^{-1}$ (Debey frequency) and $E_{des} = 1.0$ eV are shown in 63.

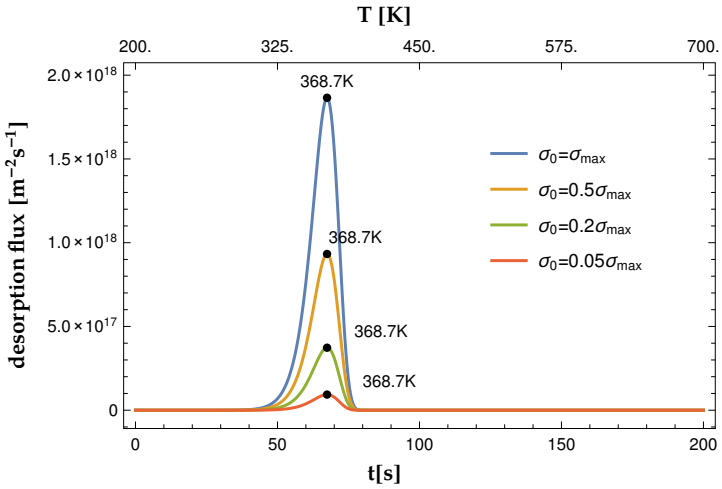

Figure 63: First order desorption spectra for different initial surface coverages.

Note that, unlike for the case of diffusion or second-order diffusion, a simple – even though implicit – expression for the peak position can be given by setting the derivative to zero and solve for T.

$$T_{peak}^2 exp\left(-\frac{E_{des}}{k_B T_{peak}}\right) = \frac{E_{des}\alpha}{k_B \nu_{des}}. \tag{A.25}$$

Due to the first-order nature (linearity) of (A.19), the desorption flux does not depend on the initial value (i.e. σ_0), whereas for a second-order surface desorption process the peak-position shifts to lower temperatures for increasing surface occupation.

A.4. Computational details

Spatial grid: We face the problem of solving a system of PDEs over a spatial extend of $L = 0.5mm$, whereas fine resolution of the implantation zone ($h \approx 100$ nm)is of major importance for accuracy of the predictions. Therefore, simulating the system with a uniform grid is not economic. Indeed, the most important mechanisms happen near the surface, where a huge number of defects is created due to collision cascades, whereas the concentration profiles in the rest of the sample are comparably smooth.

Therefore, solution of the PDE system is done on a non-uniform grid with usually $n_{grid} = 1000$ lattice points which is very dense in the near-surface regions in order to 1) resolve the implantation profile and 2) be able to simulate the whole sample.

It must be stated that the outcome of a simulation does not heavily depend on the sample size, unless it is chosen so small that significant desorption at the rear side takes place. If a major contribution of the whole outgassing happens at the back, this amount is missing at the front side. Even for the case of our predicted diffusion coefficient $D(T) = 1.89/\sqrt{A} \cdot e^{-0.4\ eV/k_B T}$ the contribution from the rear side is always well below 1% so that the integral values from the left outflux can be compared to experimental data. In the work by Piechoczek [48] his two-dimensional model had a simulation size of only 400 nm (direction perpendicular to surface) times 1 nm (with periodic boundaries in parallel to surface) which leads to a major contribution from rear side outflux. Comparison to experiments were only done with the front side fluxes, which then give misleading results. Nevertheless, the treatment of the direction parallel to the surface used a homogeneous implantation profile which in combination with the periodic boundaries does not change over time. Therefore, we decided to discard the second spatial dimension in the code, which results in much higher accuracy and performance of the code allowing us to simulate the whole spatial extend of the sample ($L = 0.5mm$). It must be stated that the results in Piechoczek's paper can exactly be reproduced using the one-dimensional code.

Particle number conservation: The system of PDEs conserves the particle number. Therefore, we continuously observe after each calculation if this also holds for the simulations by comparing the initial hydrogen amount (or the influx of hydrogen to the system), with the amount of hydrogen that leaves the sample (either during the heating ramp or before). The relative difference is in every case well below 10^{-3}.

Self-consistency of the solutions: In order to check if the solution that is provided by the *NDSolve*-routine provided by *Wolfram Mathematica* actually solves the PDE system, left- and righthandside of the PDE system are compared after inserting the solution. Deviations are usually small.

For simplicity, these studies were only performed for the system with Dirichlet boundary conditions (no surface barriers).

Accuracy and precision goal: *Wolfram Mathematica* provides parameters which indicate how large numerical errors may be tolerated when solving PDE systems. The estimated error may not be larger than $10^{-a} + f_i 10^{-p}$, where a is called *Accuracy Goal*, p - *Precision Goal* and the number f_i is a calculated value of the solution (e.g. $c_H(x,t)$ at some position (x,t)). How

these error estimates are performed is not reported. Therefore, we did convergence analysis for different values of a and p and found that values over 10 usually lead to satisfactory convergence. For calculations shown in this thesis we chose $a = p = 13$, which proved to be a good compromise between efficiency and accuracy.

Strictly positive concentrations: The system of PDEs (and the physical reality) does not allow for negative concentration values of the considered particles and defects. Nevertheless, using schemes for discretizations of PDEs to solve them numerically can lead to negative concentration values. Indeed these are observed for concentrations which should be very close to zero, which could in principle lead to instabilities of the solution. Contributions of negative-concentrations are usually in the range of the double precision (relative error 10^{-16}) so that for solutions which converged this should not be a problem. Nevertheless in some cases the solution diverges and gives non-physical results. These are usually easy to identify since they heavily violate the particle number conservation.

Implementation of surface effects: We presented a model composed of a coupled system of ODEs and PDEs. The *Wolfram Mathematica* software is not able to handle such systems. For numerical solvability the mixed system is transformed into a system which contains only partial differential equations. This is achieved by adding an artificial spatial coordinate to the surface occupation $\sigma(t) \to \sigma(x,t)$. The majority of equations do not need change, only boundary conditions and the surface term needs treatment to be included into the code. The terms are given in table 16.

Table 16: Transcription from the mixed equation type-model (ODEs & PDEs) to a system of PDEs only.

Model-system	**Implemented**
$\frac{d}{dt}\sigma_0(t) = j^0_{trans}(t) - j^0_{des}(t)$	$\partial_t \sigma(x,t) = j_{trans}(x,t) - j_{des}(x,t)$
$\frac{d}{dt}\sigma_L(t) = j^L_{trans}(t) - j^L_{des}(t)$	
$j^{0/L}_{des}(t) = \kappa_{des} e^{-E_{des}/k_B T} \sigma^2_{0/L}(t)$	$j_{des}(x,t) = \kappa e^{-E_{des}/k_B T} \sigma^2(x,t)$
$j^{0/L}_{trans}(t) = \nu_{trans} e^{-\frac{E_{trans}}{k_B T}} (1 - \frac{\sigma_{0/L}(t)}{\sigma_{max}}) c(0/L,t)$	$j_{trans}(x,t) = \nu_{trans} e^{-\frac{E_{trans}}{k_B T}} (1 - \frac{\sigma(x,t)}{\sigma_{max}}) c(x,t)$
$\partial_x c(x,t)\|_{x=0} = \frac{j^0_{trans}(t)}{D_H}$	$\partial_x c(x,t)\|_{x=0} = \frac{j_{trans}(0,t)}{D_H}$
$\partial_x c(x,t)\|_{x=L} = -\frac{j^L_{trans}(t)}{D_H}$	$\partial_x c(x,t)\|_{x=L} = -\frac{j_{trans}(L,t)}{D_H}$

The currents j_{trans} and j_{des} are chosen to be positive for the flow bulk $\rightarrow$ surface and accordingly surface $\rightarrow$ vacuum. Note, that there are no terms that connect $\sigma(x,t)$ and $\sigma(y,t)$ for $x \neq y$. Furthermore, there are no terms that would change the concentrations $c(x,t)$ due to the artificial $\sigma(x,t)$. In the end, only the values of $\sigma(x=0,t)$ and $\sigma(x=L,t)$ are considered for physical results. Therefore, the artificial extension of σ does not lead to change in physically observable quantities.

B. References

[1] E. Abramov, M. Riehm, D. Thompson **Deuterium permeation and diffusion in high-purity beryllium**, J. Nucl. Mat. 175 90-95 (1990)

[2] V. Kh. Alimov, V. N. Chernikov, A. P. Zakharov, **Depth distribution of deuterium atoms and molecules in beryllium implanted with D ions**, J. nucl. mat. 241-243, 1047-1052 (1997)

[3] A. Allouche, **Density functional study of hydrogen adsorption on beryllium (0001)**, Phys. Rev. B 78, 085429 (2008)

[4] A. Allouche, M. Oberkofler, M. Reinelt, Ch. Linsmeier, **Quantum modeling of hydrogen retention in Beryllium bulk and vacancies**, J. Am. Ch. Soc., 10.1201 (2010)

[5] J. Ambrosek, G. Longhurst, **Verification And Validation Of The Tritium Transport Code TMAP7**, Idaho, INEEL/CON-04-01593 (2004)

[6] R. A. Anderl, R. A. Causey, J. W. Davis, et al. , **Hydrogen isotope retention in beryllium for tokamak plasma-facing applications**, J. Nucl. Mat 273, 1-26 (1999)

[7] M. Ardenne, G. Musiol, U. Klemradt, **Effeke der Physik und ihre Anwendung**, 3. Auflage, deutsche Ausgabe, Verlag Harri Deutsch, 2005

[8] D. Bachurin, V. Borodin, M. Ganchenkova, A. Möslang, Ch. Stihl, P. Vladimirov, **Multiscale modeling of beryllium in fusion environment**, presentation ICFRM-17, Aachen 2015

[9] M. Baskes, **A calculation of the surface recombination rate constant for hydrogen isotopes on metals**, J. Nucl. Mat. 92, 318-324 (1980)

[10] R. Behrisch, G. Federici, A. Kukushkin, D. Reiter, **Material erosion at the vessel walls of future fusion devices**, J. Nucl. Mat. 313-316, 388-392 (2003)

[11] R. Causey, **Hydrogen isotope retention and recycling in fusion reactor plasma-facing components**, J. Nucl. Mat. 300, 91-117, (2002)

[12] V. Chernikov, V. Alimov, A. Markin, et. al. **Gas-induced swelling of beryllium implanted with deuterium ions**, J. Nucl. Mat., 233-237, 860-864 (1996)

[13] R. Conn, R. Doerner, J. Won, **Beryllium as the plasma-facing material in fusion energy systems — experiments, evaluation, and comparison with alternative materials**, Fus. Eng. and Des. 37, 481-513 (1997)

[14] R. Doerner, M. Baldwin, D. Buchenauer. G. De Temmerman, D. Nishijima,**The role of beryllium deuteride in plasma-beryllium interactions**, J. Nucl. Mat. 390-391, 681-684 (2009)

[15] W. Eckstein, **Calculated sputtering, reflection and range values**, IPP Report 9/132 (2002)

[16] W. Eckstein, R. Dohmen, A. Mutzke, R. Schneider, **SDTrimSP: a monte-carlo code for calculating collision phenomena in randomized targets**, IPP 12/3 (2007)

[17] L. Ferry, **Contribution to the study of tritium behavior in beryllium (ITER context)**, PhD student, Institut de Radioprotection et de Sûreté Nucléaire (2014-2017)

[18] L. Ferry, et al., **Building a comprehensive set of elementary mechanism for H in Be via DFT**, in preparation (2016)

[19] S. Fujita, A. Garcia, **Theory of hydrogen diffusion in metals. Quantum isotope effect**, J. Phys. Chem. Solids 52 pp. 351-355, 1991

[20] M. Ganchenkova, V. Borodin, **Ab initio study of small vacancy complexes in beryllium**, Phys. Rev. B 75, 054108 (2007)

[21] M. Ganchenkova, V. Borodin, R. Nieminen, **Hydrogen in beryllium: solubility, transport, and trapping**, Phys. Rev. B 79, 134101 (2009)

[22] M. Glicksman, **Diffusion in solids, field theory, solid-state principles, and applications**, Wiley interscience (2000)

[23] J. Guterl, R. D. Smirnov, S. I. Krasheninnikov, **Revisited reaction-diffusion model of thermal desorption spectroscopy experiments on hydrogen retention in material**, J. Appl. Phys. 118, 043302 (2015)

[24] A. Haasz, J. Davis, **Deuterium retention in beryllium and tungsten at high fluences**, J. Nucl. Mat 241-243, 1076-1081 (1997)

[25] G. Henkelmann, B. Uberuaga, H. Jonsson, **A climbing image nudged elastic band method for finding saddle points and minimum energy paths**, J. Chem. Phys. 113, 22 (2000)

[26] International atomic energy agency Vienna, **ITER final design report**, ITER documentation series No. 22, 2001

[27] ITER-homepage, `www.iter.org`

[28] J. Jacquinot and the JET team, **Deuterium-tritium operation in magnetic confinement experiments: results and underlying physics**, Plasma Phys. Control. Fusion 41, A13-A46 (1999)

[29] The JET Team: P. Thomas, **Results of JET operation with beryllium**, J. Nucl. Mat. 176-177, 3-13 (1990)

[30] P. Jones, R. Gibson, **Hydrogen in beryllium**, Nucl. Mat. 21, 353 (1967)

[31] A. de Jong, J. Niemantsverdriet, **Thermal desorption analysis: comparative test of ten commonly applied procedures**, Surf. Sc. 23, 355-365 (1990)

[32] M. Kaufmann, **Plasmaphysik und Fusionsforschung**, 2. Auflage, deutsche Ausgabe, Springer (2003)

[33] K. Kizu, K. Miyazaki, T. Tanabe, **Hydrogen permeation and diffusion in beryllium**, Fusion Technology 28, 1205-1210 (1995)

[34] H. Kugler, **Gmelin Handbook of Inorganic and Organometallic Chemistry**, 8th edition, Berylium suppl., Vol A1, Springer (1986)

[35] R. Langley, **Interaction of implanted deuterium and helium with berylium: radiation enhance oxidation**, J. Nucl. Mat. 86& 86, 1123-1126 (1979)

[36] V. Lossev, J. Küppers, **Interaction of hydrogen atoms with beryllium (0001) surfaces**, J. Nucl. Mat. 196-198, 953-957 (1992)

[37] V. Lossev, J. Küppers, **Adsorption of hydrogen on Be(0001) surfaces**, Surf. Sc. 284, 175-185 (1993)

[38] Ch. Linsmeier, P. Goldstraß, K. Klages, **ARTOSS - A new surface science experiment to study the hydrogen inventory in multi-component materials**, Phys. Scr. T94, 28-33 (2001)

[39] D. Maisonnier et al., **Power plant conceptual studies in Europe**, Nucl. Fusion 47, 1524-1532 (2007)

[40] A. Markin, V. Chernikov, S. Rybakov, A. Zakharov, **Thermal desorption of deuterium implanted in beryllium**, J. Nucl. Mat., 233-237, 865-869 (1996)

[41] H. Mehrer, **Diffusion in solids, Fundamentals, Methods, Materials, Diffusion-Controlled Processes**, Springer (2007)

[42] S. Middleburgh, R. Grimes, **Defects and transport processes in beryllium**, Act. Mat. 59, 7095-7103 (2011)

[43] M. Oberkofler, M. Reinelt, A. Allouche, S. Lindig, Ch. Linsmeier, **Towards a detailed understanding of the mechanisms of hydrogen retention in beryllium**, Phys. Scr. T138 (2009)

[44] M. Oberkofler, M. Reinelt, Ch. Linsmeier, **Retention and release mechanisms of deuterium implanted into beryllium**, Nucl. Instr. Meth. B 269, 1266-1270 (2011)

[45] M. Oberkofler, **Rückhaltemechanismen für Wasserstoff in metallischem Beryllium und Berylliumoxid sowie Eigenschaften von ioneninduziertem Berylliumnitrid**, IPP 17/31, 2012

[46] M. Pick, K. Sonnenberg, **A model for atomic hydrogen-metal interactions - application to recycling, recombination and permeation**, J. Nucl. Mat. 131, 208-220 (1984)

[47] R. Pitts et al., **Status and physics basis of the ITER divertor**, Phys. Scr. T138, 014001 (2009)

[48] R. Piechoczek, M. Reinelt, M. Oberkofler, A. Allouche, Ch. Linsmeier, **Deuterium trapping and release in Be(0001), Be(11$\bar{2}$0) and polycrystalline beryllium**, J. Nucl. Matt. 438, S1072-S1075 (2013)

[49] M. Reinelt, Ch. Linsmeier, **Temperature programmed desorption of 1 keV deuterium implanted into clean beryllium**, Phys. Scr. T128, 111-113 (2007)

[50] M. Reinelt, A. Allouche, M. Oberkofler, Ch. Linsmeier, **Retention mechanisms and binding states of deuterium implanted into beryllium**, New J. Phys. 11 043023 (2009)

[51] M. Reinelt, **Untersuchung zur Erosion ultradünner Kohlenstoffschichten und Wasserstoffrückhaltung in Beryllium**, (2008)

[52] M. Reinelt, private communication

[53] I. Tazhibaeva, V. Shestakov, E. Chikhray et al., Proc 18th Symp. Fus. Technol. 22-26 August, Karlsruhe, Fus. Technol. 427 (1994)

[54] D. Thomson, R. Macauley-Newcombe, **Solubility, diffusion and desorption of hydrogen isotopes in beryllium and tungsten**, CFFTP G-9585, (1996)

[55] G. H. Vineyard, **Frequency factors and isotope effects in solide state rate processes**, J. Phys. Chem. Solids Vol 3, 121-127 (1957)

[56] Wolfram Research, Inc., **Mathematica**, Version 10.3, Champaign, IL (2015)

[57] Y. Yang, P. Coppens, **The Electron Density and Bonding in Beryllium Metal as Studied by Fourier Methods**, Acta Cryst. A34, 61-65 (1978)

[58] S. Zalkind, M. Polak, N. Shamir, **Adsorption of hydrogen on clean and oxidized beryllium studied by direct recoil spectrometry**, Appl. Surf. Sc. 115, 273-278 (1997)

[59] P. Zhang, J. Zhao, Bin Wen, **Retention and diffusion of H, He, O, C impurities in Be**, J. Nucl. Mat. 423, 164-169 (2012)

[60] P. Zhang, J. Zhao, **Interactions of extrinsic interstitial atoms (H, He, O, C) with vacancies in beryllium from first-principles**, Comp. Mat. Sc. 90, 116-122 (2014)

C. List of figures

D. List of tables

Band / Volume 332
Analysis of biomixtures to determine the fate of pesticides
S. Mukherjee (2016), xix, 136 pp
ISBN: 978-3-95806-163-7

Band / Volume 333
Temperature Dependence of Carbon Kinetic Isotope Effect for The Oxidation Reaction of Ethane by Hydroxyl Radicals Under Atmospherically Relevant Conditions: Experimental and Theoretical Studies
T. Piansawan (2016), 196 pp
ISBN: 978-3-95806-166-8

Band / Volume 334
Konzeption von Membranmodulen zur effizienten Abtrennung von Kohlendioxid aus Gasgemischen
S. Luhr (2016)
ISBN: 978-3-95806-170-5

Band / Volume 335
Einfluss fehlpassungsinduzierter Spannungsfelder auf den Transportprozess bei ionischer Leitung
J. Keppner (2016), viii, 171 pp
ISBN: 978-3-95806-171-2

Band / Volume 336
Production and Characterization of Monodisperse Uranium Particles for Nuclear Safeguards Applications
A. Knott (2016), A-H, 123, xxviii, xiii pp
ISBN: 978-3-95806-172-9

Band / Volume 337
3D hydrological simulation of a forested headwater catchment: Spatio-temporal validation and scale dependent parameterization
Z. Fang (2016), XVII, 119 pp
ISBN: 978-3-95806-174-3

Band / Volume 338
Influence of Thermomechanical Treatment on High Temperature Properties of Laves Phase Strengthened Ferritic Steels
M. Talík (2016), xxiii, 130 pp
ISBN: 978-3-95806-175-0

Band / Volume 339
Groundwater recharge in Slovenia
Results of a bilateral German-Slovenian Research project
Mišo Andjelov, Zlatko Mikulič, Björn Tetzlaff, Jože Uhan & Frank Wendland (2016)
ISBN: 978-3-95806-177-4

Band / Volume 340
Atomic oxygen derived from SCIAMACHY O(^{1}S) and OH airglow measurements in the Mesopause region
Y. Zhu (2016), 206 pp
ISBN: 978-3-95806-178-1

Band / Volume 341
Diagnostic Mirror Concept Development for Use in the Complex Environment of a Fusion Reactor
A. Krimmer (2016), x, 123 pp
ISBN: 978-3-95806-180-4

Band / Volume 342
Long-Term Measurements of the Radiation Exposure of the Inhabitants of Radioactively Contaminated Regions of Belarus – The Korma Report II (1998 – 2015)
P. Zoriy, H. Dederichs, J. Pillath, B. Heuel-Fabianek, P. Hill, R. Lennartz (2016), ca 105 pp
ISBN: 978-3-95806-181-1

Band / Volume 343
Entwicklung und Charakterisierung von Nickel/Gadolinium-Ceroxid-basierten Anoden für die metallgestützte Festoxid-Brennstoffzelle
V. Rojek-Wöckner (2016), XVI, 136 pp
ISBN: 978-3-95806-182-8

Band / Volume 344
Reaction-diffusion modelling of hydrogen retention and release mechanisms in beryllium
M. Wensing (2016), 100 pp
ISBN: 978-3-95806-184-2

Weitere ***Schriften des Verlags im Forschungszentrum Jülich*** unter
http://wwwzb1.fz-juelich.de/verlagextern1/index.asp

Energie & Umwelt /
Energy & Environment
Band / Volume 344
ISBN 978-3-95806-184-2

JÜLICH
FORSCHUNGSZENTRUM